

AD-A021 744

INVESTIGATIONS OF TECTONIC STRESS, APPLIED
RELAXATION-SOURCE THEORY TO EARTHQUAKE-EXPLOSION
DISCRIMINATION

Charles B. Archambeau

Colorado University

Prepared for:

Air Force Cambridge Research Laboratories

15 August 1975

DISTRIBUTED BY:

NTIS

National Technical Information Service
U. S. DEPARTMENT OF COMMERCE

Best possible scan

REPRODUCED BY
**NATIONAL TECHNICAL
INFORMATION SERVICE**
U. S. DEPARTMENT OF COMMERCE
SPRINGFIELD, VA. 22161

Best possible scan

Unclassified

SECURITY CLASSIFICATION OF THIS PAGE (When Data Entered)

REPORT DOCUMENTATION PAGE		READ INSTRUCTIONS BEFORE COMPLETING FORM
1. REPORT NUMBER AFCL-TP-75-0467	2. GOVT ACCESSION NO.	3. RECIPIENT'S CATALOG NUMBER
4. TITLE (and Subtitle) INVESTIGATIONS OF TECTONIC STRESS, Applied Relaxation-Source Theory to Earthquake- Explosion Discrimination	5. TYPE OF REPORT & PERIOD COVERED Final Technical Report 1 November 1973-31 August 1975	
	6. PERFORMING ORG. REPORT NUMBER	
7. AUTHOR Charles B. Archambeau	8. CONTRACT OR GRANT NUMBER(s) F19628-74-C-0087	
9. PERFORMING ORGANIZATION NAME AND ADDRESS The Regents of the University of Colorado Boulder, Boulder County, Colorado 80309	10. PROGRAM ELEMENT, PROJECT, TASK AREA & WORK UNIT NUMBERS 1795-N/A-N/A Amend. #5 62701E	
11. CONTROLLING OFFICE NAME AND ADDRESS Defense Advanced Research Projects Agency 1400 Wilson Blvd. Arlington, Virginia 22209	12. REPORT DATE 15 August 1975	
	13. NUMBER OF PAGES 188	
14. MONITORING AGENCY NAME & ADDRESS (if different from Controlling Office) Air Force Cambridge Research Laboratory Hanscom AFB, Massachusetts 01731 Contract Monitor: Stanley M. Needleman/LWW	15. SECURITY CLASS. (of this report) Unclassified	
	15a. DECLASSIFICATION/DOWNGRADING SCHEDULE	
16. DISTRIBUTION STATEMENT (of this Report) Approved for public release; distribution unlimited		
17. DISTRIBUTION STATEMENT (of the abstract entered in Block 20, if different from Report)		
18. SUPPLEMENTARY NOTES		
19. KEY WORDS (Continue on reverse side if necessary and identify by block number) m _b -M _g , earthquakes, relaxation source models, tectonic, stress field, explosions, discriminants		
20. ABSTRACT (Continue on reverse side if necessary and identify by block number) Results relating to the analytical modeling of earthquakes by relaxation- source theory models are summarized. Applications to explosion-earthquake discrimination and earthquake source parameter estimation, particularly tectonic stress determinations, are discussed in detail. The theoretical work summarized includes: generalized representation theorems, energy con- siderations, equivalence theory, radiation field solutions for relaxation models of earthquakes, computer based earthquake field simulation, predictions		

D D C
RECEIVED
 MAR 8 1976
REGISTERED
 A

Unclassified

SECURITY CLASSIFICATION OF THIS PAGE(When Date Entered)

of m_b - M_s relations for earthquakes and explosions, and comparisons of relaxation source theory results with results from numerical models of earthquakes. Further, the theoretical basis for m_b - M_s discrimination and discrimination using spectral magnitude parameters is discussed in detail. Comparative studies undertaken, involving observed data for earthquakes, include comparisons of relaxation theory spectra to observations of earthquake spectra in the near field distance range with associated inference of source properties, and modeling of the static field using numerical dislocation and relaxation models in order to infer failure conditions and prestress fields. An observational study of P wave spectral discrimination of earthquakes and explosions is described, and it is concluded that the observed behavior of these spectral magnitudes is in agreement with the theoretical predictions and can serve as a very powerful discrimination procedure.

Stress field estimates of magnitude and spatial variability are inferred from the set of world-wide m_b - M_s data for the period 1968-1974, using relaxation theory predictions of magnitude. Some seismic regions, for example the Aleutians, show high magnitude stress concentrations, above 1 kbar at shallow depths. Such zones appear to be spatially localized to volumes of the order of 10 km or less, with general stress levels elsewhere of around 100 bars.

Unclassified

SECURITY CLASSIFICATION OF THIS PAGE(When Date Entered)

TABLE OF CONTENTS

I.	Introduction	1
II.	A Summary of Results of Research on Earthquake Sources and Earthquake-Explosion Discrimination	4
	1. Theoretical Investigations	4
	(a) Formulation of Representation Theorems	4
	(b) Energy Considerations	4
	(c) Equivalence Theory	5
	(d) Radiation Field Solutions for Relaxation Models	6
	(e) Computer Based Earthquake Field Simulation	14
	(f) Predictions of $m_b - M_s$ for Earthquakes and Explosions and Investigations of New Discrimination Methods	15
	(g) Comparisons with Numerical Models of Earthquakes	28
	2. Interpretive Studies: Comparisons of Predictions with Observational Data	30
	3. References to the Detailed Developments and Complete Results	43
III.	Multiple and Single Explosion Discrimination Using Frequency Dependent Magnitudes	46
	1. Discrimination Methods based on $\bar{m}_b - \bar{M}_s$	46
	2. Discrimination Methods based on the \bar{m}_b (f) Parameter	97
	3. Observational Testing and Results for \bar{m}_b (f) Space Discrimination	132
IV.	Earthquake Source Properties: Tectonic Stress Estimates	155
V.	General Conclusions and Comments on Remaining Problems	167
	Acknowledgments	171
	References	173

INDEX OF FIGURES

Fig. 1.	Theoretical Rayleigh wave radiation patterns for a multiple explosion of three 100 kt events, no prestress. Period range $8 \leq T \leq 38$ sec.	Page 48
Fig. 2.	Theoretical Rayleigh wave spectra and time series at three azimuths for the multiple event of Fig. 1.	Page 49
Fig. 3.	Theoretical Rayleigh and Love wave radiation patterns at 20 seconds period for a 2.5 km fault length, dip slip earthquake, 500 bar stress drop.	Page 51
Fig. 4.	Theoretical Rayleigh and Love wave radiation patterns at 14 sec period for the same earthquake as shown in Fig. 3.	Page 52
Fig. 5.	Comparison of time domain P wave signals from an earthquake and two multiple explosions, both with tectonic release, designed to yield a P wave signal train similar to that from an earthquake as well as $m_b - M_s$ values appropriate to those for an earthquake. Distance 4000 km, azimuth 30° .	Page 55
Fig. 6.	Compressional wave trains for five different multiple explosions involving various combinations of 5, 20 and 100 kt explosions with tectonic release included.	Page 56
Fig. 7.	Love waves from the five different multiple explosions of Fig. 6.	Page 57
Fig. 8.	Rayleigh waves from the five different multiple explosions of Figs. 6 and 7.	Page 58
Fig. 9.	Rayleigh surface wave magnitude as a function of body wave magnitude for single and multiple explosions.	Page 60
Fig. 10.	Love surface wave magnitude as a function of body wave magnitude for single and multiple explosions.	Page 62
Fig. 11.	Spectral characteristics of the explosions for yields in the range of 10 - 1000 kt.	Page 64
Fig. 12.	Spectral characteristics of an earthquake with fault dimensions of the order of 2.5 km ($m_b \approx 4.5$, if stress drop is about 500 bars).	Page 65

- Fig. 13. Plot of the log of the narrow band filter amplitude maximum, A_g , normalized by the center period of the filter (T_g) versus the log of the time domain seismogram P wave amplitude, A_1 , normalized by the effective period T_1 . Page 74
- Fig. 14. Plot of the log of the narrow band filter amplitude maximum, A_g , normalized by the filter center period, T_g , versus A_1 and T_1 measured from the time domain seismograms; both for Rayleigh type surface waves with $T_g = 20$ sec and T_1 approximately 20 sec. Page 76
- Fig. 15. Log of the narrow band filter amplitude maximum, A_g , divided by the filter center period, T_g , versus $\log A_1/T_1$ for Love waves at $T_g = T_1 = 20$ sec. Page 77
- Fig. 16. An example of narrow band filter output at two frequencies for a multiple explosion event. Page 79
- Fig. 17. An example of narrow band filter output at two frequencies for a single explosion. Page 81
- Fig. 18. An example of narrow band filter output at two frequencies for a small earthquake. Page 82
- Fig. 19. Narrow band filter output at two frequencies for a moderate earthquake (stress drop of 500 bars). Page 83
- Fig. 20. Narrow band filter output at two frequencies for a large earthquake (500 bar stress drop used). Page 84
- Fig. 21. Narrow band filter output from surface waves generated by a moderate sized earthquake. Page 85
- Fig. 22. Rayleigh type spectral surface wave magnitude as a function of spectral body wave magnitude for earthquakes and multiple explosions. Page 87
- Fig. 23. Love type spectral surface wave magnitude as a function of spectral body wave magnitude for earthquakes and multiple explosions. Page 89
- Fig. 24. Rayleigh type spectral surface wave magnitude as a function of spectral body wave magnitude for single explosions and earthquakes. Page 92
- Fig. 25. Love type spectral surface wave magnitude as a function of spectral body wave magnitude for single explosions and earthquakes. Page 95

- Fig. 26. Spectral explanation of the predicted $\bar{m}_b - \bar{M}_s^R$ and $\bar{m}_b - \bar{M}_s^L$ relations for earthquakes and single and multiple explosions. Page 99
- Fig. 27. Spectral basis for frequency dependent magnitude discriminants involving high frequency body wave magnitudes. Page 104
- Fig. 28. Frequency dependent spectral magnitudes $\bar{m}_b(f)$ as functions of the conventional body wave magnitude $m_b(1)$ for earthquakes. Page 108
- Fig. 29. Frequency dependent spectral magnitudes $\bar{m}_b(f)$ as functions of the conventional body wave magnitude $m_b(1)$ for explosions. Page 109
- Fig. 30. Rayleigh type spectral surface wave magnitude \bar{M}_s^R as a function of $\bar{m}_b(1.5)$, the frequency dependent spectral body wave magnitude at 1.5 Hz, for earthquakes, multiple explosions and single explosions. Page 113
- Fig. 31. Rayleigh type spectral surface wave magnitude \bar{M}_s^R as a function of $\bar{m}_b(2.5)$, the frequency dependent spectral body wave magnitude at 2.5 Hz, for earthquakes, multiple explosions and single explosions. Page 115
- Fig. 32. Love type spectral surface wave magnitude \bar{M}_s^L as a function of $\bar{m}_b(1.5)$, the frequency dependent spectral body wave magnitude at 1.5 Hz, for earthquakes, multiple explosions and single explosions. Page 117
- Fig. 33. Love type spectral surface wave magnitude \bar{M}_s^L as a function of $\bar{m}_b(2.5)$, the frequency dependent spectral body wave magnitude at 2.5 Hz, for earthquakes, multiple explosions and single explosions. Page 119
- Fig. 34. Low frequency spectral body wave magnitude $\bar{m}_b(0.3)$, as a function of the high frequency body wave magnitude $\bar{m}_b(1.5)$, for earthquakes, multiple explosions and single explosions. Page 122
- Fig. 35. Low frequency spectral body wave magnitude $\bar{m}_b(0.3)$, as a function of the high frequency body wave magnitude $\bar{m}_b(2.0)$, for earthquakes, multiple explosions and single explosions. Page 125

Fig. 36.	Low frequency spectral body wave magnitude, $\bar{m}_b(0.3)$, as a function of the high frequency body wave magnitude, $m_b(2.5)$, for earthquakes, multiple explosions and single explosions.	Page 128
Fig. 37.	Low frequency spectral body wave magnitude $\bar{m}_b(0.3)$, as a function of the high frequency body wave magnitude, $\bar{m}_b(3.0)$, for earthquakes, multiple explosions and single explosions.	Page 130
Fig. 38.	Examples of narrow band filter outputs.	Page 133
Fig. 39.	Spectral magnitudes, \bar{m}_b , for observed Eurasian events.	Page 135
Fig. 40.	Spectral magnitude discrimination showing the effect of varying f_c of the low frequency magnitude.	Page 137
Fig. 41.	Spectral magnitude discrimination showing the effect of varying f_c of the high frequency magnitude.	Page 139
Fig. 42.	Spectral magnitudes of deep earthquakes recorded at LASA.	Page 142
Fig. 43.	Spectral magnitudes at $f_c = 0.6$ Hz and $f_c = 5.0$ Hz for events recorded at the Oyer array, Norway.	Page 144
Fig. 44.	Filter amplitudes with noise corrections for the same events as in Fig. 43.	Page 145
Fig. 45.	An example of signal detection using a narrow band filter comb.	Page 146
Fig. 46.	Amplitudes of narrow band filter envelope peaks at two frequencies for deep earthquakes recorded at Norway.	Page 148
Fig. 47.	Narrow band filter outputs at 3 frequencies for an explosion and a deep earthquake.	Page 149
Fig. 48.	Simulation of multiple explosion seismograms.	Page 151
Fig. 49.	Spectral magnitude discrimination for earthquakes, single explosions and multiple explosions.	Page 153
Fig. 50.	$m_b - M_s$ event data for Seismic Region 1, Alaska-Aleutian Arc.	Page 156

Fig. 51.	$m_b - M_s$ event data for Seismic Region 2, Eastern Alaska to Vancouver Island.	Page 158
Fig. 52.	$m_b - M_s$ event data for Seismic Region 3, California-Nevada region.	Page 159
Fig. 53.	$m_b - M_s$ event data for Seismic Region 4, Baja California and Gulf of Mexico.	Page 160
Fig. 54.	$m_b - M_s$ event data for Seismic Region 5, Mexico-Guatemala area.	Page 161
Fig. 55.	$m_b - M_s$ event data for Seismic Region 6, Central America.	Page 162
Fig. 56.	$m_b - M_s$ event data for Seismic Region 7, Caribbean loop.	Page 163
Fig. 57.	$m_b - M_s$ event data for Seismic Region 8, Andean South America.	Page 164
Fig. 58.	$m_b - M_s$ event data for Seismic Region 19, Japan - Kuriles - Kamchatka.	Page 165

I. INTRODUCTION

This final report contains a summary of research work undertaken over the last two years, including the work under the current Contract F 19628-74-C-0087, sponsored by the Defense Advanced Research Project Agency, ARPA Order No. 1795, Amendment #5. In order to present a more comprehensive discussion, some work carried out jointly under other contracts is incorporated. The other contract research support is listed in the Acknowledgments section of this report.

The objectives of the current contract were:

(1) To use present theoretical earthquake models (in particular relaxation models) as a framework for the interpretation of the seismic radiation from earthquakes, especially small earthquakes of magnitude $m_b < 5$.

(2) To utilize available world-wide $m_b - M_s$ data to provide estimates of nonhydrostatic stress levels and the spatial variations of this field.

(3) To incorporate complex, non-homogeneous prestress and general fault geometries as relaxation theory models through the use of numerical modeling methods, with the numerical calculations designed to provide the definition of equilibrium field changes to be used in the analytical relaxation theory.

In section II of this report, the results of the research effort in these areas has been summarized. A major part of this work has involved theoretical work designed to extend and amplify the relaxation theory. A significant part of the work reported also involves comparisons of

theoretical predictions to observations of earthquake radiation in the near field distance range. Results relating to the inference of the tectonic stress state associated with failure are summarized.

Further, in part as a means of verifying some details of relaxation theory models, results relating to spectral magnitude discrimination are discussed in some detail in section III. These results show that the theory properly predicts the character of the high frequency radiation from earthquakes and that discriminants based on the differences between earthquake and explosion compressional wave radiation are very effective. In particular, an observational study involving roughly 200 Eurasian events showed that the theoretical predictions based on source theory models were quite accurately reproduced from the observations.

Section IV deals directly with the measurement of nonhydrostatic stress using $m_b - M_s$ data. Specifically the magnitude and spatial character of the tectonic stress field is inferred from a large, world-wide set of earthquake magnitude data. Consistent with independent observations summarized in part II, very large nonhydrostatic stresses, of the order of 1 kbar and larger, seem to be required to explain $m_b - M_s$ data for some events in certain seismic regions. These rather high stress levels appear to be very local, and to be concentrated within regions of spatial extent near 10 km in radius. In general, stress levels near 100 bars predominate, but the spatial character of the stress field, as inferred from spatial contours of the inferred stress levels for events within a seismic zone, can be complex.

Section V provides a short summary of some of the important results that are regarded as especially pertinent to event discrimination as well

as earthquake modeling. Some of the more obvious problems remaining and requiring further work are also mentioned.

II. A SUMMARY OF RESULTS OF RESEARCH ON EARTHQUAKE SOURCES OF SEISMIC RADIATION AND EARTHQUAKE - EXPLOSION DISCRIMINATION.

1. Theoretical Investigations

The major emphasis of the theoretical work was the detailed development of the analytical representation of the radiated elastic wave field from earthquakes, with the field expressed in terms of the fundamental physical variables for such events. The propagation of this field in the near to far field distance ranges, with the medium representative of the earth's actual structure, was also investigated as a separate theoretical effort. The results of these theoretical studies were then merged to provide predictions of the character of the radiation field to be observed in both the near and far field ranges. The principal results of this work are as follows:

(a) Formulation of Representation Theorems

Formulation of the general representation theorem (Green's function solution) for a stress relaxation source in an arbitrarily prestressed medium, this result describing spontaneous failure in a prestressed medium. The generality of the representation theorem obtained is actually such that dislocation and stress pulse equivalent sources, as well as externally applied forces, are represented. This result serves as a basis for most of the source calculations carried out in this study. (References: Minster, 1973; Archambeau and Minster, 1975a)

(b) Energy Considerations

Consideration of the conservation of energy as well as momentum, the latter resulting in the representation theorem mentioned above, for processes of failure in a prestressed medium has led to the description of the nonlinear processes in terms of a generalized phase change, wherein the boundary of the failure zone is described as a moving phase boundary in a prestressed medium. The concept and approach is natural to continuum theory descriptions of irreversible processes of failure wherein the medium suffers a permanent change in physical properties upon failure. The application of the conservation of energy, momentum and mass at the

failure boundary leads to coupling between the relations for energy and momentum conservation as well as complex "jump conditions" at the failure boundary which prescribe the failure boundary growth with time (i.e., the rupture velocity). These theoretical results are complimentary to the representation theorem for the radiation field from the seismic source, described in (a). In particular, exact solutions require solution of the "jump conditions" simultaneously with the evaluation of the representation theorem in order to determine the radiated stress wave field from an earthquake. Subsequent work reported here aims at reasonable approximate solutions to the full coupled problem posed by these results. (References: Archambeau and Minster, 1975a, b; Minster, 1973)

(c) Equivalence Theory

In the special case of an instantaneous failure it was shown that both dislocation and stress pulse equivalent sources can be constructed such that they produce elastic radiation fields that are identical to those from the relaxation source representation. Thus it was shown explicitly that the commonly used dislocation and stress pulse equivalents can be constructed to yield the same radiated field as a relaxation source in a prestressed medium, however it was also shown that equivalents are in general quite complicated with the dislocation displacement discontinuity or applied boundary stress pulse required to be a function of position along the equivalent failure surface. Further, for realistic conditions, it is found that specification of the equivalent displacement or stress "dislocation" cannot be made without first solving an integral equation involving the initial stress field. In effect, this requires a solution of the relaxation problem prior to construction of the exact dislocation equivalent (of displacement or stress pulse type).

Along the same lines, it was pointed out in quantitative terms that the radiation field from any seismic source whatsoever can be represented by an equivalent point source composed of a superposition of point multipoles. (This had earlier been demonstrated by Archambeau, 1964, 1968.)

Taken together the equivalence results proved to be extremely useful as well as important in clarifying the relationships between the various source representations. In particular, the point source equivalence was used to express source fields in computer programs which then compute the effects of propagation of the field in complex media, representative of the earth. Further, the results provide support to the modeling approach commonly used to fit observed radiation fields from earthquakes wherein a spatial array of dislocations, along a fault zone, are employed to achieve a fit to observations, by choosing different displacement offsets or stress pulses and time functions for each of the individual dislocations. In this case the equivalence theory explicitly shows the approach to be valid and provides a basis of interpretation for the inferred dislocation results in terms of the prestress field and the failure process. (References: Minster and Archambeau, 1975a; Minster, 1973).

(d) Radiation Field Solutions for Relaxation Models

Solutions for the radiation fields from relaxation source models were obtained by evaluating the integral Green's function solution resulting from the representation theorem. A number of approximations are involved and a variety of source models were used in an effort to produce reasonably precise predictions for the elastic wave radiation from earthquakes while still allowing the integral solution to be evaluated analytically. Specifically, the representation theory integral solution was simplified by:

(1) Neglecting dynamic scattering of waves from the failure zone boundary during failure growth. This is termed the "transparent source" approximation.

(2) Decoupling the momentum and energy equations, where the coupling is affected through boundary conditions and the growing failure boundary surface, by the expediency of independently specifying the rupture growth rate, that is the rupture velocity, and treating this quantity as an

adjustable parameter in the results. Thus the failure growth rate, while in reality being controlled by dynamical energy balance and momentum transfer, is described parameterically a priori, so that the solution of the full complex (and nonlinear) coupled problem is avoided. In this case the radiation field is explicitly dependent on the assumed rupture growth parameters.

The justification of these simplifying approximations is quite straightforward; the first is the neglect of the second order scattering effects which are certainly small, while the second simplification, in principle, only postpones the considerations of energy balance and renders the predictions of the radiated field less deterministic, inasmuch as they are expressed in terms of a basically unknown rupture velocity, which must later be interpreted in terms of energy balance.

The earthquake failure zone and prestress field spatial characteristics were modelled or represented parameterically with the objective of permitting closed form analytic solutions for models with the essential spatial characteristics of an earthquake. Specifically, the models used employ:

(1) An expanding or moving spherical failure zone constrained to translate in space and/or grow in such a manner as to sweep out an ellipsoidal failure zone.

(2) Specification of the change in elastic properties of the material within the moving-growing failure zone volume, where the elastic properties change in some particular way due to the failure process which may be viewed as a generalized phase change. In all the models it was assumed that melting was a part of the failure process (e.g., as a secondary effect of failure) and hence that the rigidity modulus vanished, at least in a transient sense, within the failure volume.

(3) A variable spatial stress dependence such that the prestress field

is characterized by largest values in the failure zone with decreasing values away from this region. This condition is approximated for purposes of analytical tractability by taking a uniform prestress level over an infinite region, evaluating the dynamical relaxation of this stress field over the failure zone growth interval and then explicitly deleting contributions to the radiated field from the region far from the failure zone. In particular, contributions from the region outside a sphere of radius R_g are deleted. In effect, the prestress spatial variation is thereby parameterized by R_g .

While these largely geometrical approximations are not a part of the theory itself, they lead to a relatively simple analytical evaluation of the radiation field with modeling conditions and approximations that are reasonably representative of the physical situation. (Most of the new and continuing work is, however, designed to obtain solutions under less restrictive approximations and for model geometries that are more sophisticated.)

Some essential theoretical results obtained using the model approximations given can be summarized as follows:

(1) The P and S wave spectrums for all earthquake models are strongly dependent on the following model parameters: V_R (the assumed uniform rupture velocity), L (the maximum failure zone dimension), $\sigma_{ij}^{(0)}$ (the initial prestress level), μ' , λ' , ρ' (the elastic moduli and density of the material after failure, taken in current models as $\mu' = 0$, $\lambda' = \lambda$, $\rho' = \rho$ with λ and ρ the values before failure) and R_g (the spatial "stress concentration" distance factor). The far field displacement spectral shapes are characterized by a nearly flat spectral level to high and low cut-off or corner frequencies, f_c^H and f_c^L , given approximately by:

$$2\pi f_c^H \sim \frac{V_R}{L} \left[\frac{3V_{p,s}^2}{V_R^2} \right]^{1/3}$$

$$2\pi f_c^L \sim \frac{V_{p,s}}{R_s} \left[\frac{10}{1 - 3/5 (L/R_s)^2} \right]^{1/2}$$

where $V_{p,s}$ denotes either V_p or V_s , which are the compressional and shear velocities in the medium surrounding the failure zone. For compressional wave spectra V_p is used, with V_s used for S waves. At frequencies above f_c^H the displacement spectra decrease, becoming asymptotic to $1/f^3$ for $f \gg 1$. At frequencies below f_c^L the spectra decrease as f^2 , for $f < 1$ and $f \ll f_c^L$. Hence the general spectral shape for P and S waves alike is a nearly flat spectral region, with decreasing spectral amplitudes for $f < f_c^L$ and $f > f_c^H$ on either side of the flat zone. Clearly then, the spectrum can be strongly peaked if f_c^L and f_c^H are close in value, and this amounts to R_s being not much larger than L , with V_R similar in magnitude to V_p or V_s . On the other hand for R_s large, f_c^L will be small and the spectra will be flat for $f < f_c^H$, and therefore quite possibly to very low frequencies.

Note that P and S wave spectra will have different "cut-off" frequencies f_c^L and f_c^H . We can characterize the spectral dependence on the other parameters in terms of the displacement spectral amplitudes A_p , for P waves and A_s for S waves. We find that:

$$A_s/A_p \propto \left(\frac{V_p}{V_s} \right)^3$$

so that the S wave radiation is commonly about five times as large as for P waves.

Further both P and S wave spectral amplitudes, at all frequencies, scale as the cube of the failure zone dimension, that is:

$$A_p \propto L^3 ; \quad A_s \propto L^3$$

and directly with the prestress, so:

$$A_p \propto |\sigma_{ij}^{(0)}| ; \quad A_s \propto |\sigma_{ij}^{(0)}|$$

The scaling with the initial prestress is modified to a linear scaling of the spectra with stress drop, rather than prestress, in case $\mu' = 0$ is not used. In particular, if $\mu' \neq 0$ but is approximately uniform within the failure zone, then it can be shown that the stress within the failure zone is also uniform and equal to τ'_{ij} , say. In this case we have;

$$A_p \propto |\sigma_{ij}^{(0)} - \tau'_{ij}| ; \quad A_s \propto |\sigma_{ij}^{(0)} - \tau'_{ij}|$$

(2) The spectral shapes of the far field displacement spectra are dependent on the angular position of the observation point relative to the failure zone orientation. In particular, the high frequency corner frequencies for P and S waves vary with angular position, with f_c^H for P waves generally higher than that for S waves, but in some directions f_c^H for S can be larger than f_c^H for the P wave. The variation is relatively complex and is due, mainly, to rupture propagation.

(3) The spectral slopes at high frequencies, $f > f_c^H$, are quite strongly dependent on V_R , the rupture velocity. For low rupture velocities, the

slope varies gradually approaches $1/f^3$, attaining this slope at frequencies much higher than f_c^H ; so that the spectral slope can appear to be $1/f$ to $1/f^2$ for frequencies near to and considerably larger than f_c^H . For rupture velocities that are quite high, yet less than the medium shear velocity V_s , the spectral slope steepens rapidly for $f > f_c^H$, so that the gradual change in slope noted for low rupture velocity events is not apparent in the high rupture velocity spectra. However, as the rupture velocity approaches the intrinsic elastic velocity for the material (i.e., either V_s or V_p) the frequency at which the spectra attains the $1/f^3$ slope moves to higher and higher values. For the cases in which the rupture velocities are equal to or larger than one of the elastic velocities, then the spectrum of the wave type for which V_R is supersonic never reaches the $1/f^3$ asymptotic slope, and the spectral slope is $1/f^2$ for $f > f_c^H$. The P and S wave spectra behave in basically the same way with changes in V_R , except that what is meant by large and small values of V_R is based on the magnitude of V_R relative to V_p or V_s . Hence, a particular V_R value can be large for S waves and quite small for P waves - with the individual wave spectra therefore having high frequency slope characteristics which are quite different from one another.

(4) The theoretical results yield predictions for both the "near" and "far field" radiation from the source. The far field spectra have the character described above while the "near field" components have a spectral and spatial dependence that is quite different than that for the far field. In particular, if the P and S waves are considered separately, then the near field components of these waves have a spectral dependence with frequency that is approximately $1/f^3$ for both wave types. Thus if the wave types could be separated in the near field distance range (actually they cannot be

separated since they overlap in time), they would give spectral estimates that become infinite at zero frequency like $1/f^3$. Since the two wave types are not separated in the near field, then if they are considered together theoretically, the overall dependence of the spectrum is as $1/f$ with frequency. This is the expected result, in that it gives a net static offset in the zero frequency limit (i.e., the $1/f$ dependence of the P + S displacement spectra means that, as $t \rightarrow \infty$, the displacement will have a net offset from zero in the time domain). Since both the "near" and "far" field spectra are observed in superposed form at all distances, but with the near field component only very important in the near distance range from the source (since it decreases as a higher power of $(1/r)$ with distance compared to the "far field" component) it is appropriate to consider the total spectrum (both near and far field terms added) especially at distances close to the source. Thus in terms of observed spectra, the summation of the near and far field spectra results in a superposed $1/f^3$ (or $1/f$, for P plus S waves) spectral shape on the previously described far field spectra. At large (teleseismic) distances the effect of the $1/f^3$ or $1/f$ near field spectral shapes is very small and can be seen only for $f \ll 1$. Coupled with the filtering of most seismometers then, the near field component is not usually observed and hence can usually be neglected. For distances of observation closer to the source the near field becomes important and the spectra at low frequency is more and more dominated by the $1/f^3$ or $1/f$ near field component. In particular, the low frequency spectral decrease for $f < f_c^L$ can be strongly affected and at most near field distance ranges the composite spectra will decrease for $f < f_c^L$ and then begin to increase as $1/f$ or $1/f^3$ at some intermediate frequency, $0 < f < f_c^L$. This yields spectra that have a low frequency dip or minimum followed by an increase as $1/f^3$ or $1/f$ to zero frequency; the latter

rate of increase depending on whether the individual P or S wave spectra are considered, or whether the total P plus S wave spectrum is considered. At distances very near the source, the near field spectra will completely dominate and a spectrum behaving as $1/f^3$ or $1/f$ occurs.

(5) The radiation patterns for the P and S waves are dominated by the quadrupole term at the low to intermediate frequencies ($f < f_c^H$). Thus in this frequency range the earthquake appears to be a simple quadrupole (or double couple) radiator. At higher frequencies, $f > f_c^H$, higher order multipoles contribute significantly in such a way as to produce "distorted quadrupole-like patterns" where the distortion is such that amplitudes in the direction of rupture propagation (or opposite to it) are larger relative to the other lobes of the pattern. Thus at high frequencies the amplitude radiation patterns can be highly distorted from quadrupole patterns due to rupture propagation effects. The radiation patterns for the initial phase, viewed in terms of the phase at a given frequency for a range of frequencies, show a behavior similar to that of the spectral amplitude. That is the phase changes sign as a function of azimuth as a quadrupole for $f < f_c^H$. At high frequency the phase pattern shows distortion from the simple quadrupole variation but not to the same degree as does the amplitude patterns. In particular, the nodal lines, bisecting regions of opposite phase (different by 180°) for the simple quadrupole radiation are not strongly distorted in the high frequency range by rupture propagation effects, so the quadrupole-like change in phase from quadrant to quadrant is maintained even though the phase value itself within the individual quadrants, is somewhat different from that for a pure quadrupole. Hence the initial motion in each quadrant sector will show a variation between quadrant sections similar to a quadrupole. Thus, fault plane solutions obtained at high frequency would not differ appreciably from

those at low frequencies. Further the phase distortion in the high frequency seismic band (below 3 cps) is not so large as to change the polarity of first motion. (References: Minster and Archambeau, 1975 b; Minster, 1973; Archambeau, 1974; Archambeau, Harkrider and HelMBERGER, 1974.)

(e) Computer Based Earthquake Field Simulation

The analytical representations of earthquakes in terms of relaxation source models have been incorporated in a series of linked computer programs designed to predict the seismic radiation at any point in the earth. Specifically, a variety of relaxation models are used to predict the radiation from the earthquake itself. This direct field is expressed as a multipole field and used with surface wave (Rayleigh and Love) and body wave programs to determine the spectrum and time domain displacement, velocity and acceleration in realistic earth models. Complete synthetic seismograms at both teleseismic and near source distance ranges can be produced. The surface wave propagation programs employ a layered half space approximation, with both the near and far field terms retained in the calculation for all orders of multipoles. The body wave calculations employ the Haskell matrix method at the source and receiver sites in order to accurately account for complex crustal structure with this computational method then being coupled to higher order ray theory calculations for propagation in the earth's mantle. Lateral variations in earth structure are also incorporated in the wave propagation computations. In the near field region only the Haskell method or a Cagnaird method are used to predict the propagational effects. Both the elastic and anelastic properties of the earth are accounted for in all the calculations. In particular the attenuation and dispersion introduced by anelasticity are included. For teleseismic body waves, especially, it is found that anelastic dispersion has a strong effect on both

the travel time of the phases and on the wave form. (References: Minster and Archambeau, 1975b; Minster, 1973; Cherry, Bache, Archambeau and Harkrider, 1973; Archambeau, Harkrider and Helmberger, 1974.)

(f) Predictions of $m_b - M_s$ for Earthquakes and Explosions and Investigations of New Discrimination Methods.

The coupled source representation and wave propagation programs were used to generate synthetic seismograms for teleseismic distances from which theoretical m_b and M_s values were computed. The procedure followed was exactly that used to obtain magnitude values from observed data. A set of earthquake models were used with a range of fault lengths from 1 km up to 20 km in various prestress environments ranging from .01 kbar to 1 kbar in magnitude and with spatial "stress concentration factors", R_s , ranging from 10 km (for the small events) up to 500 km. R_s values used were always at least 5 times the rupture length L . All earthquakes were dip slip events at 10 km depth with rupture velocities fixed at $.9 V_s$. Predicted m_b and M_s values were obtained as a function of fault length, prestress and R_s value and plotted in the $m_b - M_s$ plane. The parameter variations for the earthquakes generate a population of $m_b - M_s$ values occupying a band in this parameter space. It was found that for large events the $m_b - M_s$ population trend is such that the mean and boundary lines for the population have slopes significantly greater than one, becoming steeper with increasing m_b in a plot of M_s as a function of m_b . At lower m_b values, (less than m_b about 5) the boundary and mean lines for the population all have slopes of unity. However, it was found that the earthquake population could be very dispersed in this population space, partly due to the methods used for magnitude measurements, but fundamentally because of the expected variations in prestress

(or stress drop), rupture velocity and R_s value - that is variations in the spatial variability of the prestress. Most german to the discrimination problem are the variations producing anomalous earthquakes that appear explosion-like in this parameter space. It is found that at large magnitudes ($m_b > 5$) the events having high rupture velocity and large prestress level (or stress drop) are most explosion-like. In order for such an event to be within the explosion population, the prestress and/or stress drop accompanying the event would have to be larger than about 2 kbars with a rupture velocity very near the shear wave velocity or larger. At low magnitudes ($m_b < 5.0$), neither prestress nor rupture velocity have much affect on the event position in the $m_b - M_s$ plane, since the $m_b - M_s$ population trend has unit slope in this range. However, the spatial stress variation can have a profound effect on the dispersion or spread of the population. In particular, events with R_s values such that f_c^L is at significantly higher frequency than the .05 cps. frequency, near which surface wave magnitudes are measured, will have low M_s values relative to their m_b value. Hence if some (or most) small events are limited in size because the prestress field is only large near the hypocenter and rapidly decreases away from this region, thereby limiting the spatial extent of failure, then rather low M_s values will occur with normal or even high m_b magnitudes. With a range of R_s values for different events, from large to rather small values, a wide variation of M_s values would occur yielding a scatter of event points, those of lowest M_s value being near or possibly within the explosion population. Thus, the anomalous events at low m_b magnitudes are those occurring within strongly inhomogeneous stress zones with high stress levels locally concentrated at the point of initial rupture.

The mean line for the entire population of events has, as previously noted, a slope of unity at low magnitude which gradually increases with increasing m_b , becoming noticeably steeper at $m_b \sim 5$, reaching a slope of 2 around

$m_b \sim 6.0$. The slope of the mean curve continues to increase beyond $m_b \sim 6.0$. (To date the largest event studied had $m_b \sim 6.5$.) The origin of this behavior can be understood from the spectral properties of earthquake radiation. That is, for all the low magnitude events, the high frequency cut-off, f_c^H , is at a frequency larger than both .05 cps and 1 cps near where the M_s and m_b magnitudes are computed. Thus, in this range of event magnitude both m_b and M_s are measured in the frequency range where the spectrum for both P and S waves is generally flat. Hence, in this range, both m_b and M_s will both scale in the same way with increasing rupture length or prestress and rupture velocity variations have no effect, so long as no extremely low velocities occur. However, if the low frequency cut-off f_c^L for the event is such that it lies between .05 cps and 1 cps, then the M_s value will be depressed due to the spectral fall-off at $f < f_c^L$. Then, as previously described, the M_s value will be "anomalously small" relative to the $m_b - M_s$ values for events with larger R_s values, such that $f_c^L < .05$ cps.

At magnitudes between 4 and 5 the m_b measurement near 1 cps is near the high frequency cut-off f_c^H . Thus, for events with f_c^H lower than 1 cps and larger than .05 cps, the m_b value does not increase as fast as the M_s value since the spectrum decreases above f_c^H in the frequency range where the m_b is measured. This causes the whole population trend to bend upwards in a plot of M_s vs m_b . For sufficiently large earthquakes a measurement of m_b at 1 cps will be made in the spectral region where the slope of the P wave spectrum is $1/f^3$. If the m_b measurement is made precisely at 1 cps (by a filtering method) then for larger events of greater fault dimension, no increase in m_b would be observed. This is because the spectra scale up

in magnitude as the cube of the fault length, while f_c^H scales inversely with the fault length. In this case, the high frequency spectra with slope of $1/f^3$ remains the same for all these large earthquakes and amplitude measurements made in this spectral region do not change with increasing event dimension. The net result is then that the m_b magnitude will have a cut-off value and the mean M_s vs m_b curve will become vertical. The cut-off value is a function of the prestress and rupture velocity, the higher the prestress level the larger the m_b cut-off value and similarly for rupture velocities below the shear wave velocity. If the rupture velocity can be supersonic (actually equal to or greater than the P wave velocity) then no m_b cut-off occurs, since the spectrum never assumes the $1/f^3$ slope, but instead varies as $1/f^2$ at high frequencies.

In practice m_b is never measured precisely at 1 cps in the time domain and in fact it is common for the measurement to be made at lower and lower dominant frequencies for larger and larger events with the correction applied assuming a linear dependence rather than cubic. This has the effect of removing any cut-off in m_b for large events, so that observed M_s vs m_b populations for large events commonly show only a steepening of the distribution, so that a mean curve for the large magnitude events usually has a slope of around two, or only somewhat higher.

A similar study of the magnitudes of the theoretical underground explosions was made in order to compare these predictions to those for earthquakes, as well as to compare the results to observations. The theoretical explosions were

generated from a finite difference calculation which included vaporization, plastic flow, cracking and pore collapse. The finite difference calculation was carried to a time for which the wave field had propagated to a distance such that the material behavior was linear. At this point the calculation was terminated and the wave field was sampled in space and time. Using this sampling, an equivalent multiple point source was generated with the property that the numerically calculated wave field in the elastic zone was reproduced. This equivalent multipole seismic source was then used in the elastic wave propagation computational programs to predict the near and far field spectra, for individual wave types, and near and far field synthetic seismograms. This latter procedure is precisely the same as that used for earthquakes but in this case, for explosions, the equivalent source representation is much simpler.

For the simple explosion with no tectonic release or source geometry asymmetries, the equivalent source is a monopole. The far field displacement spectrum associated with this monopole is essentially flat from zero frequency to the cut-off or corner frequency, f_c^H . The spectrum can be slightly peaked, this being dependent on characteristics of the medium. The corner frequency f_c^H is above 1 cps. for yields of 1 megaton and less, for ordinary rock materials. Its specific value is a function of material type, porosity etc. This characteristic frequency scales inversely with the time of formation of the nonlinear zone, that is:

$$f_c^H \propto V_R/R_0$$

with R_0 the radial dimension of the nonlinear zone and V_R an effective

rupture velocity, which is near the compressional velocity of the medium. The spectral slope for $f > f_c^H$ is between f^{-2} and f^{-3} , generally close to f^{-2} . This slope value is also dependent on the material type, but is generally near to f^{-2} .

Using the synthetic seismograms, m_b and M_s values were computed using the standard formula. As with the earthquakes however, the standard formulas for event magnitude admit of a range of possible measured periods and/or pulse cycles. This range of possible measurements was used in order to establish a range of magnitudes that could be, in practice, assigned to the theoretical events (for both the theoretical earthquakes and explosions). For all theoretical events however, M_s measured at 20 sec. period and m_b measured from the first cycle of motion were used as reference measurements with all other possibilities of measurement (e.g., M_s measured at 17 sec.) used to establish variance bounds on the $m_b - M_s$ measurements. The $m_b - M_s$ values for a range of explosions of different yields and at different depths of burial (depths sufficient to provide containment) were plotted and compared to observations from NTS. A material "typical" of NTS shot media (i.e., similar to granite or welded tuff) was assumed for the explosion medium environment in all cases. The theoretical $m_b - M_s$ curve fell within .1 to .2 magnitude units from the observed mean $m_b - M_s$ line for NTS events, over the entire m_b range from 3.5 to 6.5. The theoretical curve was slightly higher (M_s values somewhat higher and m_b values somewhat lower) than the observed mean curve, but this was expected in view of the somewhat higher rigidity of the material assumed for the medium surrounding the explosions in the theoretical calculations compared to the average material at NTS.

The effects of tectonic stress on the $m_b - M_s$ results were also investigated by addition of a uniform non-hydrostatic prestress of 165 bars

to the medium. The radiation effects were calculated from the relaxation of prestress around the shatter zone created by the explosive shock wave, with the shatter zone radius estimated from the size of the nonlinear zone determined by the shock wave calculations. The effects of tectonic release were primarily to increase the M_s value measured. For the largest event (100 kt), the M_s value increased by approximately .6 units, this being due to the large shatter zone created by the explosion. For the smallest explosion studied (1 kt), the increase in M_s was less than .1 magnitude unit.

The perturbation of the theoretical $m_b - M_s$ values due to tectonic release were sufficient to explain the relatively few explosions observed with anomalously high M_s values relative to the average $m_b - M_s$ curve for NTS explosions. Thus, while tectonic release due to shatter zone creation is not the only mechanism available to explain anomalous explosions with "high" M_s values and hence most earthquake-like, it is an explanation consistent with all the observations, including: the lack of observations of seismically significant faulting at the explosion site; the observations of large Love waves from explosions; and perturbations in the P wave train which would correspond to the addition of sP from the tectonic release.

The theoretical $m_b - M_s$ results for explosions without tectonic release and in the same medium but with different yields and depths of burial could be fit with a line of unit slope in the $m_b - M_s$ plane. With the addition of tectonic release the curve through the $m_b - M_s$ points tends to steepen somewhat for large yield events such that the slope becomes greater than unity (M_s plotted on the vertical axis). The separation of the theoretical explosion, $m_b - M_s$, from the theoretical results for earthquakes is such that the extreme bound of the earthquake population is from .7 to 1.5 magnitude units from the explosions in the $m_b - M_s$ plane. The separation is largest at the high magnitudes and converges to near .7 at low magnitudes, near $m_b = 4.0$. However, these results apply to explosions without tectonic release and for earthquakes with stress drops below 1 kb, with rather large R_s factors.

If explosions with appreciable tectonic release effects (prestress near 165 bars) are included as well as earthquakes with stress drops of the order of 2 kb, then the explosion-earthquake populations can overlap slightly at large magnitudes ($m_b \approx 6.0$ and greater). If small R_s factors are possible, which could be the case for small magnitude earthquakes, then such earthquakes will have anomalously low M_s values. In this case, the part of the earthquake population consisting of low R_s events can overlap the explosion population. As suggested earlier, it would be expected that this would most likely occur at low magnitudes ($m_b \leq 5.0$). Specifically, an earthquake with a 1 km fault length and $R_s = 30$ km will yield m_b and M_s values ($m_b = 3.2$ and $M_s = 1.2$) well within the explosion population. Larger events will give $m_b - M_s$ values within or near the explosion population if the spatial stress concentration factor, R_s , associated with the event is less than the wave length of Rayleigh waves in the period range from 17 - 22 sec (about 60 km). R_s values less than 60 km could be expected to occur, at least occasionally, for earthquakes with $m_b \leq 5$.

The results of the joint theoretical investigation of the seismic radiation from explosions and earthquakes, expressed in terms of $m_b - M_s$ values and event P and S wave spectra, shows that the separation of earthquake and explosion event populations in the $m_b - M_s$ plane is due to a combination of factors, namely:

- (a) Explosions are richer in high frequency P wave radiation than earthquakes with the same low frequency P wave amplitude level as the explosions. This is due to the fact that f_c^H , the high frequency corner or cut-off frequency, is larger for the explosion than for an

earthquake with a comparable low frequency spectral level. This, in turn, is due to a higher effective rupture velocity and a smaller source dimension for explosions compared to earthquakes with the same low frequency levels. In addition the high frequency ($f > f_c^H$) slope for the explosions is close to f^{-2} , while it is, generally, close to f^{-3} for earthquakes, so that this also contributes to the enrichment of the high frequency radiation of explosions relative to the comparable earthquakes. This slope difference is due to the high effective rupture velocities (characterizing the time of formation of the entire nonlinear zone) for explosions, as compared to the much lower rupture velocities characteristic of earthquake failure zone formation.

(b) An earthquake with the same low frequency P wave spectral level as a selected (comparable) explosion will have a S wave spectrum with a maximum of from three to five times the maximum of its P wave spectrum, while the S wave spectrum from the explosion is entirely absent, or even with tectonic release or source asymmetry effects, is at most of the same order as the explosive generated P wave maximum. This is due to the fact that earthquakes can be thought of as being due to failure under shear and consequently most of the energy release is in the form of shear waves. On the other hand an explosion is intrinsically compressional, where the seismic wave is the result of conversion of a compressional shock to a compressional elastic wave.

To understand the separation of these two kinds of events in the $m_b - M_s$ plane then, it only is necessary to observe that since the m_b value is obtained from a P wave amplitude measurement at high frequency, near 1 cps., then an explosion will have a higher m_b value than will a comparable earthquake

(having the same low frequency P wave spectral level) due to the high frequency enrichment noted in (a). In addition however, the M_s value is measured from the Rayleigh wave amplitude near .05 cps. and since this amplitude is a function of both the P and S wave excitation from the source, then the earthquake will have a higher M_s value than the comparable explosion due to the enhanced S wave production of the earthquake as described in (b). The $m_b - M_s$ separation of the two event populations is therefore due to the combined effects, tending to make the earthquakes have larger M_s values and the explosions larger m_b values for comparable events with the same low frequency P wave radiation.

In order to define a discriminate with greater intrinsic detection capability and equal or greater separation of event population between both single and multiple explosions and earthquakes, the spectral differences described in (a) were utilized. Specifically a P wave spectral discrimination method was devised that was simple, so that it could be easily implemented, and yet took advantage of the earthquake explosion spectral differences. The approach taken was to use "spectral magnitudes", that is m_b values, computed from ultra-narrow band filtering of the P wave train at center frequencies over the range from about .2 cps. to 6 cps. These magnitudes are denoted $\bar{m}_b(f)$ and are computed from the maximum in the envelope of the narrow band filtered P wave train. For optimal discrimination of events, noise reduced envelope amplitudes are used. Such magnitudes were computed for the synthetic earthquakes and explosions previously described along with a variety of multiple explosions made up of combinations of the single theoretical explosions. In general 10 frequencies were used in the frequency range $.2 \leq f \leq 6$ cps. The events were then viewed, as single points, in the $\bar{m}_b(f)$ parameter space. It was found that

theoretical explosions of both single and multiple type define a population in this space that is well separated from the earthquake population. The principal basis of this separation is the high frequency enrichment of the explosion signals relative to comparable earthquakes, but in addition, the effects of interference between the phases P and pP for the very shallow explosions results in a peaked spectrum for the composite P + pP phases, with depressed low frequency spectral level and this further enhances the separation of the event classes.

In practice the event populations are projected on planes through the N-dimensional $\bar{m}_b(f)$ space and viewed in the planes $\bar{m}_b(f_1)$ vs $\bar{m}_b(f_2)$ with $f_1 < f_2$. The event populations in these planes are similar to the populations viewed in the $m_b - M_s$ plane, but in general with wider separation between populations. In particular, for planes with $f_1 \ll f_2$ (e.g., $f_1 = .3$ cps, $f_2 = 3$ cps) the separation of multiple and single explosions from earthquakes is from near 1.0 to above 1.5 magnitude units over the entire range studied, from $m_b \approx 3.0$ to $m_b \approx 6.5$, the separation being largest at the large magnitudes. In general, with f_1 fixed at some "low" frequency (e.g., .5 cps) and f_2 allowed to vary, the population separation increases with increasing f_2 . This is due to the high frequency enrichment for explosions. For f_2 fixed at some "high" frequency (e.g., 3 cps) and f_1 allowed to vary, the population separation increases with decreasing f_1 . This is due to the P - pP interference for explosions. Here $\bar{m}_b(f_1)$ for explosions decreases as f_1 decreases while it remains nearly constant for earthquakes as f_1 decreases, so long as f_1 does not decrease to values below f_c^L (the R_s induced low frequency cut-off).

These theoretical predictions were tested against a large group of Eurasian earthquakes and explosions as recorded

at LASA and NORSAR. More than 200 events were processed and the resulting $\bar{m}_b(f)$ data yielded results in close agreement with the theoretical predictions. Noise however limited the band width that could be used and the separation of event populations was somewhat less than 1 magnitude unit for the frequencies used. In any case, this discriminant has been reasonably well verified using a large group of events. In particular, all explosions (about 60) were identified as explosions by this discriminant, including the smallest explosion of $m_b < 4.0$. Only earthquakes deeper than 70 km sometimes fell into the explosion population, with most of the explosion-like earthquakes being at depths of around 300 km. All the explosion-like earthquakes can therefore be easily identified as earthquakes by standard location methods.

The value of the frequency dependent body wave magnitude discriminant lies in its simplicity and, of course, in the fact that all shallow earthquakes are well separated from both multiple and single explosions. In addition however signal detection and implementation of this technique can be made at very low magnitudes, near $m_b = 4.0$, using teleseismic receivers. Further only vertical component short period detectors are required and these can be operated at high gain levels with minimum maintenance and cost. Finally the possible convergence of the $m_b - M_s$ populations due to low R_s values, for relatively small earthquakes, need not occur when the event populations are viewed in the $\bar{m}_b(f)$ space. That is, the effect can easily be avoided for the $\bar{m}_b(f)$ discriminant by using a proper frequency band in which all events of interest (e.g., $m_b > 3.5$) are to be viewed.

Finally an interesting and useful result occurs when $\bar{m}_b(f)$ discrimination is applied to pure seismic noise. In this case the spectral magnitudes for the noise fall within the shallow earthquake population. Hence if explosion signals are to be detected and identified by an on-line processor, we can

continuously monitor time segments of incoming receiver output (e.g., 50 sec sections and only when an explosion, multiple explosion or very deep earthquake signal is encountered will the "event" location in the $\bar{m}_b(f)$ space move into the explosion-like region. This therefore implies that this method can be used to continuously monitor incoming data to detect and identify explosion-like signals. Since the processing involved can be accomplished at about 1/10 real time, this is a very attractive possibility.

In addition to the body wave spectral magnitudes, similarly defined spectral surface wave magnitudes $\bar{M}_s^R(f)$, for Rayleigh waves, and $\bar{M}_s^L(f)$, for Love waves, were computed from the synthetic surface waves from the theoretical explosions and earthquakes. A variety of discriminates were applied using the multi-dimensional parameter space defined by the sets $\bar{m}_b(f)$, $\bar{M}_s^R(f)$ and $\bar{M}_s^L(f)$. In particular the events were viewed in $\bar{M}_s^R(f)$ vs $\bar{m}_b(f)$ planes which is similar to the ordinary $m_b - M_s$ plane, and $\bar{M}_s^L(f)$ vs $\bar{m}_b(f)$ planes. In general the population consisting of single and multiple explosions were well separated from the shallow earthquake population. It was found, at least theoretically, that considerable improvement in the event population separation could be achieved using these spectral magnitudes rather than the standard $m_b - M_s$. No complete verification of these predictions have been made using recorded events, but such verification is being pursued.

Use of the spectrally defined magnitudes is clearly a powerful approach to discrimination and the results so far are extremely encouraging. With additional exploration of the spectral magnitude parameter space, a multi-discriminate method will evolve which should give an optimal event identification procedure. (References: Archambeau et al., 1974; Cherry et al., 1974; Savino and Archambeau, 1975)

(g) Comparisons with Numerical Models of Earthquakes

The theoretical predictions of the radiation from the transient motion model used in the relaxation source theory was compared to results from a two-dimensional numerical model of an earthquake computed by Cherry. Cherry's model involved slip on a plane, which occurred when a failure condition was met and continued until the stress on the fault plane was balanced by frictional forces, at which time the fault was locked. The coefficients of friction (dynamic and static) used by Cherry were of the order of those observed in rock mechanics experiments. Preceding failure Cherry assumed an epoch of plastic deformation, initiated at a stress level equal to the failure stress level with failure (or slip on the failure plane) occurring only after a finite amount of plastic work had taken place.

Taking a stress level sufficient to cause failure, the fault was allowed to grow at its own rate, as determined by the failure condition and the dynamic transfer of momentum and energy. The resulting radiation was monitored at a number of points close to the fault. The spectrum of the complete displacement history at various points in the grid was then computed.

Using the rupture rate obtained by Cherry, as well as the rupture length and prestress levels used in the model, the radiation field was computed using the relaxation theory model. A comparison of the displacement spectra with those from the numerical model showed that the spectra were very similar, with "corner frequencies", f_c^H , and amplitude levels at this frequency essentially the same. The high frequency, $f > f_c^H$, slopes of the spectra from the two models were both $1/f^3$ on the average. Maxima and minima in the high frequency spectra were present in the results from both models but were only roughly similar as to position and amplitude. The spectra at frequencies below f_c^H were both essentially flat for a short range of

frequency and then began to increase as $1/f$, with $f < 1$. The numerical model spectrum was somewhat different than the relaxation theory spectrum in this low frequency range however, in that the near field, $1/f$, behavior at low frequency began at a frequency closer to f_c^H for the numerical model. Hence while the general shapes of the two spectra are nearly identical in this range, the numerical results are offset upward in the range where the spectra increases as $1/f$. There are at least two possible reasons for this difference, the most fundamental reason being that the relaxation model is a three dimensional model while the numerical model is two dimensional. Since the static field in a two dimensional space falls off more slowly with distance than that in three dimensional space, one would expect just this kind of difference in the static near field spectrum, since it reflects a larger static offset for the two dimensional case at a particular distance. In addition, both theoretical models have difficulties with precision at very low frequencies, where the power is extremely low, and so both of the calculations are, to some degree, uncertain in this frequency range.

The differences between the two results however are not great and what differences do exist appear to be understandable in view of basic differences in the dimensionality of the models themselves. Since the differences are minor, one can conclude, at least tentatively, that details of the models such as fault or failure zone width and plastic work are not critical in the prediction of the general characteristics of the radiation. Thus, while the relaxation model geometry that was used involved a translating spherical zone of vanishing rigidity and hence transient melting in a thick zone, this geometric aspect did not result in a strong perturbation in the radiation when compared to a thin fault model. What does seem to be most important is the set of basic failure parameters, namely the rupture velocity prestress level and overall failure zone length.

Additional comparisons of relaxation theory models to numerical models are underway. In particular, a three dimensional numerical earthquake model of the same type as the two dimensional model has been run by Cherry and a comparison with relaxation theory model results will be completed soon. Up to now the numerical models have assumed a uniform prestress, in effect a constant nonhydrostatic prestress in an infinite medium. A second three dimensional numerical modeling in a strongly nonhomogeneous prestress field is planned and this will be compared to the predictions of the relaxation theory model with finite R_s in order to ascertain the accuracy of the R_s approximation. Further, more sophisticated relaxation theory models are being developed and will be tested against the numerical models.

The objectives of this comparative study is to determine, in a quantitative way, the importance of various effects and parameters, such as plasticity, that may be associated with earthquakes. Further this study is designed to verify the general applicability of relaxation source models and to determine the accuracy of the approximations introduced in the course of obtaining analytical solutions. Should the analytical theory prove accurate in the representation of the elastic radiation from very complex nonlinear failure models that can be simulated numerically, then we feel that it would probably be accurate for the representation of radiation from actual earthquakes. In view of the relative simplicity, flexibility and insight to be acquired from the use of an analytical solution, such a verification therefore receives high priority. (References: Cherry, 1973; Minster, 1973; Minster and Archambeau, 1975b; Archambeau et al., 1974)

2. Interpretive Studies: Comparisons of Predictions with Observational Data

a. General Comparisons with spectra observed in the Near Field Study

This work is largely still in progress, but some results and tentative

conclusions can be stated now. First, the spectra of entire seismograms generated by small earthquakes and recorded in the near field distance range show:

- (i) The high frequency slope for frequencies $f \gg f_c^H$ is "near" $1/f^3$ in rough agreement with relaxation source predictions. The uncertainties due to the required correction for attenuation and the contamination from noise make a strong conclusion as to the exact asymptotic slope value impossible. However, it is highly unlikely that the asymptotic slope is less than 3.
- (ii) Most spectra from the observed earthquakes showed a strong minimum in the low frequency displacement spectrum followed by a rapid increase in spectral amplitude toward zero frequency. In total, the part of such spectra that are largely uncontaminated by noise show a strong peak followed by the rapid increase in amplitude, as $1/f$ or $1/f^2$, to zero frequency. This type of spectra are essentially as predicted by relaxation theory models with a low value of R_s ; that is for an earthquake occurring in a high stress concentration zone. The spectral increase as $1/f$ to zero frequency is as predicted by the relaxation theory model, while the observations of $1/f^2$ (or steeper) slopes is judged to be due to various sources of noise contamination at low frequency. Because of the differing distance dependence of the near and far field components of the displacement field, the frequency at which the spectrum begins to increase as $1/f$, for $f < 1$, is dependent on the distance of the receiver from the source. Therefore spectra obtained from data recorded quite near the source can be monotonically increasing from high to low frequency with the near field spectrum completely dominating the spectral shape.

At increasing distance the far field component emerges more prominently. In general then, spectral shapes varying from monotonic increasing to strongly peaked or with a broad flat section can be expected to be observed with varying distance from the source. However, if the far field spectrum from earthquakes is always flat from zero frequency to the corner frequency f_c^H , then no peak in the spectra should ever be observed at any distance. The data however show that most of the events have a strong peak at intermediate frequencies. This behavior is characteristic of earthquake spectra with a strong peak in the far field spectrum. This is not the only explanation for such observations however, since interference between signals (e.g., P and pP, or in this case simply any strongly reflected P phase) can give a minimum in the spectrum at low frequency, which will result in a peaked spectrum. But since near field spectra from several earthquakes at various azimuths, locations and depths have been obtained, it does not appear likely that so many of the observations could be so similarly affected by such interference. Nevertheless, the possibility still exists.

On the other hand it would be expected that at least some earthquakes in the low magnitude range, $m_b < 5$, would have essentially flat far field spectra over the frequency range of observation, with a superimposed near field component varying as $1/f$ at low frequency. Such events would correspond to earthquakes in rather uniformly stressed regions, with an effective R_g factor that was larger than the wavelength of the lowest frequency radiation reliably recorded. The observations of the near field spectral do in fact show some spectra with no peaking at intermediate frequencies, but no earthquake shows such spectra at all azimuths and

distances. Because of noise levels at low frequencies possibly obscuring the spectral minimum, as well as near field contributions dominating the far field component, it is uncertain as to whether such flat looking spectra reflect the true source spectrum in any simple way.

In order to fully evaluate the near field spectral (and time domain) observations, a systematic quantitative comparison with relaxation source predictions is underway. This process is difficult and tedious since it is still important to accurately account for structure effects in fitting the data and it has been difficult to obtain reliable structure determinations. Nevertheless this approach should eventually provide quite firm results.

(iii) Observations of the seismic moment for a given earthquake in both the near and far field distance ranges, with measurements made in two widely different frequency ranges, have given moments that differ by about an order of magnitude. Specifically, the low frequency moment is about an order of magnitude less than the high frequency moment. [McEvelly and Johnson, 1974 and Turnbull, 1974; reported at the Near Field Meeting, California Institute of Technology, November 1974 and at Orcas Island, Washington meeting, June 1975.] This would indicate a strongly peaked far field spectrum, as predicted by a relaxation model with a relatively low value for R_g . This result is in agreement with observations of the entire near field spectrum where peaked spectra were observed, but where the interpretation was somewhat uncertain.

(iv) A number of events ranging in magnitude from near $m_b = 3.0$ to $m_b = 5.0$ showed spectra with no discernible shift in corner frequency. If the events corresponded to failure zones of increasing length with increasing magnitude, it would be expected that the corner frequency would shift

noticeably to lower frequencies with increasing event magnitude and fault length. Alternatively, however, the increase in magnitude can be due to increased stress drop (or an increased ambient stress level) for failure zones of about the same dimension. As was previously described, the relaxation source models show that for fixed fault length and rupture velocity, the spectra would scale upward with no shift in corner frequency or significant change in spectral shape. This appears to be the most likely explanation of these observations, although it is possible that the rupture velocity increased with increasing fault length for larger events such that the ratio L/v_R remained nearly constant, so that the high frequency cut-off f_c^H was nearly the same for all the events. While the latter situation is certainly possible, it does not seem as probable as the former. If the rupture velocity did in fact change as described, the high frequency slope for $f > f_c^H$ should show a slope like f^{-1} to f^{-2} over an appreciable frequency range for the low rupture velocity events, and this does not appear to be the case. Thus it would appear that many of the events observed at the Near Field experiment site at Bear Valley, California correspond to earthquakes with quite variable stress drops (or events occurring in zones of highly variable stress concentration levels).

(v) While most of the spectral computations were made using the entire seismic record, so that both P and S wave spectra were included, a few were made from windowed time series, such that an attempt was made to isolate the P and S waves and compute their spectra individually. While this can be done with reasonable success in the far field at teleseismic distances, it can be shown theoretically that the P and S waves overlap

in time in the near field and because of the near field component of the radiation field, that no separation of compressional and shear type motion is really possible. Thus spectra obtained by "windowing" the time series in the near field are contaminated, especially at the low frequencies, due to truncation. However, at high frequencies it is reasonable to expect that the individual P and S wave spectra will be less contaminated by truncation and that reasonable estimates of P and S high frequency cut-off frequencies would be possible. The spectral data must be corrected for attenuation, and while the S wave corner frequencies are systematically lower than the corner frequencies for P waves, after correction for P and S wave attenuation there seems to be very little difference in the corner frequencies, although the P wave frequencies tend to be slightly higher. In terms of a relaxation source interpretation, the S wave corner frequency should, on the average (averaged over distance and azimuth), be somewhat less than the P wave corner frequency, although the theory predicts that at some individual points of observation the S corner frequency can be higher than the P corner frequency. Thus both theoretically and observationally, no very distinctive differences between P and S wave corner frequencies occur and indeed there is wide variation for individual point observations.

The near field results, as analyzed so far, suggest that at least some small earthquakes show spectral peaks in the far field spectrum. In terms of the relaxation source theory, this implies that these events occur in zones of high stress concentration of fairly small dimensions. The position of the apparent low frequency cut-off, f_c^L , is such that the inferred stress zone concentration would be of the order of 10-15 km. As a consequence, it would

also follow that the M_s value for such events would be anomalously low, due to the reduced low frequency amplitude at $f < f_c^L$, and that such events could appear more explosion-like in the m_b - M_s parameter space.

The high frequency, $f > f_c^H$, behavior of the spectrum for observed events implies a spectral slope of $1/f^3$ on the average, and hence a m_b cut-off in the m_b - M_s parameter space. Finally it appears that stress drops for events in the same region can be highly variable and that P and S corner frequencies are not much different on the average, with P wave corner frequencies being only slightly higher. (References: Current work in progress)

(b) Comparisons with Data from Other Earthquakes

Three separate studies have provided results bearing directly on the mechanics of earthquakes and the nature of the associated seismic radiation. These investigations involved the detailed study of the static near field of the San Fernando, Hedman Lake and Alaskan earthquakes; a study of the radiation fields from the Wilmington oil field earthquakes in terms of source properties; and finally a study of world-wide m_b - M_s data and the inference of properties of the tectonic stress field magnitude and spatial variations from this data. The latter study is still in progress.

The essential results of these studies are as follows:

(1) Application of tectonic modeling capability was made in the study of the San Fernando, Hedman Lake and Alaskan earthquakes, using two dimensional finite element modeling with the objective of delineating some of the conditions associated with and required for failure, as well as the effects of these tectonic processes.

The observations of static changes associated with the events, such as surface displacements, were used, along with knowledge of the medium properties, fault plane orientation and similar data, to determine conditions

and consequences of the earthquakes. In general good fits to the observations were obtained only when quite complex prestress, faulting and medium properties were used. Both dislocation and relaxation type modeling were used in the event studies. In particular, it was concluded that the initial stress field prior to the earthquakes was highly nonuniform, with very high stress concentrations over regions of characteristic dimension small, compared with the final fault volume, being typical of the events studied. The results for the San Fernando earthquake in particular indicated that a prestress of the order of 1 kbar was present in the focal region prior to the event. The characteristic dimension for this stress concentration was of the order of 2 to 3 kilometers, with the initial nonhydrostatic stress falling to considerably lower values (300-400 bars) outside this region. The initiation of failure occurred within this stress concentration zone, and the failure zone propagated to the surface, with curvature in the fault "plane" and secondary near surface faulting occurring. The latter effects appear to be controlled by a combination of the prestress spatial variability and changing material properties with depth. Both the displacement changes and stress changes on the failure surface were also found to be highly variable spatially. Similar results were obtained for the Alaskan and Hedman Lake earthquakes. It was found that the effects of gravity were particularly important for earthquakes involving considerable vertical motion and that estimates, by seismic methods, of energy and stress changes for such events would be considerably influenced by gravity coupling effects. As a general conclusion we find that the results of studies of these representative events show that shallow earthquakes are quite complex and commonly involve multiple fractures and highly spatially variable prestress. In

addition, changes in the failure conditions and mode of failure appear to occur along the failure zone, with strong depth dependence a dominant feature for earthquakes. Further, these variations from uniformity manifest themselves as first order effects, so that observations of, for example, static surface displacement and strain changes can only be explained by taking account of such variability. Interpretations of observations based on uniform or "average" changes in stress and displacement along the failure plane, for example, are likely to be grossly in error. This applies to both the static and dynamic characteristics of earthquakes. Relative to the stress levels required to initiate failure, we conclude that a higher stress than was previously supposed is required for failure at depths greater than 10 km and by implication also at shallower depths. In particular, in some cases at least, shear stresses of the order of 1 kbar appear to be required for failure initiation at depths near 10 km, and shear stresses of the order of at least several hundred bars at shallower depths.

(2) A comprehensive modeling study of the Wilmington oil field pumping operations, which resulted in subsidence and a number of small earthquakes, was carried out using relaxation source theory in modeling the earthquakes and the linear theory of fluid-solid composites to model the fluid extraction and subsidence.

Use of the observed seismic radiation from the earthquake in the source theory led to estimates of the nonhydrostatic (shear) strain field prior to failure, of 1.25×10^{-3} , and rupture velocities of 0.15 km/sec for two of the best recorded earthquakes. These events were representative of the group of earthquakes that occurred during the pumping operations. These events are particularly important since the

extent and sense of failure was known and measured from the offsets in well casings, in wells that entirely covered the region of failure, so that the number of unknown event variables was minimal. It was concluded that these events could be most appropriately termed subsidence earthquakes, in that they corresponded to localized nonlinear readjustment of the solid medium to the extraction of fluid and associated down-warp. In general, throughout the time history of the pumping, the overall response to the extraction of fluid from the field appeared to be linear, or nearly so, and the incidence of nonlinear phenomena, that is earthquakes, was isolated in both time and space and could properly be considered as second order perturbations to the overall response of the medium. This conclusion is enforced, and in part a consequence of the close fit achieved between the observed subsidence and that calculated from the (linear) modeling of the oil field for 32 years of fluid extraction. Further, the shear stress levels at the depths of the earthquakes predicted by the linear modeling of the fluid-solid composite are of the same order as those determined from the source theory interpretations of the seismic radiation from the earthquakes; namely between 100 and 125 bars at 0.5 km depth. Thus these independent theoretical predictions yield consistent results for the shear stress (or strain) levels within the medium, at these depths at least.

(3) The predicted $m_b - M_s$ values for theoretical earthquakes can be used to provide an interpretive basis for the estimation of stress drop (or ambient stress under certain assumptions) for observed earthquakes. Specifically, the locus of theoretical $m_b - M_s$ values for earthquakes of increasing rupture dimension and constant stress, rupture velocity and

stress concentration factor defines a single curve in the m_b - M_s plane. The same set of theoretical events with a different prestress level (and stress drop) defines a second parallel curve in this magnitude plane. For a range of prestress values, then, a network or grid of m_b - M_s curves is generated.

This system of theoretical event loci can be used to determine the prestress (or "stress drop") for the observed m_b - M_s data from earthquakes by simply plotting the data on the theoretical grid in the m_b - M_s plane and reading off the stress. This, of course, assumes that all the events compared to the theoretical event loci are of the same type and essentially are characterized by the same set of failure parameters (eg. rupture velocity). For this reason the observed world-wide set of m_b - M_s data are divided into the 50 seismic regions and then further subdivided into events occurring within particular depth regions. These subsets are then compared to the theoretical results for events of the proper type (thrust events) for the seismic region and for events occurring at the proper depth.

For the events so far considered in this framework, the rupture velocity has been taken to be near the shear velocity ($V_R = 0.9 V_S$) and the stress concentration factor large enough not to affect the M_s measurement. (Future work will involve other values for these parameters to assess the frequency of occurrence of earthquakes with low values of both V_R and R_S . However, even though high values of R_S and V_R have been employed up to now, it is still possible to infer the presence of low R_S events, for example, from the nature of the fit, or lack of a fit, of the theoretical curves to the data.)

Magnitude data for shallow earthquakes with depths less than 50 km for the period 1968-1974, subdivided by seismic region, were used to

estimate lithospheric stress levels in the manner described. Of the order of 2000 shallow events were used. On a world-side basis, over 90% of all the events observed were within the 0.01 kb (10 bar) to 1 kb prestress range, with the average being about 0.1 kb (100 bars). A few events, from only a few seismic regions such as the Aleutian arc and Japan regions, appeared to involve failure at very high stress levels, of the order of 1.5 kb. Finally, a few events, again from only a few seismic regions, had apparent prestress levels, or perhaps more properly, in this instance at least, stress drops, that were less than 10 bars. These latter events could be earthquakes with very low rupture velocities, or the M_s values could be inflated due to a measurement of an airy phase at a period shorter than 20 seconds.

For some seismic regions $m_b - M_s$ values were available down to m_b magnitudes near 4.0. In the range from $m_b = 5.0$ to $m_b = 4.0$, a few reported $m_b - M_s$ values were such that they implied small stress concentration factors, R_s . It would be expected that only a few such events would be reported even if many occurred, since only events with reasonably large, measurable, M_s values are included, those with small surface wave excitation near 20 seconds period having M_s values too small to be measured reliably in the noise background.

The next step in this analysis is to plot the stress values obtained for the events at the event hypocenters. Spatial contours of stress levels for events within particular depth ranges should show a systematic variation of stress that is correlated with the lithospheric plate structure. In this manner the inhomogeneity of the nonhydrostatic shear stress field can be determined as well as its amplitude level and orientation, the latter from standard "fault plane solutions". This spatial

analysis of the stress field is currently being investigated.

These results, taken together, show that the source theory employed, namely a relaxation source theory, is compatible with all the observations. Further, there appears to be considerable evidence that earthquakes commonly occur in strongly inhomogeneous stress zones with stresses of the order of 1 kb, not uncommon, but constrained to rather small spatial zones of the order of 10 kilometers or less. Most events, however, appear to be the consequence of failure at stresses of the order of 100 bars, with the stress being quite uniform over a region of many tens of kilometers. The strong inhomogeneities in the inferred stress fields for several well-studied earthquakes imply low M_s values for some earthquakes, and this is further supported by some of the m_b - M_s observations. (References: Archambeau, 1975a; Archambeau, 1975b; Archambeau, 1974)

3. References to the Detailed Developments and Complete Results

- Archambeau, C. B. and J. B. Minster, 1975a, Elastodynamic Representation Theorems in Prestressed Elastic Media with Moving Boundaries, submitted to *Geophys. J. Roy. astr. Soc.*
- Archambeau, C. B. and J. B. Minster, 1975b, Energy Balance for Elastodynamic Relaxation Sources, submitted to *J. Geophys. Res.*
- Archambeau, C. B., 1975, Studies of Tectonic Processes Associated with Fluid Injection and Surface Loading, Final Report, ARPA-USGS Fluid Injection/Waste Disposal Research Program, Contract No. 14-08-0001-12716, February, 1975.
- Archambeau, C. B., D. C. Harkrider and D. V. Helmberger, 1974, Studies of Multiple Seismic Events, Final Report to U. S. Arms Control and Disarmament Agency, Contract ACDA/ST-220.
- Archambeau, C. B., 1974, Investigations of Tectonic Stress, Semi-Annual Technical Report, Contract F19628-74-C-0087, ARPA Order No. 1795, Report No. AFCRL-TR-74-0424.
- Cherry, J. T., 1973, Calculations of Near Field, Earthquake Ground Motion, Systems, Science and Software Annual Technical Report, SSS-R-73-1759, ARPA Report, June, 1973.
- Cherry, J. T., T. C. Bache, C. B. Archambeau and D. G. Harkrider, 1974, A Deterministic Approach to the Prediction of Telesismic Ground Motion from Nuclear Explosions, Systems, Science and Software Final Contract Report DNA 2231F.
- Minster, J. B., 1973, Elastodynamics of Failure in a Continuum, Thesis, California Institute of Technology.

- Minster, J. B. and C. B. Archambeau, 1975a, The Relationship of Dislocation, Stress Pulse and Relaxation Representations of Seismic Sources, submitted to *J. Geophys. Res.*
- Minster, J. B. and C. B. Archambeau, 1975b, Models of Elastodynamic Relaxation Sources, submitted to *Geophys. J. Roy. astr. Soc.*
- Savino, J. M. and C. B. Archambeau, 1975, Discrimination of Earthquakes from Single and Multiple Explosions Using Spectrally Defined Event Magnitudes, to be submitted to *J. Geophys. Res.*, abstract AGU, *EOS*, 56, 1148, 1974.

III. MULTIPLE AND SINGLE EXPLOSION DISCRIMINATION USING FREQUENCY DEPENDENT MAGNITUDES

1. DISCRIMINATION METHODS BASED ON $m_b - M_s$

In this part we show that normal $m_b - M_s$ discrimination of single explosions and earthquakes is predicted by the theory and results described in the AFCRL Semi-Annual Report (Archambeau, 1974). Reference to Parts I - III in this report refer to this earlier semi-annual report. Simultaneously we show that multiple explosions can be designed to evade this criteria of discrimination and also to complicate any simple radiation pattern discrimination approach to the extent that it becomes a "costly" approach to discrimination.

Next we consider some basic spectral characteristics of explosions and earthquakes and redesign the m_b and M_s measurements, using a narrow band filtering method, so that multiple explosions appear as explosions in terms of this new $m_b - M_s$ discrimination procedure. In addition to M_s measured from Rayleigh waves, we also consider M_s measured from Love waves (M_s^L) and show that $m_b - M_s^L$ criteria are considerably more discriminatory than the usual $m_b - M_s^R$ criteria.

(a) Multiple Explosions: Signal Properties, Radiation Patterns, $m_b - M_s$ Characteristics.

Multiple explosions can be used to simulate earthquakes, at least in the crude sense that $m_b - M_s$ measurements will be such as to yield a resulting point in the earthquake population defined in the

$m_b - M_s$ plane. In addition, while this might be granted almost a priori, it is important to note that surface wave radiation patterns and spectra for such events are quite complicated and reasonably earthquake-like as well.

As an example, Figure (1) illustrates the Rayleigh wave radiation pattern for three 100 kt. explosions. These patterns, particularly at high frequency are quite similar to surface wave patterns generated by earthquakes (quadrupole). The change in shape of the patterns at long periods is not typical of an earthquake, but it is only at very long periods that a distinction is possible. Indeed at long enough periods (near 60 sec) the pattern becomes circular and distinctive of an explosion. However, such long period waves are not easily measured at teleseismic distances from low energy sources and an elaborate 360° array is required. Furthermore, as shown in Figure (2), the spectral shapes are such as to suggest a source at considerable depth, by virtue of the spectral "holes" which are indicators of source depth. Again, therefore, the surface wave spectral forms are more earthquake-like than not. This, of course, is also reflected in the time domain signals shown at various azimuths from the source.

Figures (3) and (4) show the Rayleigh and Love wave patterns at 14 and 20 seconds for a dip slip earthquake , and these can be compared to the patterns in Figure 1 for the multiple explosion. It

RAYLEIGH WAVE RADIATION PATTERNS FOR A TRIPLET OF 100KT EXPLOSIONS.

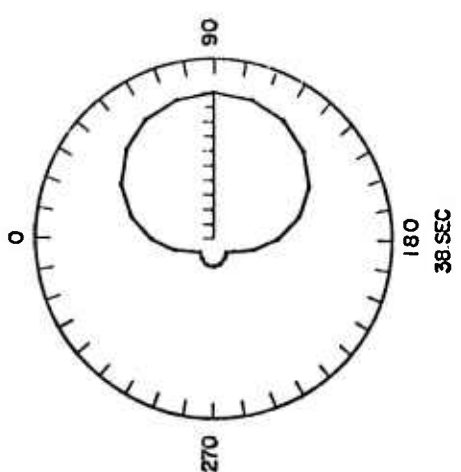
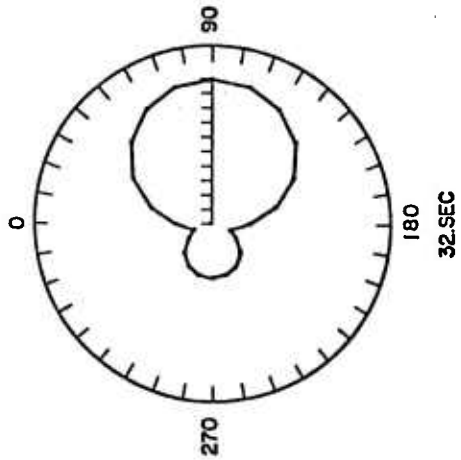
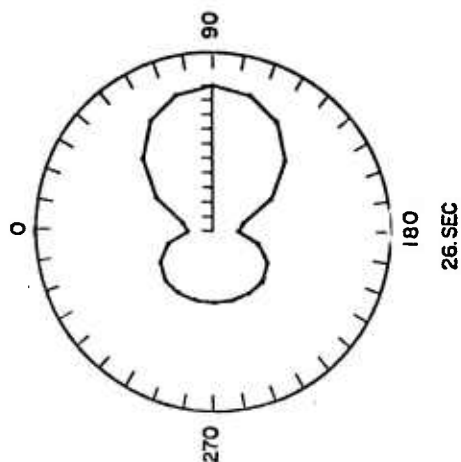
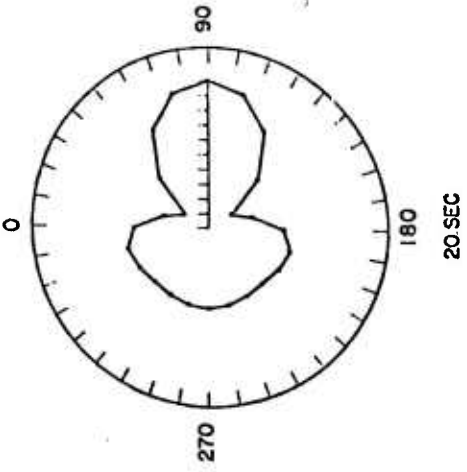
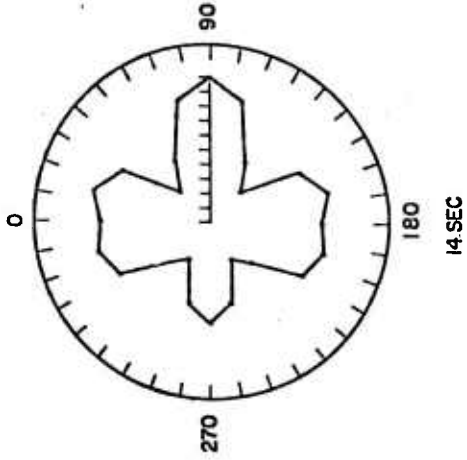
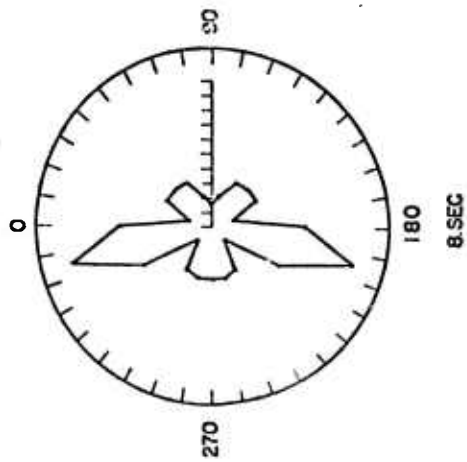


Figure 1. Theoretical Rayleigh wave radiation patterns for a multiple explosion of three 100 kt. events, 48 no prestress. Period range $8 \leq T \leq 38$ sec.

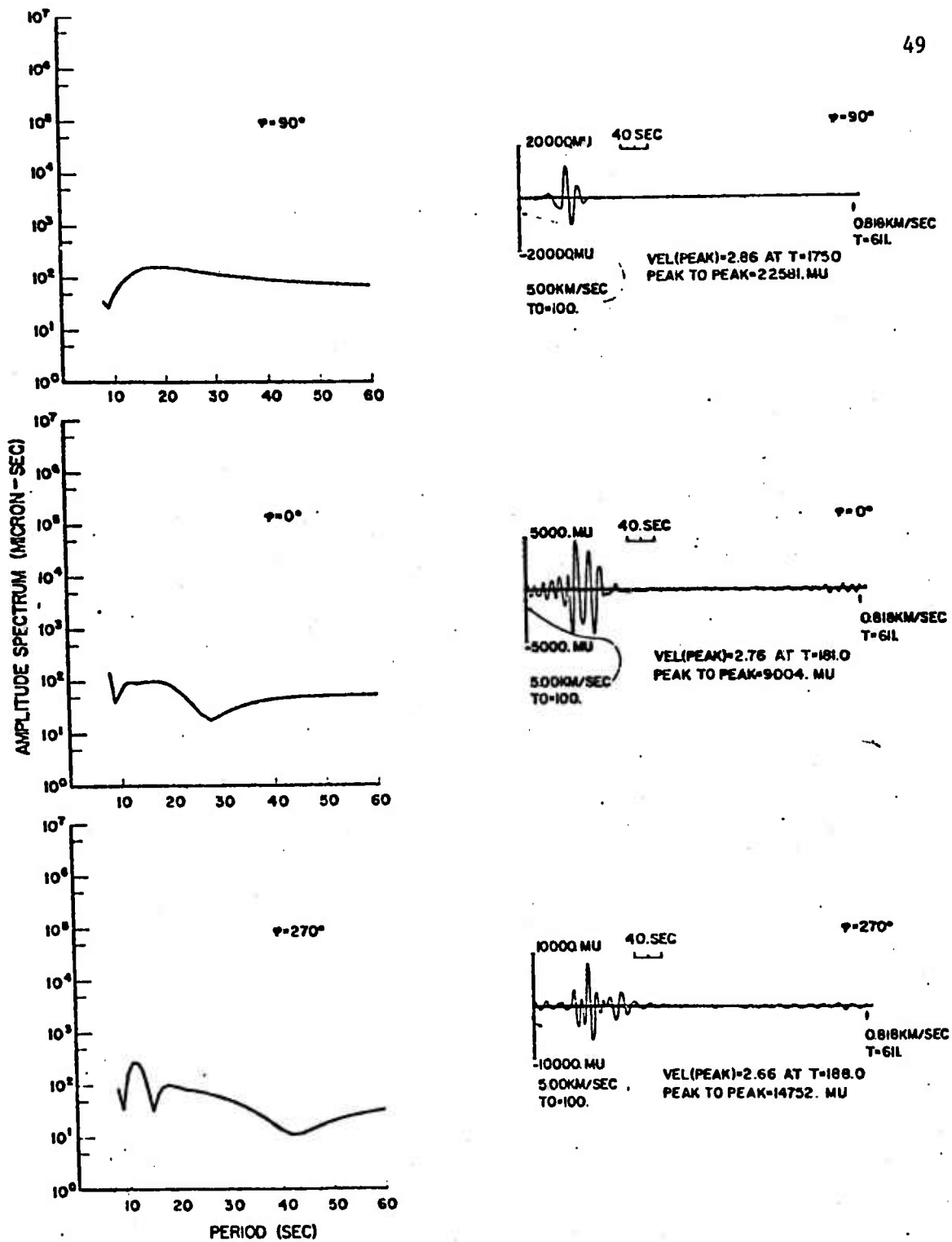


Figure 2. Theoretical Rayleigh wave spectra and time series at three azimuths for the multiple event of Figure 1.

is clear that the 20 sec pattern for the multiple explosion is very similar to a "dip slip" earthquake radiation pattern, but that the 14 sec explosion pattern is not. Further the earthquake pattern retains the two lobed shape to longer periods while the multiple explosion does not. However implementation of a viable network to detect such differences as well as a routine analysis procedure capable of generating spectral radiation patterns for a wide period range is not a particularly simple matter. Thus we conclude that while surface wave radiation patterns could be used, a simpler procedure is called for.

We therefore consider the $m_b - M_S$ criteria, in view of its empirical success for single explosion discrimination, and attempt to modify the $m_b - M_S$ measurement in order to cope with the multiple event. To do so we construct synthetic multiple explosions from the set of explosions previously considered in Part III.

Table 1 lists 4 multiple events that we will consider as typical. The table also indicated how these events are summed to yield the multiple events in each case. These multiple events are constructed in order to yield $m_b - M_S$ results that place them within the earthquake population and also such that the body and surface wave synthetic seismograms look like earthquake seismograms.

In particular Figure (5) shows the theoretical earthquake with $L = 2.4$ km, from Part I, along with multiple explosions designed to look similar to this event in terms of wave form as well as in terms

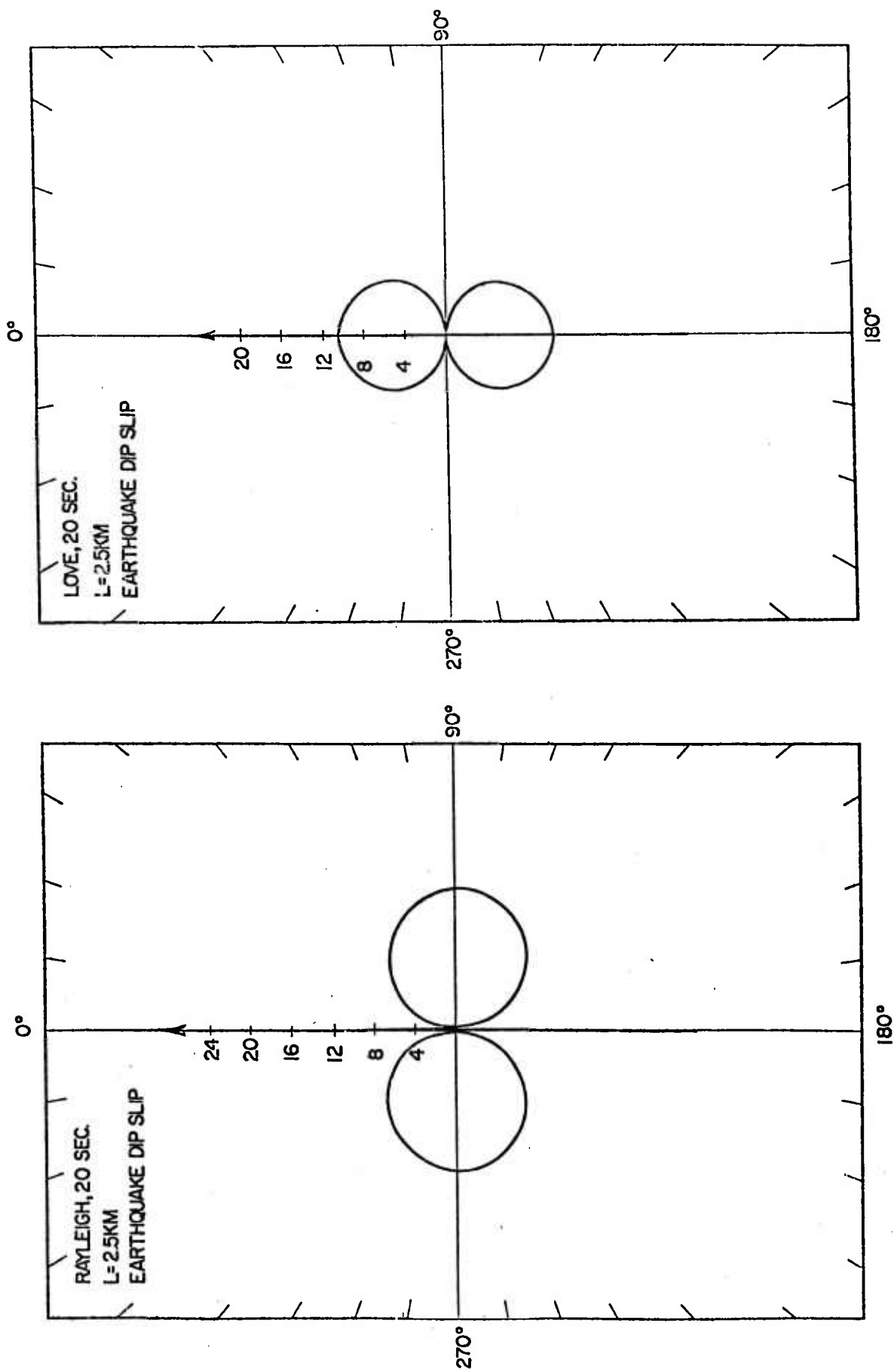


Figure 3. Theoretical Rayleigh and Love wave radiation patterns at 20 seconds period for a 2.5 km. fault length, dip slip earthquake, 500 bar stress drop. 51

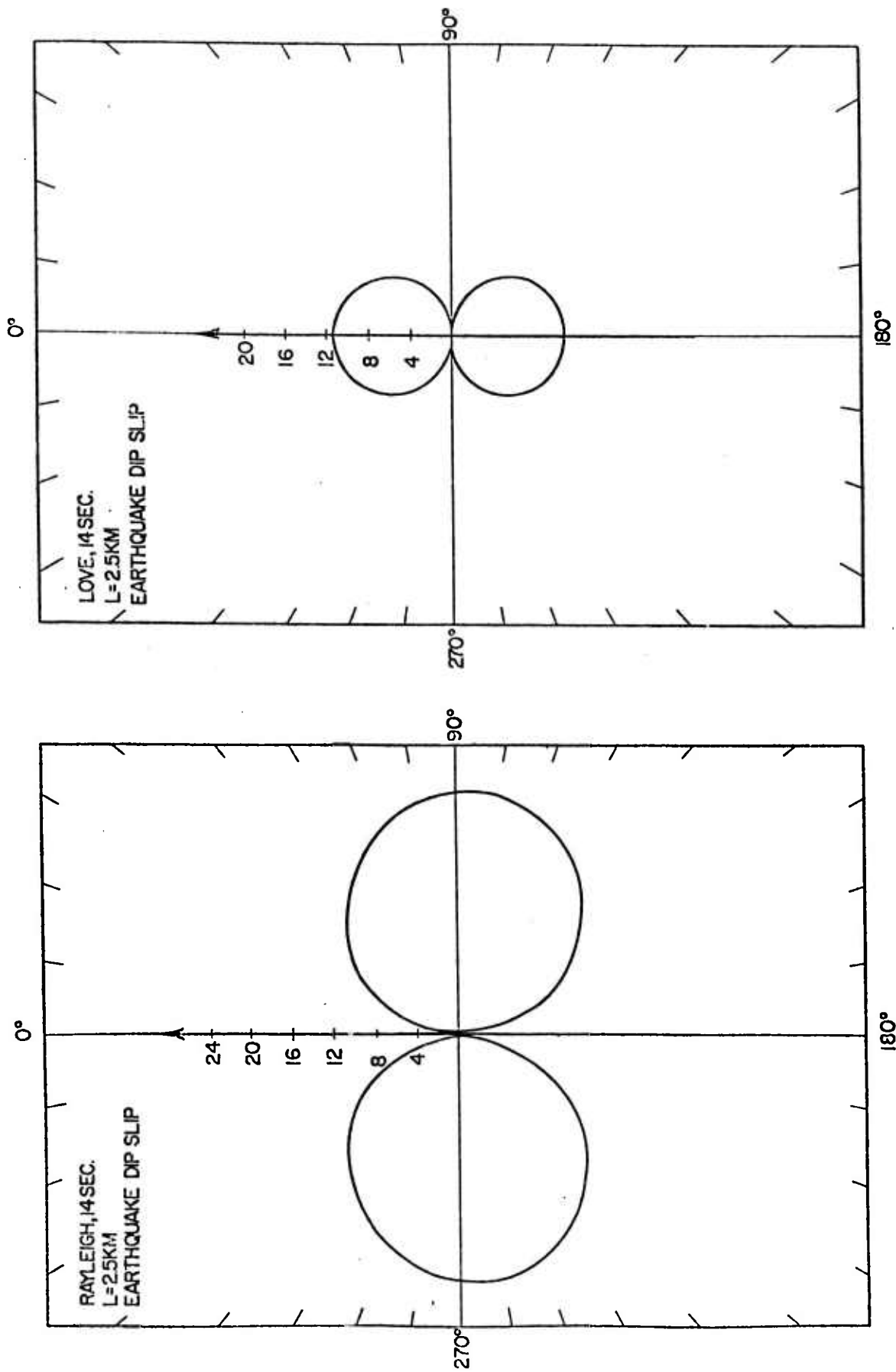


Figure 4. Theoretical Rayleigh and Love wave radiation patterns at 14 sec. period for the same earthquake as shown in Figure 3. The period is near the Airy phase maximum for both wave types.

of m_b and M_S values. In Figure (5) only the P wave train is shown, but the Rayleigh wave train has a very similar form for the earthquake and multiple events as well.

Figure (6) shows all the P wave trains for the multiple events considered. They clearly have the complexity of typical earthquakes. Figures (7) and (8) show the Love and Rayleigh waves generated by the multiple explosions assuming the medium to be granite (model G-2) and the prestress to be 500 bars. As noted, a lower prestress level of 165 bars and the granite model G-1 can be obtained by simple scaling. In the following parts of the analysis, the granite model G-1 is used with a prestress of 165 bars, 55 bars, or no prestress, depending on the conditions we regard as being appropriate to the discussion.

Using the previous results from Parts I and II along with standard m_b and M_S^R measurements of magnitudes from the synthetic multiple explosion signals shown in the preceding figures, we obtain $m_b - M_S^R$ results shown in Figure 9. Clearly the multiple explosions are within the earthquake population and would not be identified as explosions. It is quite clear that this occurs because the m_b value is measured from the signal of the smallest explosion while the M_S^R is measured from the sum of all the explosions. Thus the M_S^R is large for the m_b value computed.

Table 1 - Multiple Event Parameters

Event*	Yield	$D_s^{(k)}$ (km.)	δt_k (sec.)	k
1-5-20 kt multiple event	1 kt	0.0	0.0	1
	5 kt	2.0	2.0	2
	20 kt	8.0	8.0	3
5-20-100 kt multiple event	5 kt	0.0	0.0	1
	20 kt	5.0	4.0	2
	100 kt	10.0	8.0	3
20-100-1000 kt multiple event	20 kt	0.0	0.0	1
	100 kt	10.0	8.0	2
	1000 kt	20.0	16.0	3
5-20-100-100-100 kt multiple event	5 kt	0.0	0.0	1
	20 kt	5.0	4.0	2
	100 kt	10.0	8.0	3
	100 kt	15.0	12.0	4
	100 kt	20.0	16.0	5

*All multiple event summations were performed using the "local velocity" $v = 2.0$ km/sec. in the relation for the appropriate delay time Δt_k for the k th event of a multiple set, where:

$$\Delta t_k = \delta t_k - \frac{D_s^{(k)} \cos \varphi}{v}$$

See Table 2 for depths and other parameters appropriate to the individual explosions making up the multiple event sets.

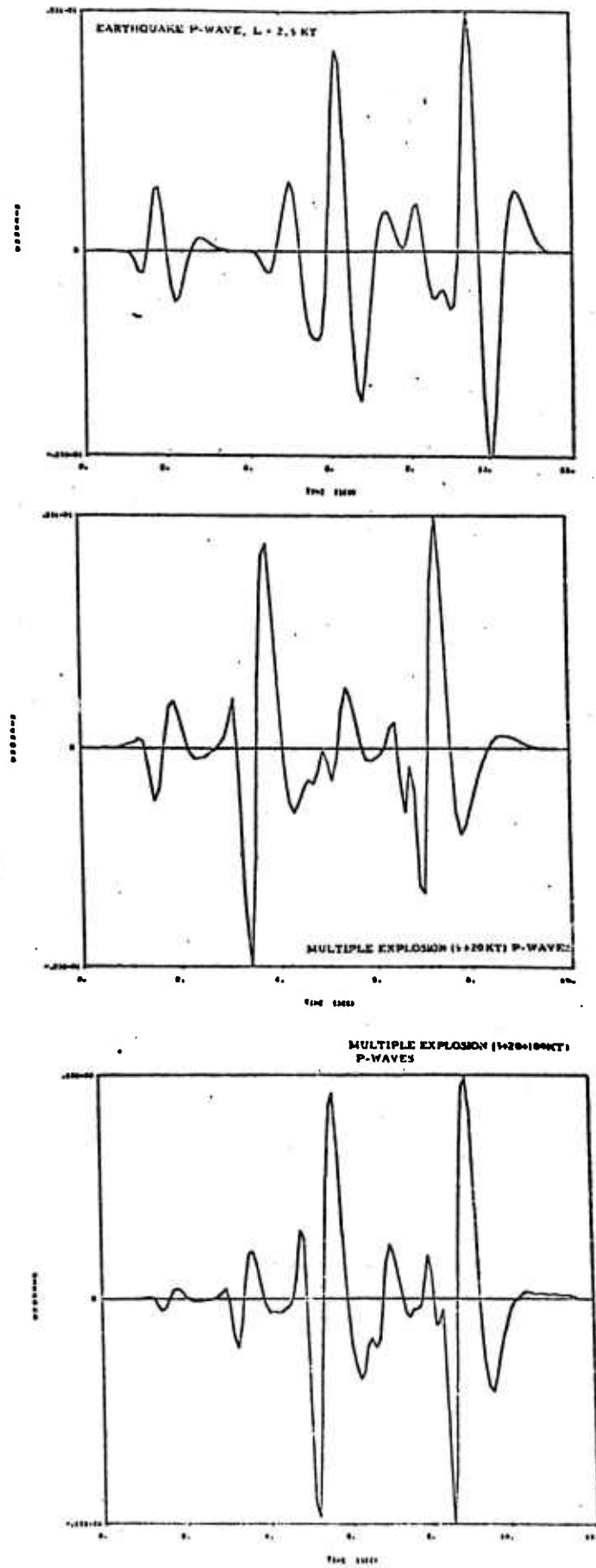


Figure 5. Comparison of time domain P wave signals from an earthquake and two multiple explosions, both with tectonic release, to yield a P wave signal similar to that from an earthquake as well as $m_b - M_s$ values appropriate to those for an earthquake. Distance 4000 km., azimuth 30°.

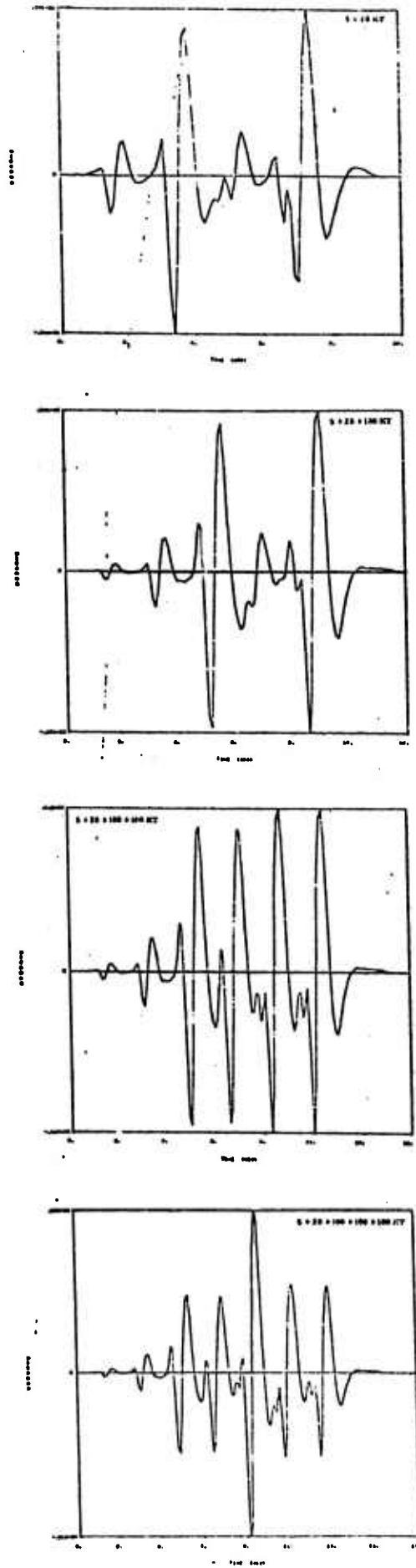


Figure 6. Compressional wave trains for five different multiple explosions involving various combinations of 5, 20 and 100 kt. explosions with tectonic release included. Source model G - 2 and CIT 109P with low Q or model C - 1 with CIT 109P and .5Q structure. Distance 4000 km., azimuth 30°.

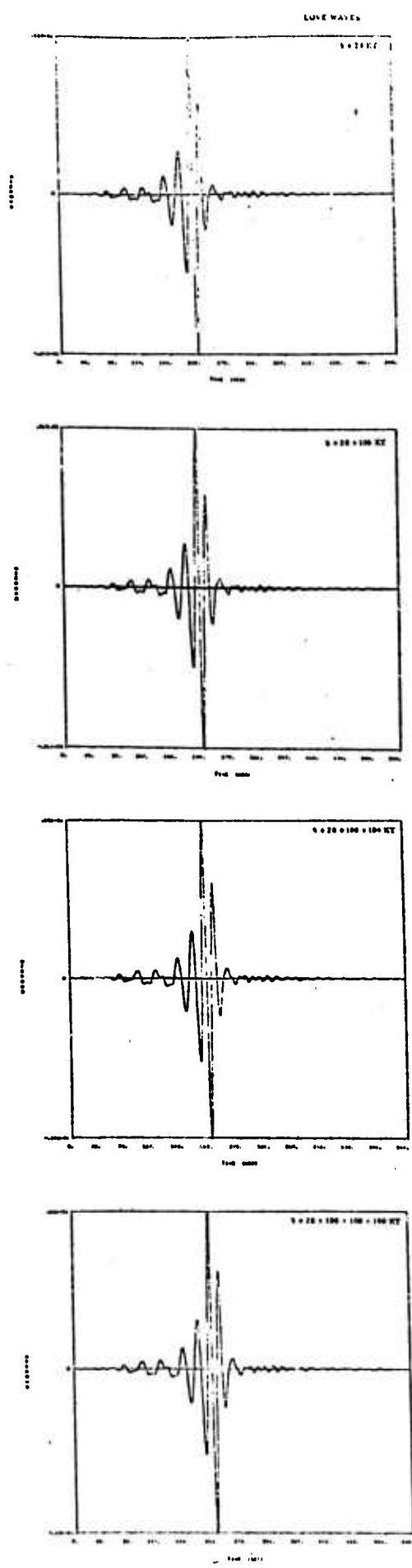


Figure 7. Love waves from the five different multiple explosions of Figure 6. Love waves arise from tectonic release due to the shatter zones created by the explosion shock waves. For prestress 165 bars and explosion model C-1 the amplitude scale is to be divided by a factor of 3 for true ground amplitude at 20 sec. period. All other periods are filtered by the LRSM long period seismometer, normalized to unity at 20 sec. period.

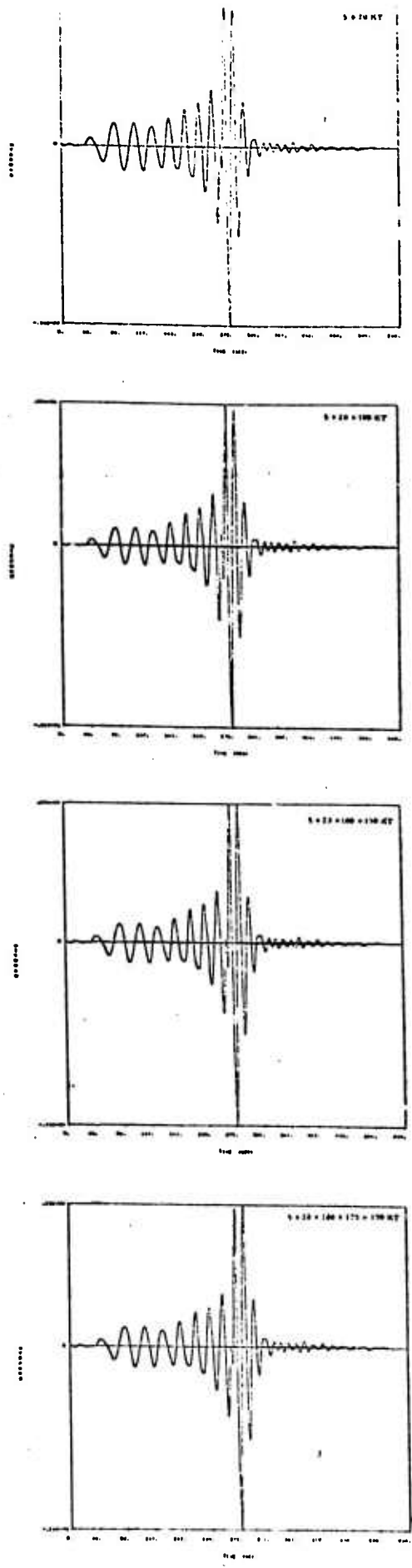


Figure 8. Rayleigh waves from the five different multiple explosions of Figures 6 and 7. Amplitude scaling for the source model G-1 with 165 bars prestress is the same as for the Love waves. Amplitudes as illustrated are appropriate to the model G-2 and 500 bars prestress. Distance 4000 km., azimuth 30°.

In this figure we also see, quite directly, that the theoretical predictions of Parts I and II yield results showing that single explosions and earthquakes will discriminate on the basis of separation of the populations in the $m_b - M_S$ plane down at least to magnitudes near $m_b = 3.5$. Discrimination based on population separation of about .7 magnitude units in M_S^R will continue to lower magnitudes provided the earthquakes do not naturally occur in concentrated prestress zones of quite small characteristic dimension (R_S). Even with quite high prestress (165 bars) the single explosions lie outside the earthquake population boundary line--in the region of lower M_S^R values for a given m_b .

We also see from Figure (10) that M_S^L , the surface wave magnitude measured from Love waves in exactly the same manner as is M_S^R , can be used along with the m_b measurement to define event populations wherein earthquakes are well separated from single explosions. Indeed the separation is considerably greater than it is for the $m_b - M_S^R$ criteria. However, again we see that for prestress values from 55 to 165 bars, that the multiple explosions are within the earthquake population and cannot be identified using this criteria.

In the next section we will examine the spectral basis for single explosion-earthquake discrimination using $m_b - M_S$, and then apply a spectral measure of m_b and M_S , which we will denote as

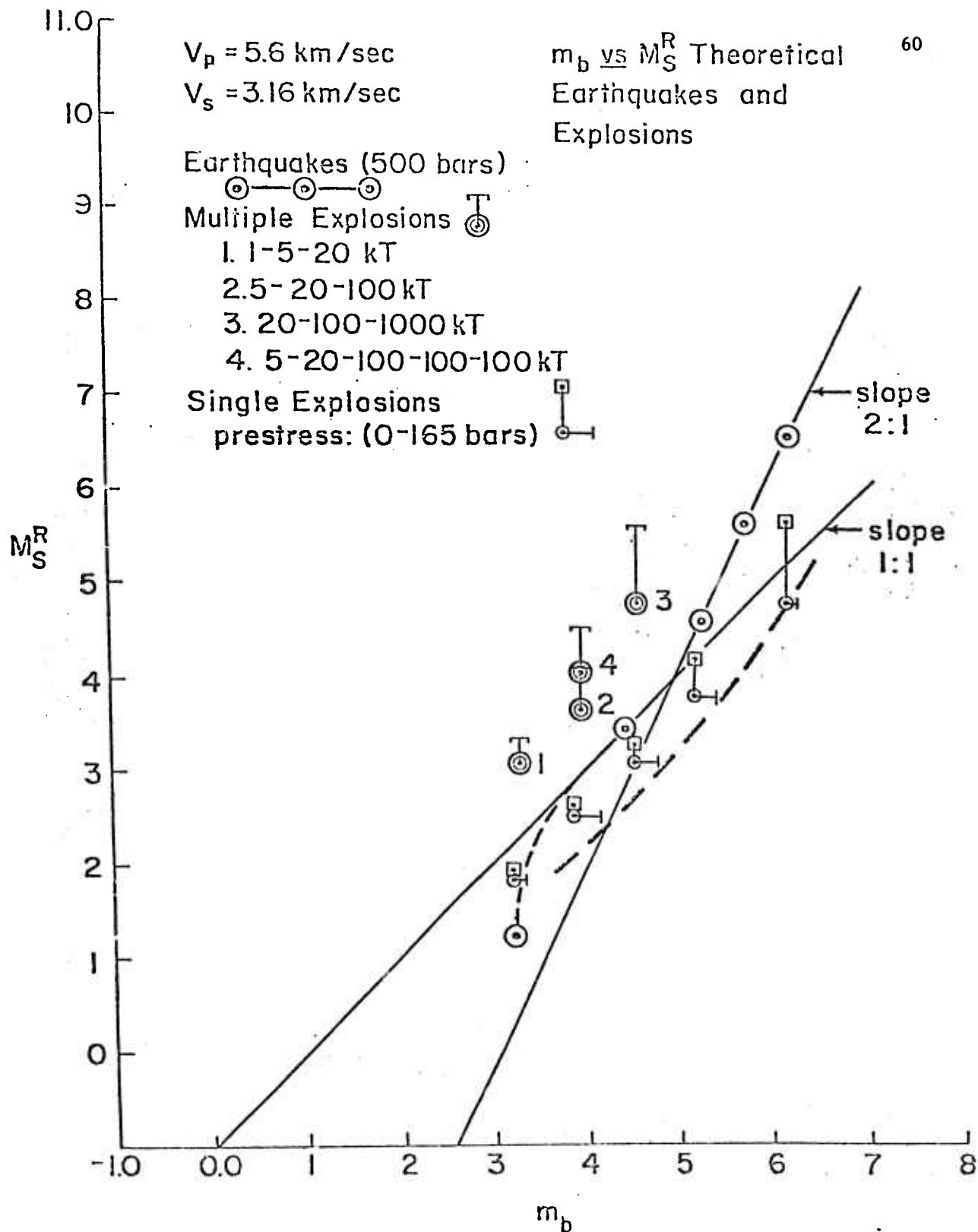


Figure 9. Rayleigh surface wave magnitude as a function of body wave magnitude for single and multiple explosions. The most extreme bound of the earthquake population, modeled by dip slip, 500 bar stress drop, high rupture velocity earthquakes, is also shown for comparison. All other earthquakes lie to the left of this locus of (Continued on following page)

Figure 9 (Continued).

"explosion-like" earthquakes. All the multiple explosions lie within the earthquake population and hence would not be identified as explosions using the standard m_b - M_s criteria. The vertical lines on all the theoretical explosions show the range of increase in M_s^R for prestress increasing from zero (circles) to 165 bars (squares or horizontal bars). The horizontal bars on the single explosions denote the range of m_b that is possible, ordinarily the largest m_b indicated is used. All explosions are for the model G-1; and all events are calculated using the CIT 109P - .5Q earth model. All calculations for a distance of 4000 km. and an azimuth of 30° .

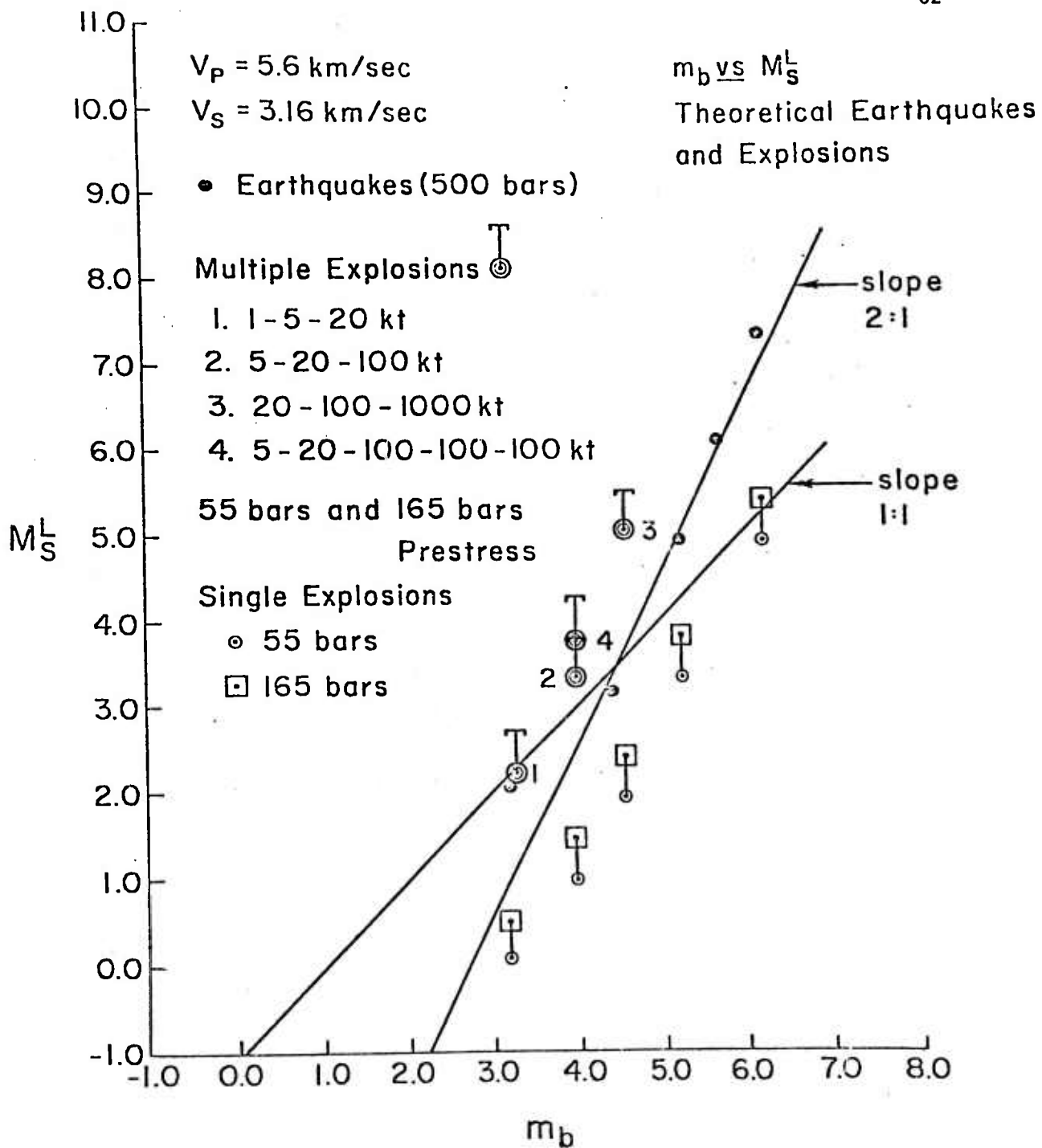


Figure 10. Love surface wave magnitude as a function of body wave magnitude for single and multiple explosions. The range of surface wave magnitude of the explosions for prestress ranging from 55 to 165 bars is indicated by the vertical bars on the points. High stress drop, high stress concentration, high rupture velocity, dip slip earthquakes are shown to indicate the limits of the earthquake population, with all other earthquakes being to the left and above the earthquake locus shown. All the multiple explosions considered therefore lie within the earthquake population.

\bar{m}_b and \bar{M}_S spectral magnitudes, which will allow us to identify multiple explosions in most cases.

(b.) Spectral Basis for $\bar{m}_b - \bar{M}_S$ Discrimination

The spectral basis for single event $m_b - M_S^R$ discrimination is summarized in Figures (11) and (12). From the description afforded in these schematic representations we see that there are two main reasons why the $m_b - M_S$ values for explosions are different than those for earthquakes. They are:

- (1.) The spectra defining the magnitude measurements for explosions in the yield range of interest are such that both magnitude measurements are made in the low frequency range, while for earthquakes the m_b measurement is almost always (except for small events) made in the high frequency range of the event spectrum (i. e. at a frequency larger than the peak or corner frequency, f_c^H , for the event) while the M_S measurement is usually made in the low frequency range of the event spectrum (except for extremely large events). Because the earthquake spectra fall off as f^{-3} for $f > f_c$, they are poor in high frequency content relative to an explosion of the same low frequency level. That is, for an explosion

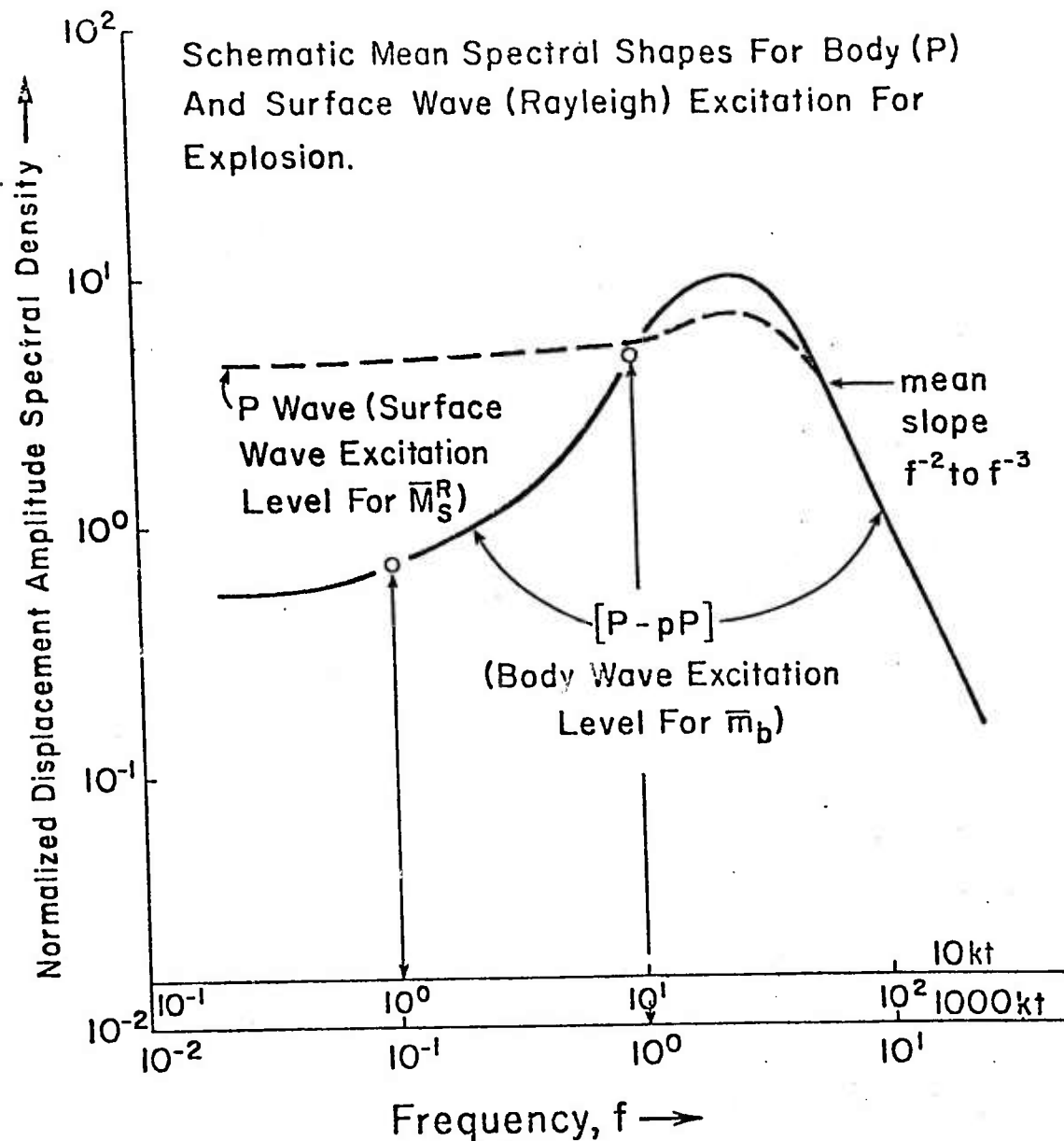


Figure 11. Spectral characteristics of explosions for yields in the range 10-1000 kt. The source P wave spectrum is nearly flat at long period. The interference of P and pP gives the observed body wave spectrum a strongly peaked character with strong cancellation of long period energy. The body wave magnitude is modified by the P-pP interference while the surface wave magnitude is determined by the true, flat, P wave spectrum of the explosion. For all explosions with yields less than approximately 1000 kt, the peak or corner frequency is at a frequency greater than 1 Hz, hence all m_b (and M_s) values are determined by source spectral characteristics in the "low frequency range" as indicated.

Schematic Mean Spectral Shapes For Body (P)
And Surface Wave (Rayleigh) Excitation For
Earthquakes

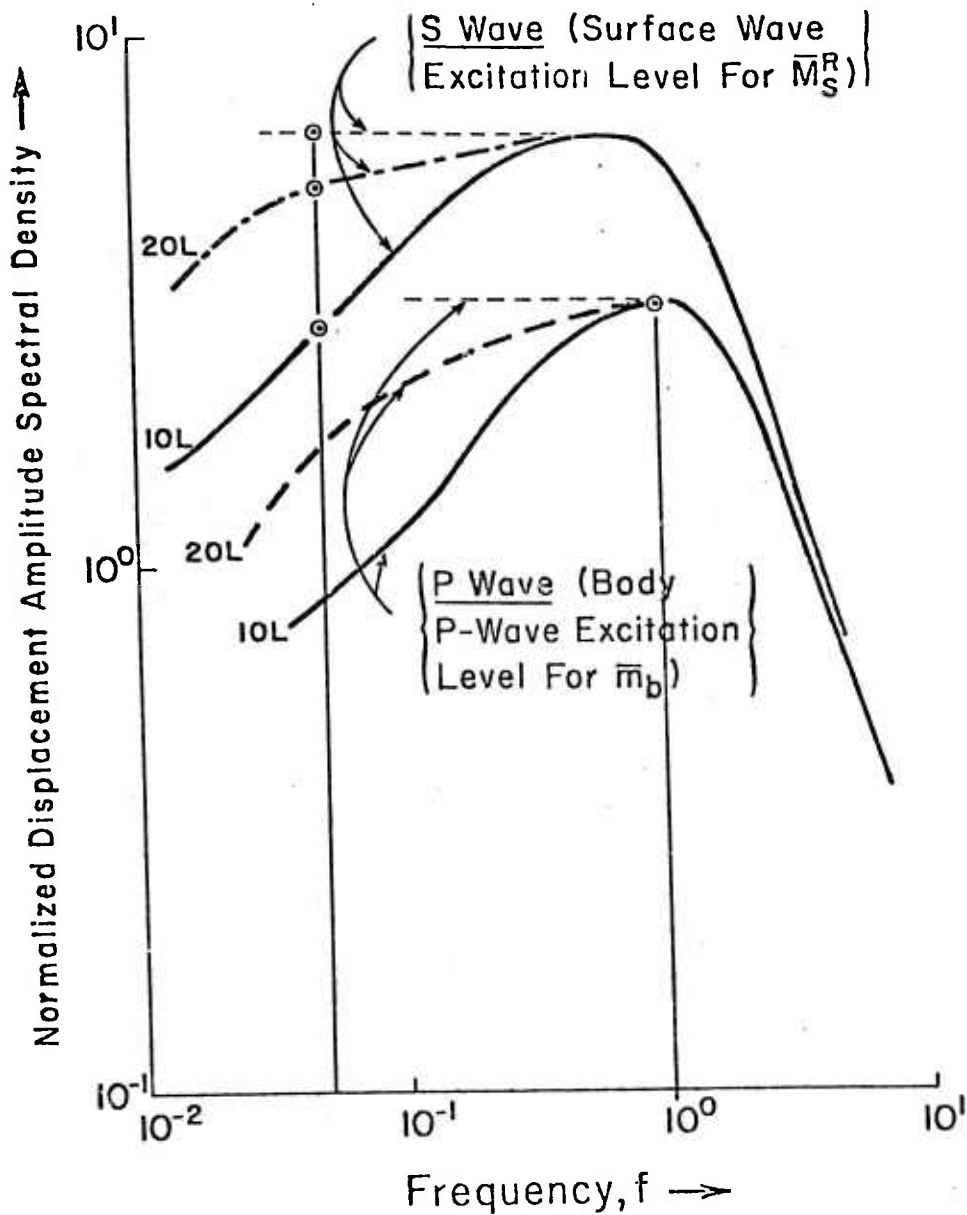


Figure 12. Spectral characteristics of an earthquake with fault dimension of the order of 2.5 km. ($m_b \approx 4.5$, if stress drop is about 500 bars). For larger L events, the frequency scale should be shifted to the right (spectra peaks at lower frequency), for events of smaller dimensions the scale must be shifted to the left. Various spectral shapes are indicated, involving more or less long period excitation, depending on the characteristic dimension of the prestress zone. R_s values of 10L, 20L and infinity

(Continued on following page)

Figure 12 (Continued).

are indicated, with L the fault length. The surface wave magnitude at .05 Hz is essentially determined by the large S wave field from the source, while the body wave magnitude is determined by the 1 Hz level from the P wave field as indicated. Only for high stress, high rupture velocity earthquakes with fault lengths of less than 2.5 km ($m_b < 4.5$) is the "low frequency range" of the earthquake spectrum used for both m_b and M_s determinations.

and an earthquake with the same low frequency level, from which M_S is determined, the explosion will have a significantly higher m_b , since this magnitude is also determined by the low or intermediate frequency spectral level, while the earthquake m_b is determined from the high frequency range of the P wave spectrum of the event, which will be considerably lower than the low frequency level used for the M_S determination due to the high frequency roll-off.

- (2.) The fact that P waves from explosions are rich in high frequency relative to earthquakes with the same low frequency spectral level provides only one aspect, or part, of the $m_b - M_S$ based discrimination. The other spectral difference which accounts for the $m_b - M_S$ difference between explosions and earthquakes is the very large generation of S waves by earthquakes compared to the P wave generation. In general, as indicated in Figure (12), the S wave amplitude is of the order of 5 times greater than the P wave amplitude, and it is the quadrupole S wave that essentially determines the Rayleigh (and Love) surface wave amplitude excitation. Since it is the low frequency level of the large S wave that determines the

M_S , then for an explosion to have a comparable M_S , its P wave low frequency spectral level must be about the same as the S wave low frequency level of the earthquake. Now the m_b for the explosion will be measured from a P wave spectrum with a low frequency spectral level comparable to the S wave spectral level for the earthquake, or at a level 3 to 5 times higher than the P wave spectral level of the earthquake. Hence the m_b for the explosion will be higher than that for the earthquake for this reason, in addition to the fact, noted in (1.) above, that it will also be higher because the m_b for the earthquake will be reduced by the high frequency spectral roll-off.

This spectral explanation is a first order analysis of the reasons for the explosion-earthquake $m_b - M_S$ differences. Spectral peaking, if present, and due to extreme prestress concentration, will modify the earthquake population distribution and the separation of populations may not, necessarily, be maintained at low magnitudes. This has of course been seen in the $m_b - M_S$ predictions previously shown, and has been discussed.

However, we see that time domain $m_b - M_S$ measurement differences for explosions and earthquakes have a rational explanation in terms of spectral differences between the two kinds of sources.

The spectral differences can of course be traced back to basic physical causes, via the discussions of parts I and II.

In view of this understanding of $m_b - M_S$ data in spectral terms, it is useful to consider a spectral definition of m_b and M_S . In particular, we can precisely define a spectral body wave magnitude \bar{m}_b as the log of the amplitude of the output of a very narrow band filter (high Q filter), centered at 1 Hz, plus a distance correction factor \bar{b} . In correspondence with the usual m_b definition, we in fact define \bar{m}_b by

$$\bar{m}_b = \log_{10} (A_g / T_g) + \bar{b}$$

where $T_g = 1$ sec here, and A_g denotes the amplitude of a narrow band, phaseless, filter output with center period at $T_g = 1$ sec, and \bar{b} is the distance correction factor. The input to the filter is the entire P wave train for the event. A description of the type of filter to be used is given by Archaubeau and Flinn (1965).

Similarly, we can very precisely define spectral surface wave magnitudes \bar{M}_S^R and \bar{M}_S^L by

$$\left. \begin{aligned} \bar{M}_S^R &= \log (A_g / T_g) + \bar{B}_R \\ \bar{M}_S^L &= \log (A_g / T_g) + \bar{B}_L \end{aligned} \right\}$$

where A_g is the output of the narrow band filter at $T_g = 20$ sec with either the Rayleigh wave (vertical or horizontal component) as input

or the Love wave as input, while \bar{B}_R and \bar{B}_L are the appropriate surface wave distance correction factors.

The advantages of defining spectral magnitudes, rather than time domain measured magnitudes, are that the definitions are not vague and so leave no room for measurement variations among different events and among different observers at different points of observation. This should reduce the scatter in magnitude data, to scatter that can be traced to physical causes. In addition, based on our previous discussion in this section, the $\bar{m}_b - \bar{M}_S^R$ and $\bar{m}_b - \bar{M}_S^L$ data should provide nearly the same kind of event discrimination for single explosions and earthquakes as did the "old" $m_b - M_S$ criteria, obtained in the time domain.

However, most important of all, the spectral magnitude definition, when applied to multiple explosions, should give $\bar{m}_b - \bar{M}_S^R$ and $\bar{m}_b - \bar{M}_S^L$ results diagnostic of an explosion. The reason that this should be the case is not hard to see. In particular we saw that the reason the regular $m_b - M_S$ criteria failed was because the m_b was obtained in the time domain from the earliest (and smallest) explosion while the M_S was measured from the superposed Rayleigh (or Love) surface waves from all the events. We saw that it was, in fact, not difficult to arrange the explosion event origin times and spatial separations so that the individual P wave signals would be well separated in time, yet delayed so as to look like a complex earthquake signal while the

surface waves from each explosion being of long period, completely overlapped in time and summed. Now if we would similarly sum the body wave amplitudes from the individual explosions we would increase the body wave magnitude in a manner comparable to the summation of surface wave amplitudes and the relation of the m_b to the M_S would be appropriate to an explosion and equal to the sum of the individual explosion yields. The process of narrow band filtering of the P wave train will do very nearly that, so that A_g appearing in the definition for \overline{m}_b will be close to the sum of the amplitudes of all the individual event amplitudes at 1 Hz.

In more detail, the filter used is phaseless, so that with a finite Q (that is a finite band width) the filter output will peak at a time when the 1Hz energy arrives. This is just the group time, t_g , for the 1Hz energy (hence the use of the subscript g on A_g and T_g in the previous definitions). For a series of signals, all containing 1 Hz energy, the filter output will oscillate at essentially 1 Hz, but with an envelope corresponding to the smooth curve through the peaks of the oscillations, that peaks at times of 1 Hz energy arrival from each of the individual signals. However, since the filter has a high Q , the output will continue to "ring" after each signal pulse and so an earlier signal pulse will contribute a 1 Hz amplitude "ring" to later pulses and there results an addition of 1 Hz amplitudes. Since the filter is made to be phaseless by filtering the signal series in both the forward and

backward time sense, then every signal rings into, and adds to, every other signal, wherever they may be located in time. Now if one of the signals contains more 1 Hz energy than the others, then the filter output envelop will have the largest peak value at the time of this large signal arrival. The actual filter output amplitude at this time will be proportional to the 1 Hz amplitude of the large signal, plus varying contributions from other signals arriving before and after this particular signal (for details - that is the exact amplitude relations - see Archambeau and Flinn, 1965). Therefore, we see that for a complex series of signals, in particular for a multiple explosion, we wish to pick from among all the filter output envelope maxima, that one that is the largest, since it most accurately measures the 1 Hz amplitude in the wave train. At worst it gives the amplitude of the largest 1 Hz signal of the series and, as well, the time of its arrival, the group time.

Hence A_g is defined, in the case of many signal wave trains, as the largest envelope maxima of the filter output.

In the following section we shall complete the \bar{m}_b and \bar{M}_S definitions by defining the distance correction factors. When these definitions have been given we can apply the procedure to the theoretical events of the previous sections to test the validity of the method as a discrimination method.

(c) Definition of \bar{m}_b and \bar{M}_S and application to explosion - earthquake discrimination.

The definitions given for \bar{m}_b , \bar{M}_S^R and \bar{M}_S^L are incomplete until the distance factors \bar{b} , \bar{B}_R and \bar{B}_L are defined. It is appropriate, however, to define these distance correction factors so as to give spectral magnitudes that are nearly distance independent - that is these factors should be essentially the same, outside of a constant perhaps, as are the distance correction factors for the regular time domain magnitudes, m_b and M_S . Hence we will require that

$$\left. \begin{aligned} \bar{b}(\Delta) &= b(\Delta) + c_1 \\ \bar{B}_R(\Delta) &= B_R(\Delta) + c_2 \\ \bar{B}_L(\Delta) &= B_L(\Delta) = c_3 \end{aligned} \right\}$$

where the c_k , $k = 1, 2, 3$ are required to be constants. To determine these constants we will require that the spectral magnitudes closely match (in a least squares sense) the time domain magnitudes for a wide range of event sizes. With this requirement, we can select any particular distance Δ to evaluate the constants c_k through use of relations above.

Thus, if we compute the factors $\log A_g/T_g$ and $\log A_1/T_1$, where A_1 and T_1 refer to the time domain amplitude and effective period for the first cycle of motion recorded for a number of synthetic earthquake and explosion P wave signals and A_g^* is the maximum of the filter output at 1 Hz, and further require that the \bar{b} be such that

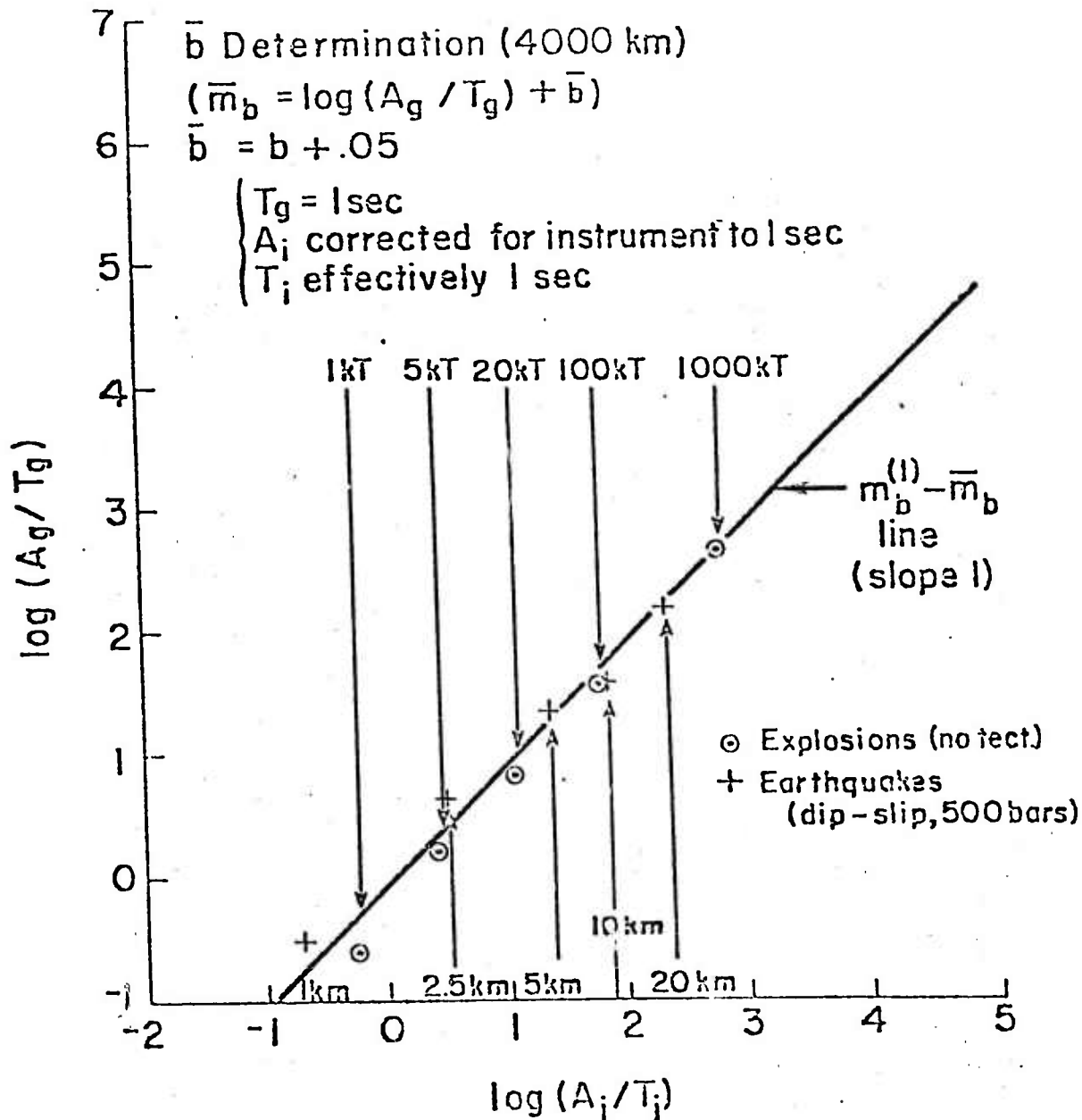


Figure 13. Plot of log of the narrow band filter amplitude maximum A_g , normalized by the center period of the filter, T_g , versus the log of the time domain seismogram P wave amplitude, A_i , normalized by the effective period T_i . Here the A_i/T_i ratio is used in the normal m_b calculation, while A_g/T_g is used for the "spectral body wave magnitude", \bar{m}_b , in which $T_g = 1$ sec. The plot determines the constant factor of proportionality between $m_b^{(l)}$ and \bar{m}_b . They are essentially identical over most of the range of events, but for small events \bar{m}_b will be slightly higher for earthquakes than for explosions.

\bar{m}_b be essentially the same as $m_b^{(1)}$ for the events at some distance, say 4000 km, then we get the results shown in Figure 13. Since \bar{b} is tied to b , via the previous relations, we are assured that this correspondence between \bar{m}_b and $m_b^{(1)}$ will hold at all distances.

We find that

$$\bar{b} = b + .05$$

where the fit over the range of magnitudes and events of Figure 67 is in a least squares sense. However we note that there is a slight systematic difference between the fit to earthquakes as compared to the fit to explosions.

Figure 14 and 15 show the results of applying the same procedure to the 20 second surface wave magnitudes. We find

$$\bar{B}_R = B_R - 1.43$$

$$\bar{B}_L = B_L - 1.43$$

These results now completely define the spectral magnitudes.

It is worth pointing out again that the \bar{m}_b is very close to the time domain magnitude $m_b^{(1)}$, by construction. Thus since $m_b^{(1)}$ is almost always somewhat lower than $m_b^{(2)}$ and/or $m_b^{(3)}$, and since the usual m_b value given for an observed event is the largest of the $m_b^{(i)}$, then it follows that the \bar{m}_b defined will usually be smaller than the observed m_b by around .3 magnitude units. The reason $m_b^{(1)}$ was used to fix our \bar{m}_b value is because it is the least contaminated by pP, sP

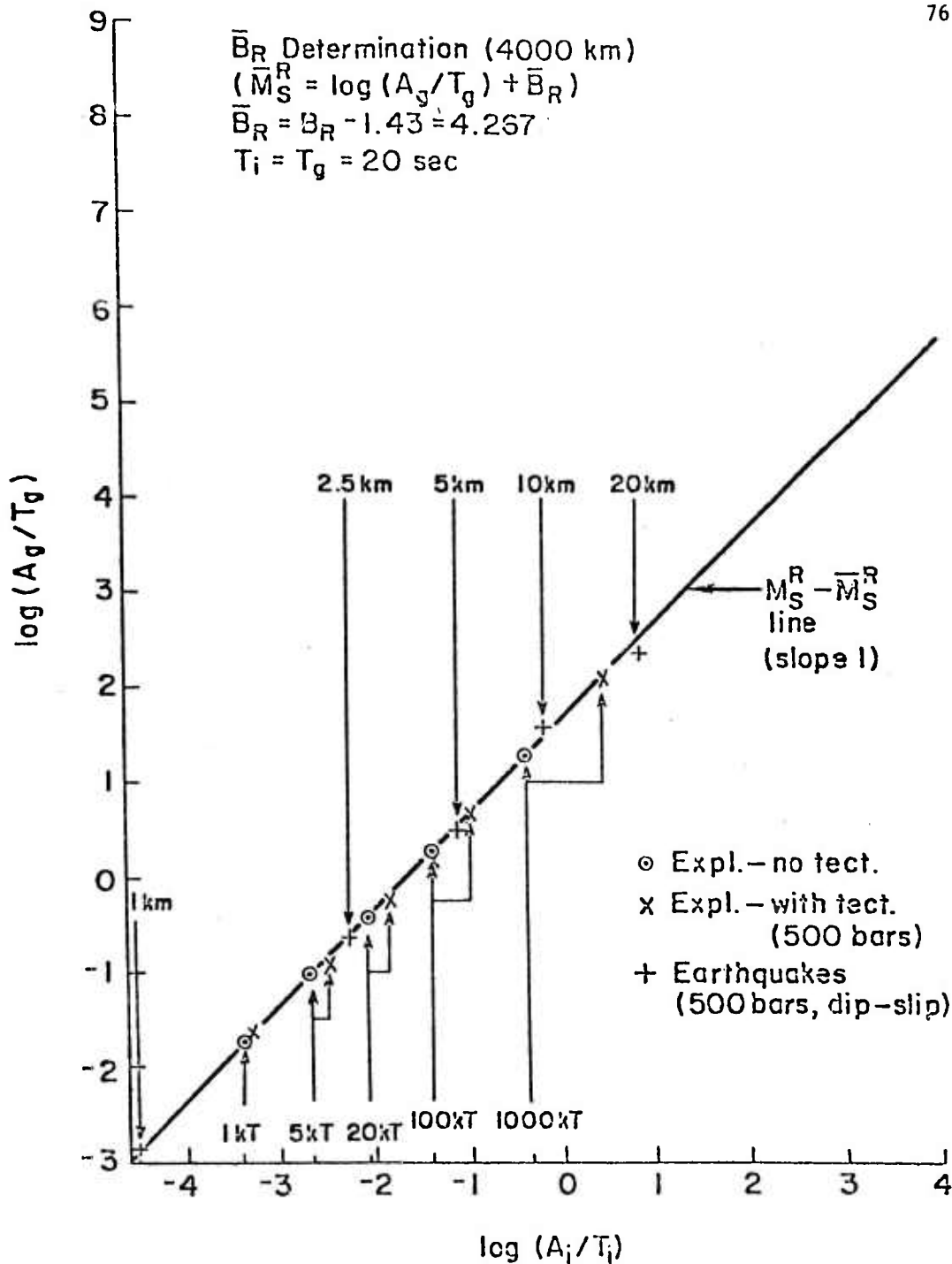


Figure 14. Plot of the log of the narrow band filter amplitude maximum, A_g , normalized by the filter center period T_g , versus A_i and T_i measured from the time domain seismograms; both for Rayleigh type surface waves with $T_g = 20$ sec. and T_i approximately 20 sec. The ratio A_i/T_i is used in the normal surface wave calculation for magnitude while A_g/T_g is used to calculate the "spectral surface wave magnitude". The constant factor of proportionality between the two magnitudes is 1.43 and the relationship is essentially linear over the whole range of events.

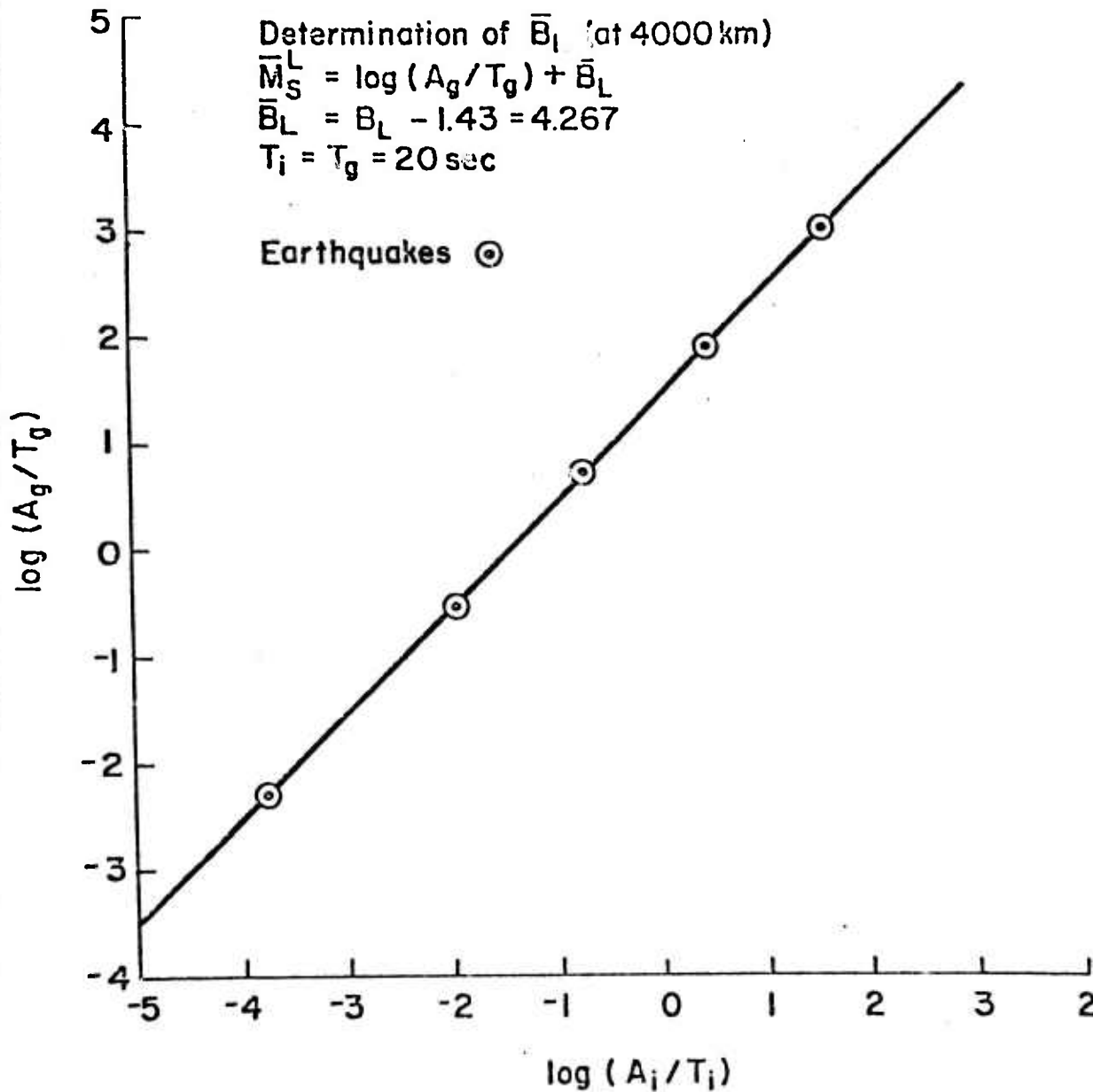


Figure 15. Log of the narrow band filter amplitude maximum, A_g , divided by the filter center period T_g versus A_i/T_i for Love waves at $T_g = T_i = 20$ sec. Surface wave magnitudes computed using the two different amplitude and period definitions are linearly related over the entire range of events, with the constant of proportionality the same as for Rayleigh waves (1.43).

reflections occurring for shallow sources. The $m_b^{(1)}$ value is, therefore, always the best estimator of the direct P wave energy from the source.

Application of the filter technique to a theoretical seismic event is illustrated in Figure 16 . The event is a multiple explosion and we see that the desired "summation" of amplitudes of the individual events is achieved. Further we see, for the high frequency filtering (1 Hz and above), that the maximum of all the envelope maxima occurs at a time corresponding to the signal from the largest event (100 kt) of the series. Note that the largest pulse occurring in the P wave signal train is due to the superposition of later arrival mantle phases and the direct arriving P wave signal (first mantle arrival) from the rest of the 100 kt events of the series. The large pulse is therefore a complicated superposition of several phases, including sP from one or more of the explosions of the series, since we have included tectonic release effects. Even though this composite pulse is large, however, the narrow band filter output, for high center frequencies, peaks at the appropriate first P wave phase from the first of the 100 kt events, as is desired.

Figures 17, 18, 19 and 20 show similar examples for a single-explosion and three different sized earthquakes. Note that in all cases the high frequency narrow band filter output peaks at the time of the first P phase arrival. However it is clear, in all the cases shown, that later arriving P phases, corresponding to second and third mantle arrivals, and pP and sP phases in the case of the shallow events, contain more

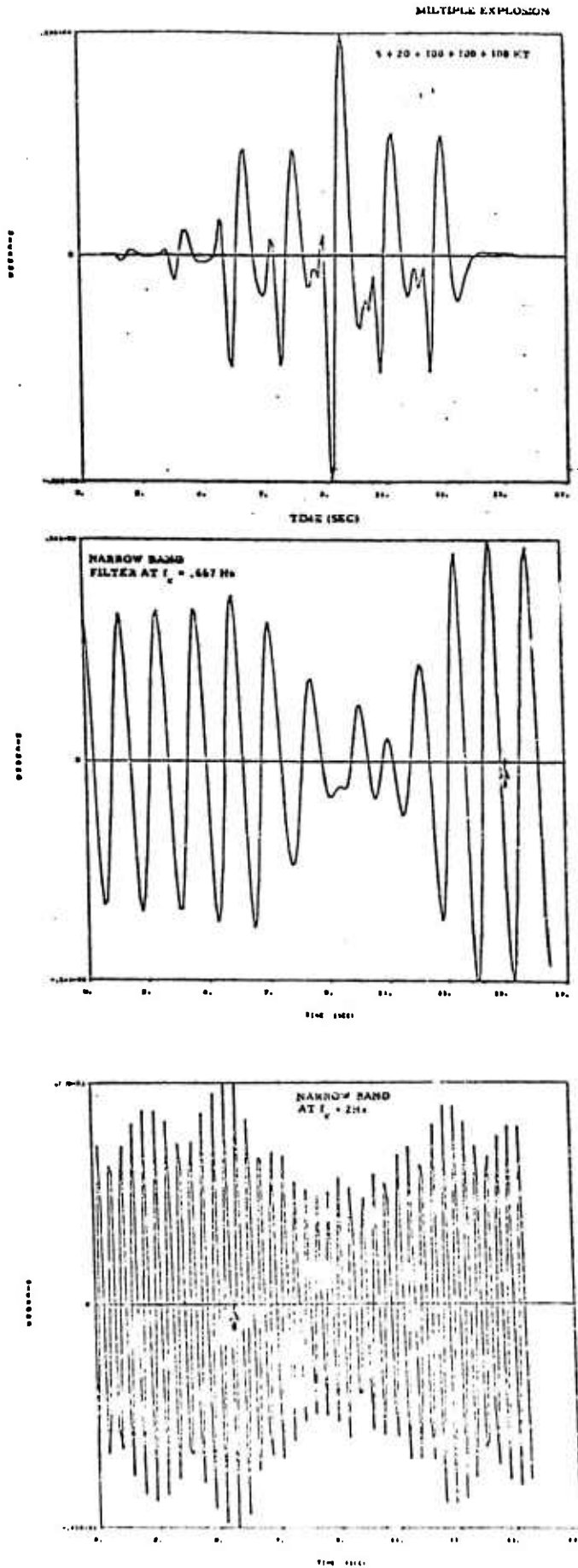


Figure 16. An example of narrow band filter output at two frequencies for a multiple explosion event. The amplitude used for the magnitude calculations is always the maximum of the envelop of the filter output, here indicated by arrows on the time axis. Over the range of filters used (center frequencies from .1 cps to 3 cps), the output amplitudes at the high frequencies peak early and lower frequencies progressively later, as is indicated by these two examples. The amplitude of the filter output is always close to the amplitude of the largest event in the multiple event series and the envelop of the filter output for high frequencies peaks near the arrival time of the P wave from the largest event.

low frequency energy and invariably the low frequency filter output peaks at later times corresponding to the arrival of these phases. It is essential that the 1 Hz filter does peak at the first arrival for earthquakes, for the successful application of this narrow band filtering method as a means of discrimination between multiple and single explosions and earthquakes. If this were not the case, the filter amplitude used for earthquakes would very strongly reflect the large, later arriving, sP and mantle phases and give considerably higher \overline{m}_b magnitude values than would be obtained from the usual m_b measurements in the time domain. Then, even though the \overline{m}_b value for a multiple event is raised to a magnitude reflecting the largest event of the multiple event series, the \overline{m}_b value for the earthquakes would also increase and discrimination of the two kinds of events by $\overline{m}_b - \overline{M}_S$ would probably not be possible. However, as Figures 18 through 20 show, this is not the case, and \overline{m}_b (measured at 1 Hz) reflects the first arrival P phase amplitude, so that \overline{m}_b should not increase significantly over $m_b^{(1)}$ measured in the conventional way. Figure 21 shows the results of the filtering operations on a surface wave from a moderately large earthquake. We see that the low frequency energy arrives first and the high frequency energy later - as we know must be the case since the Love wave of the example is known to be inversely dispersed. All explosions and earthquakes show similar results for both Love and Rayleigh type surface waves.

Applying the filtering systematically to all the theoretical earthquakes and explosions generated in this study yields the $\overline{m}_b - \overline{M}_S^R$

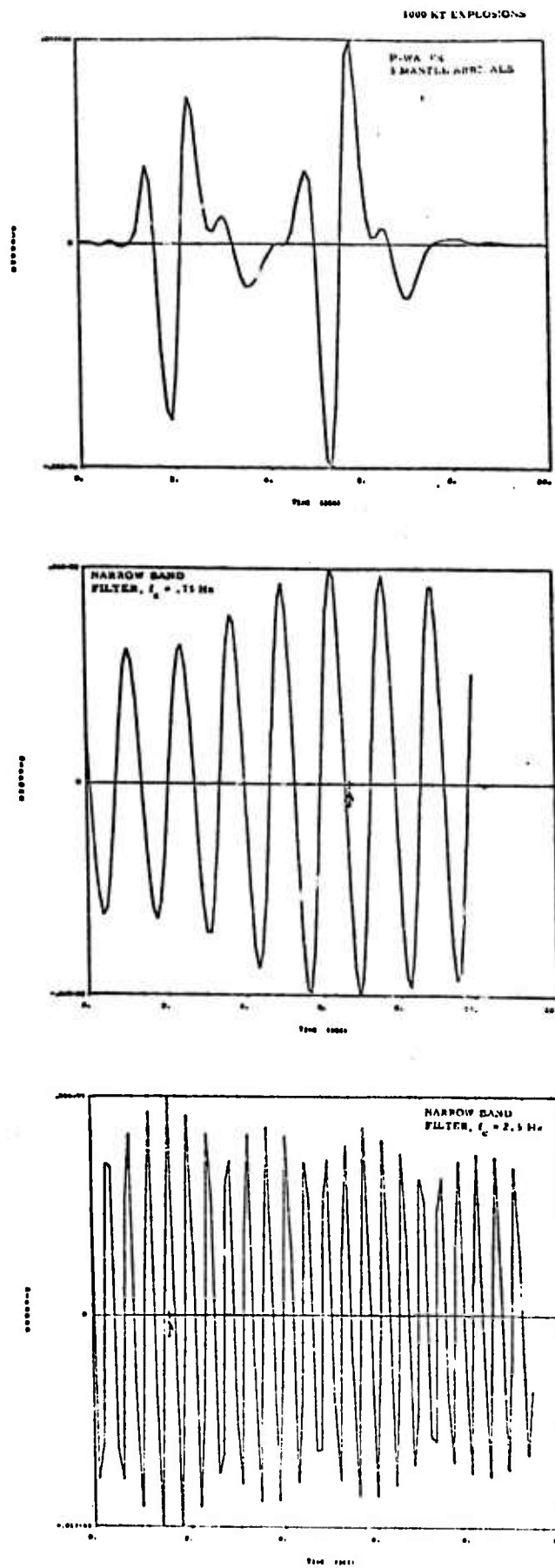


Figure 17. An example of narrow band filter output at two frequencies for a single explosion. The high frequency output peaks at a time corresponding to the first-arrival P wave time for the event. The lower frequency filter output is strongly influenced by the sP contribution from tectonic release and later arriving mantle phases and as a consequence it peaks at a later time.

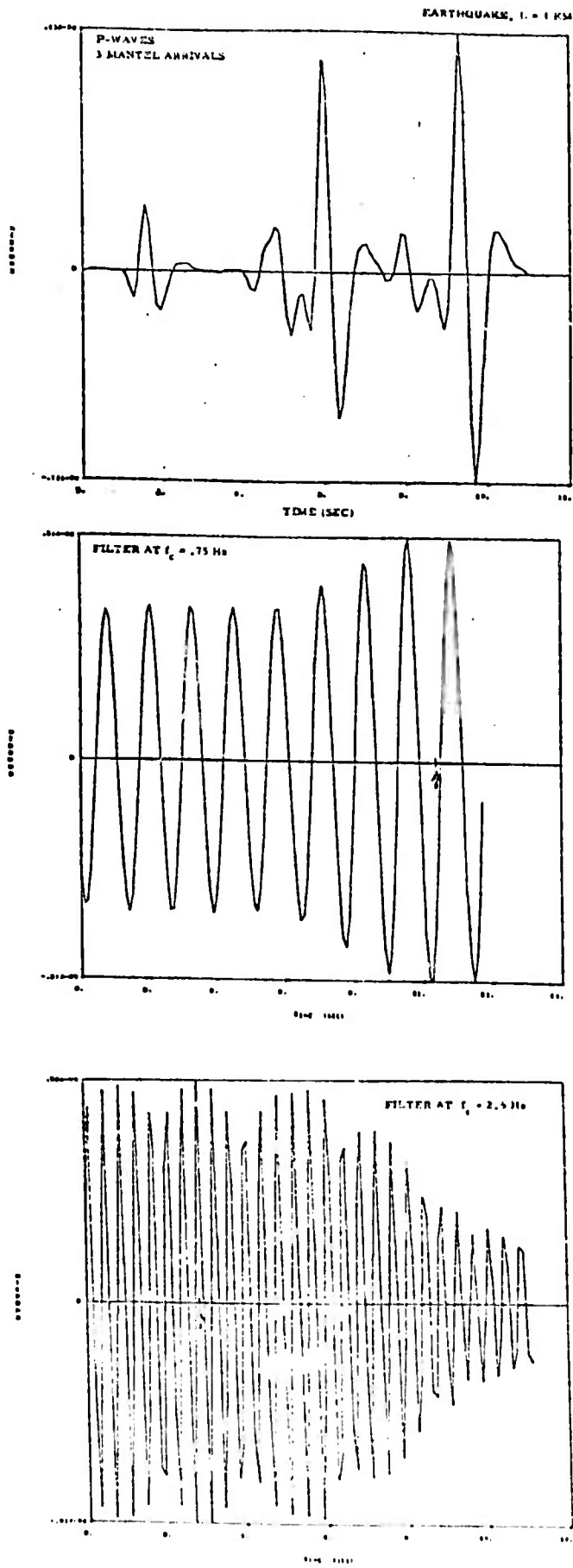


Figure 18. An example of narrow band filter output at two frequencies for a small earthquake. The high frequency filter output peaks earlier than the lower frequency output and at a time close to the first-arrival P wave travel time. The envelop maximum amplitude for the filter output at 1 cps is close to the amplitude measured off the actual seismogram using the first cycle of the first-arrival P wave, but is somewhat higher for small events and somewhat lower for large earthquakes.

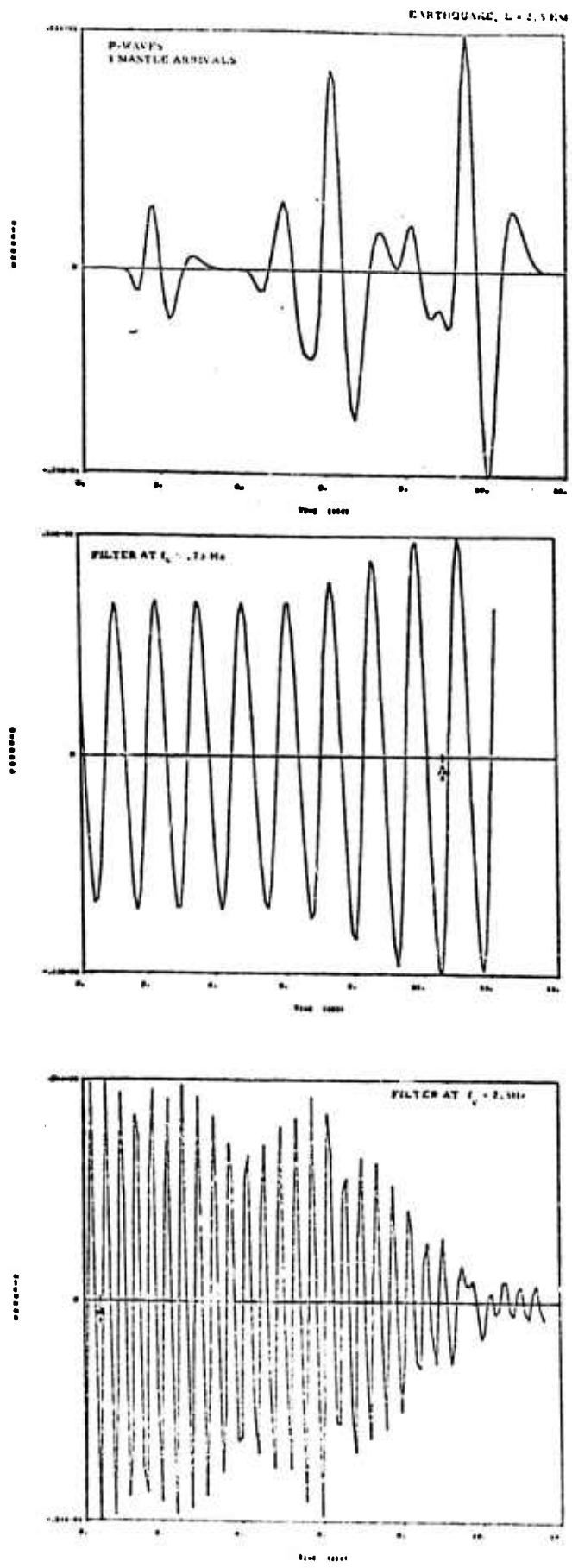


Figure 19 . Narrow band filter output at two frequencies for a moderate earthquake (stress drop of 500 bars). Example again shows high frequencies arriving early relative to low frequencies and near the first arrival P wave time.

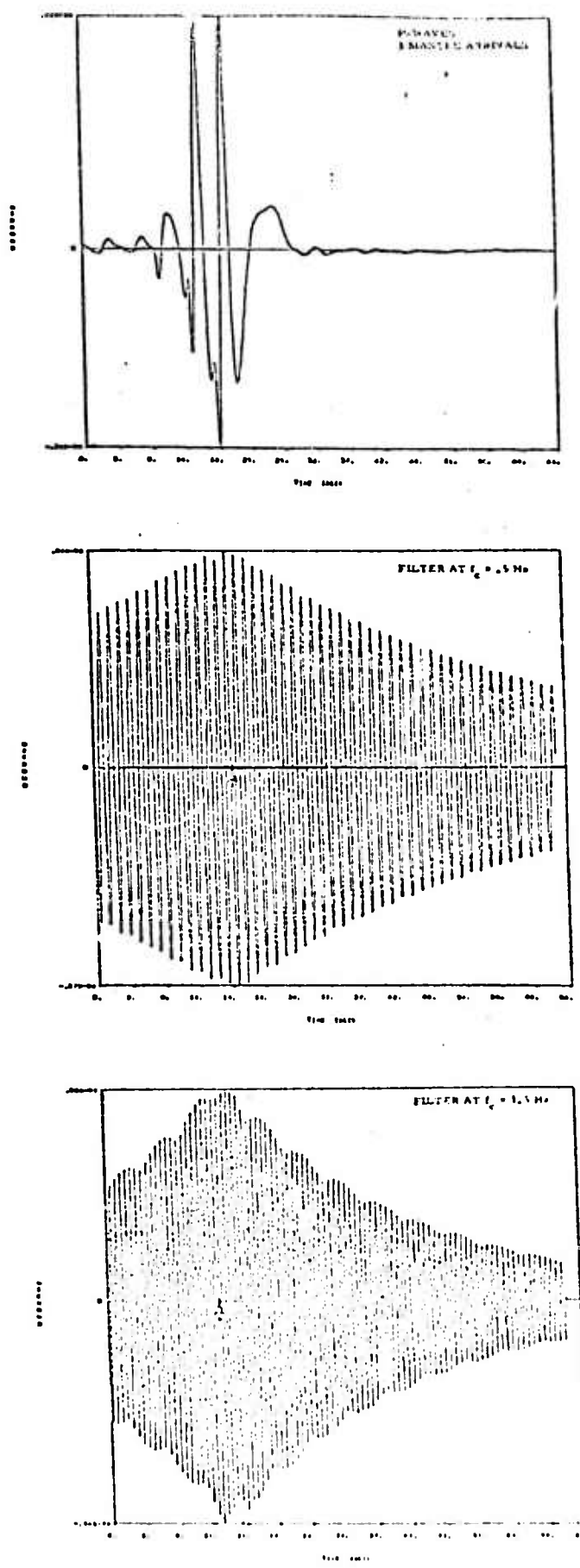


Figure 20. Narrow band filter output at two frequencies for a large earthquake (500 bar stress drop used). Filter envelop maximum is again near first arrival P wave time at high frequencies and later for lower frequencies, even with strong overlap of phases in the time domain.

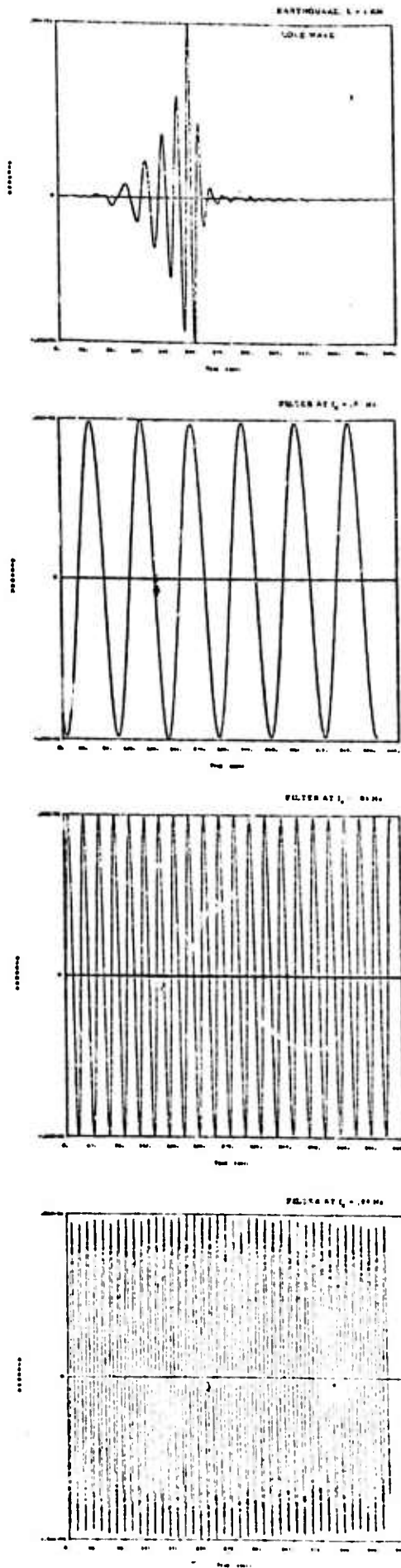


Figure 21. Narrow band filter output from surface waves generated by a moderate sized earthquake. The filter output gives low frequencies arriving first relative to the higher frequencies which is as predicted using the known dispersive characteristics of the structure employed to generate the theoretical seismogram. The maximum in the envelop of the 20 sec. (.05 Hz) filter output is used to calculate the spectral surface wave magnitude \bar{M}_s .

and $\bar{m}_b - \bar{M}_S^L$ data shown in Figures 22 - 25 . In Figure 22 the $\bar{m}_b - \bar{M}_S^R$ values for the multiple explosions of Table 1 are shown along with the $\bar{m}_b - \bar{M}_S^R$ values for the 500 bars and 100 bar prestress "dip slip" earthquakes discussed earlier. We see that all the multiple explosions lie outside of, or just on, the earthquake population boundary line - defined by the 500 bar prestress earthquakes. We note however that if the multiple event number 4 has high prestress associated with it (i.e., around 165 bars), then it will fall within the earthquake population. In general, however, it would be expected that the multiple explosions would be considered as possible explosions, in view of their proximity to the earthquake population boundary. Since only a few earthquakes occur, in a given region, that have $\bar{m}_b - \bar{M}_S^R$ values placing them at the population boundary, it would not be a highly difficult and time consuming task to check all events in this region of the $\bar{m}_b - \bar{M}_S^R$ plane against radiation pattern criteria, or other fairly elaborate discrimination tests.

Figure 23 shows that the $\bar{m}_b - \bar{M}_S^L$ criteria would be more effective in separating multiple explosions and earthquake populations, and hence constitutes a more positive event identification method. All the multiple explosions are well outside the earthquake population for moderate shear prestress conditions (55 - 75 bars), while only the event number 4 is at the earthquake population boundary line for the high prestress case (165 bars).

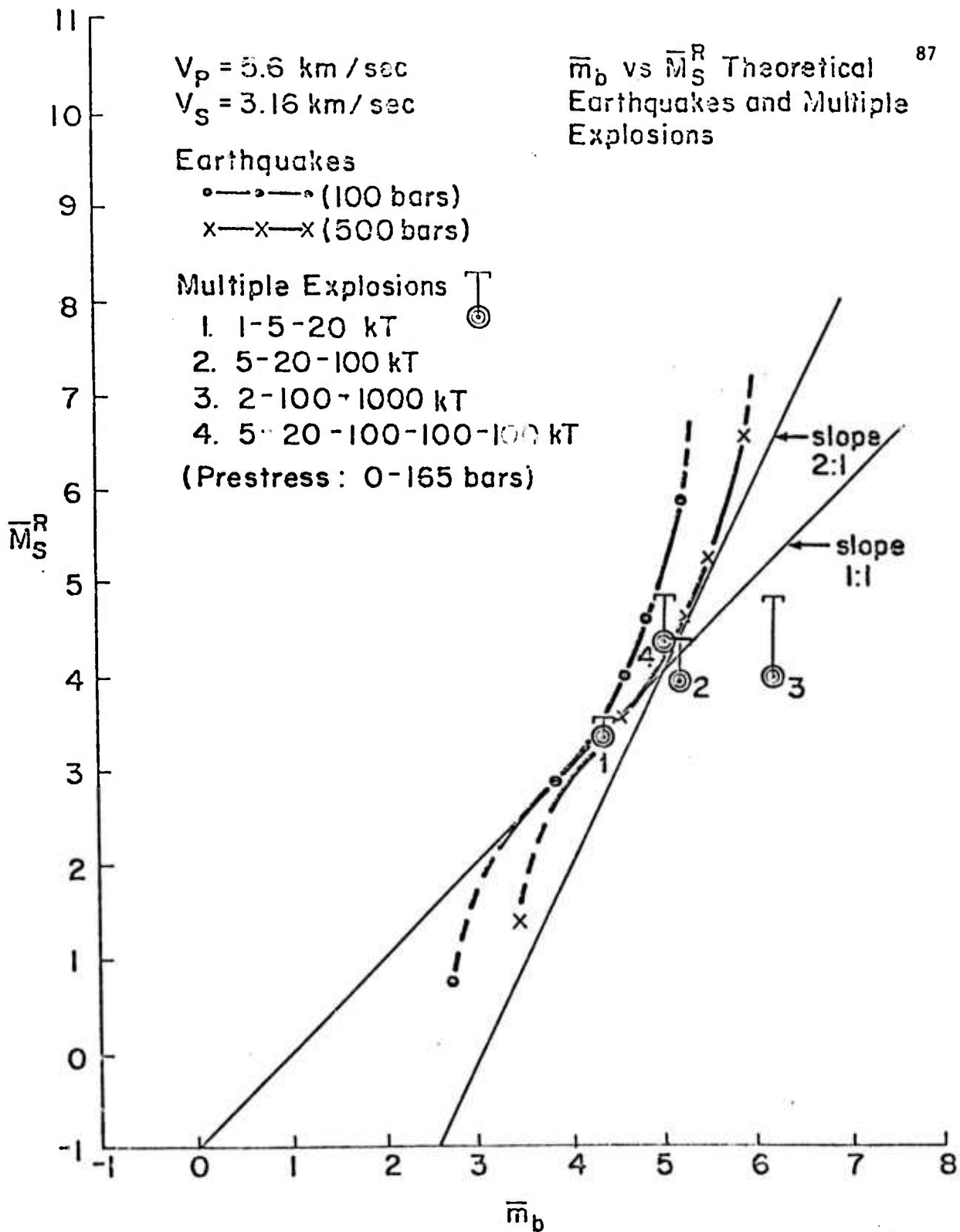


Figure 22. Rayleigh type spectral surface wave magnitude as a function of spectral body wave magnitude for earthquakes and multiple explosions. All events and medium parameters are the same as those used to produce the $m_b - M_S^R$ results of Figure 9. $\bar{m}_b - \bar{M}_S^R$ loci for high rupture (Continued on the following page)

Figure 22 (Continued).

velocity, high and medium stress drop, dip slip earthquakes define the earthquake population in the $\bar{m}_b - \bar{M}_s^R$ plane, with all earthquakes expected to be between these loci or to the left and above them. The multiple explosion \bar{m}_b is larger than the m_b determined in the conventional manner because the \bar{m}_b is most closely related to the magnitude of the largest of the events of the multiple series rather than to the magnitude of the first single event of the series. The range of \bar{M}_s^R for the multiple events is indicated by the vertical bar and corresponds to the range of tectonic contribution due to prestress, from 0 to 165 bars. Some of the multiple events are slightly inside the earthquake population and could not be positively identified as explosions using this $\bar{m}_b - \bar{M}_s^R$ criteria, but would appear as "unusual events".

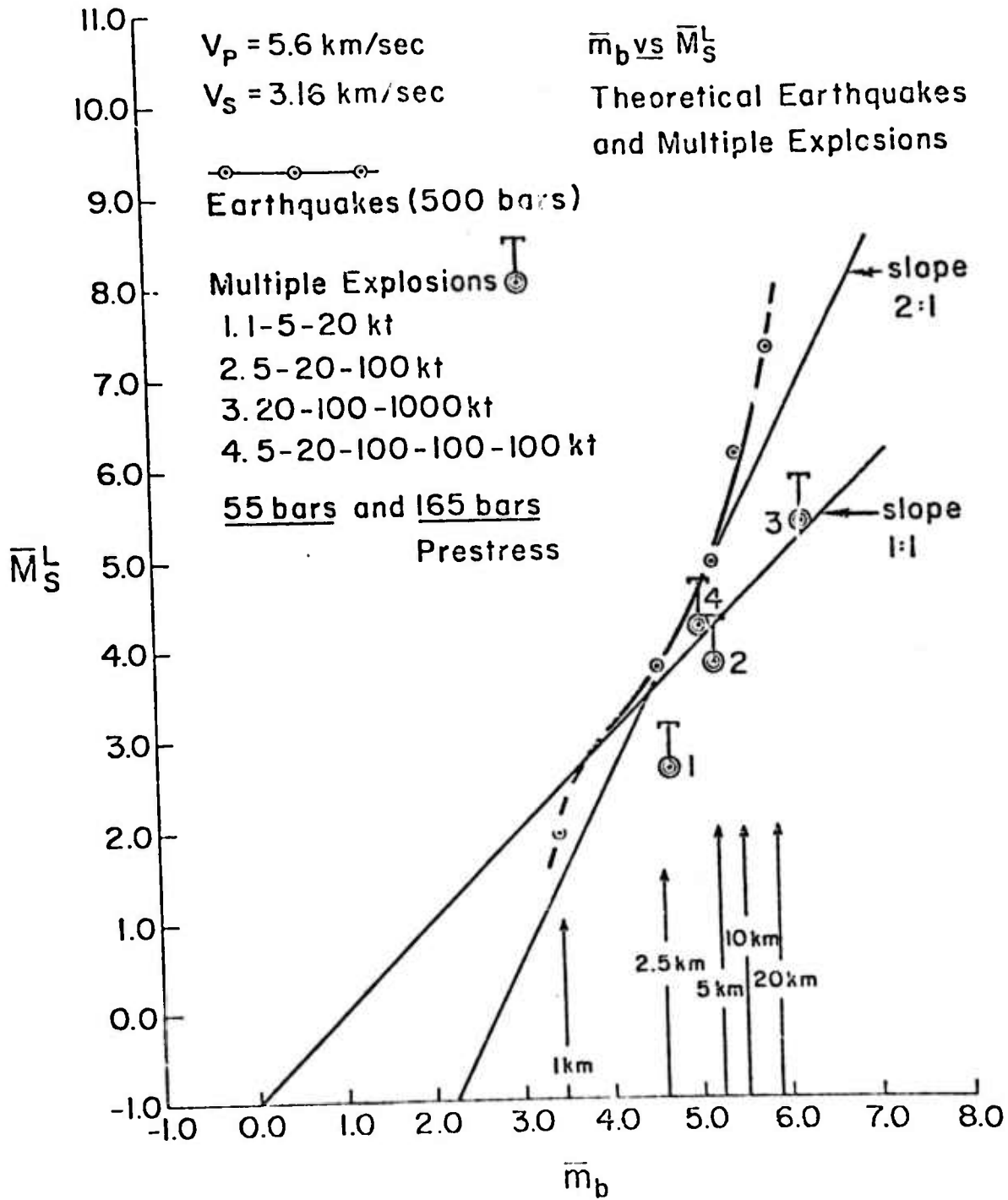


Figure 23. Love type spectral surface wave magnitude as a function of spectral body wave magnitude for earthquakes and multiple explosions. All events and medium parameters are the same as those used to produce previous $\bar{m}_b - \bar{M}_s$ results. All multiple explosions lie outside the earthquake population in the $\bar{m}_b - \bar{M}_s^L$ plane. The loci of earthquake $\bar{m}_b - \bar{M}_s^L$ values shown is the expected extreme limit for earthquakes, all other earthquake $\bar{m}_b - \bar{M}_s^L$ values would lie to the left and above this curve. (Continued on the following page.)

Figure 23 (Continued).

The multiple explosions would be identified as probable explosions, and only for high tectonic release would there be any serious uncertainty, in which case events 2 and 4 would probably be considered "unusual events". For nonhydrostatic prestress levels lower than 55 bars, the explosion $\overline{M}_s L$ values would be lower than shown and identification of these events as explosions more certain.

It is important to also investigate the $\bar{m}_b - \bar{M}_S^R$ results for single explosions as well as for multiple explosions, since discrimination must obviously be maintained for these events as well, if the method is to be applicable. Figure 24 shows the $\bar{m}_b - \bar{M}_S^R$ results for single explosions, with and without tectonic release, along with earthquakes with prestress of 500 and 100 bars. We observe that the populations intersect at around $\bar{m}_b = 4.5$. The same intersection or "cross-over" effect was indicated by the results for the multiple explosions; so that single and multiple explosions are distributed in more or less the same region in the $\bar{m}_b - \bar{M}_S^R$ plane. The reason for this convergence of populations at low magnitudes is primarily due to a decrease in the \bar{m}_b value for small explosions relative to the $m_b^{(1)}$ value that would be measured; while the \bar{m}_b value for earthquakes in this magnitude range is somewhat higher than the $m_b^{(1)}$ value. This can be seen in Figure 13, where the small explosions fall systematically below the $m_b^{(1)} - \bar{m}_b$ line while the earthquakes are systematically above the line, for small events. The divergence is nearly .5 magnitude units for the smallest events.

The physical reasons for this "cross-over" effect will be discussed in part V, where it will be shown that the convergence of the populations can be "postponed" to arbitrarily small magnitudes, through the use of high frequency (greater than 1 Hz) \bar{m}_b measurements. It suffices for the present to note that the $\bar{m}_b - \bar{M}_S^R$ method, as it

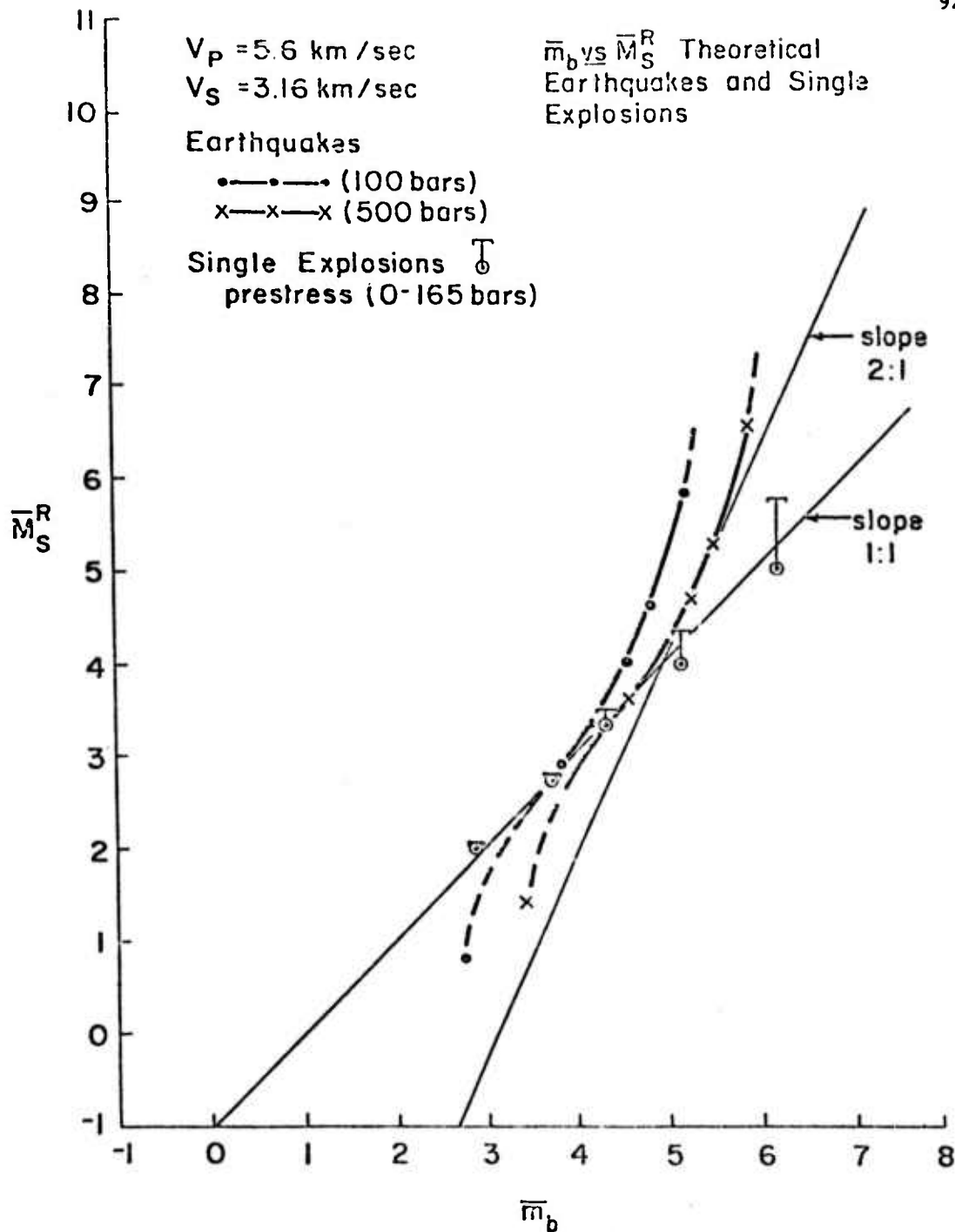


Figure 24. Rayleigh type spectral surface wave magnitude as a function of spectral body wave magnitude for single explosions and earthquakes. All event and and medium parameters are the same as were used to produce previous $\bar{m}_b - M_S$ results. The earthquake loci are for high rupture velocity, high and medium level stress drop, dip slip earthquakes and define the limits
 (Continued on the following page)

Figure 24 (Continued).
of the earthquake population. The single explosion \bar{M}_s^R range is indicated by the vertical bar, corresponding to the range from 0 to 165 bars prestress. The explosion and earthquake populations are well separated at large magnitudes but intersect at \bar{m}_b values near 4.5. If the R_s value for the smallest earthquake was taken to be larger, the earthquake loci would become tangent to the line of unit slope at low magnitudes, whereas here the $\bar{m}_b - \bar{M}_s^R$ value drops below this line due to the choice of a small R_s value. In any case the explosion line would intersect or become tangent to the boundary loci of the earthquake population near $\bar{m}_b = 4.5$ and explosions of lower magnitude could not be positively identified using a $\bar{m}_b - \bar{M}_s^R$ criteria.

stands, will provide the required discrimination between earthquake and explosion events (single and multiple) down to $\overline{m}_b = 4.5$. (At $\overline{m}_b = 4.5$, $m_b^{(1)} \approx 4.5$ also, while m_b measured by the usual procedures would be about 4.7 for explosions and slightly higher than this for earthquakes)

Figure 25 shows the Love wave spectral magnitude \overline{M}_S^L as a function of \overline{m}_b for the single explosions and high stress earthquakes. The explosion \overline{M}_S^L , of course, is due to tectonic release entirely and the level of 55 bars is a nominal level to be expected in most cases, while 165 bars is probably the maximum that would be anticipated. It is clear that the earthquake and explosion populations are well separated and that $\overline{m}_b - \overline{M}_S^L$ data serves as a very effective discriminate for both single and multiple explosions, in view of these results and the results shown in Figure 23.

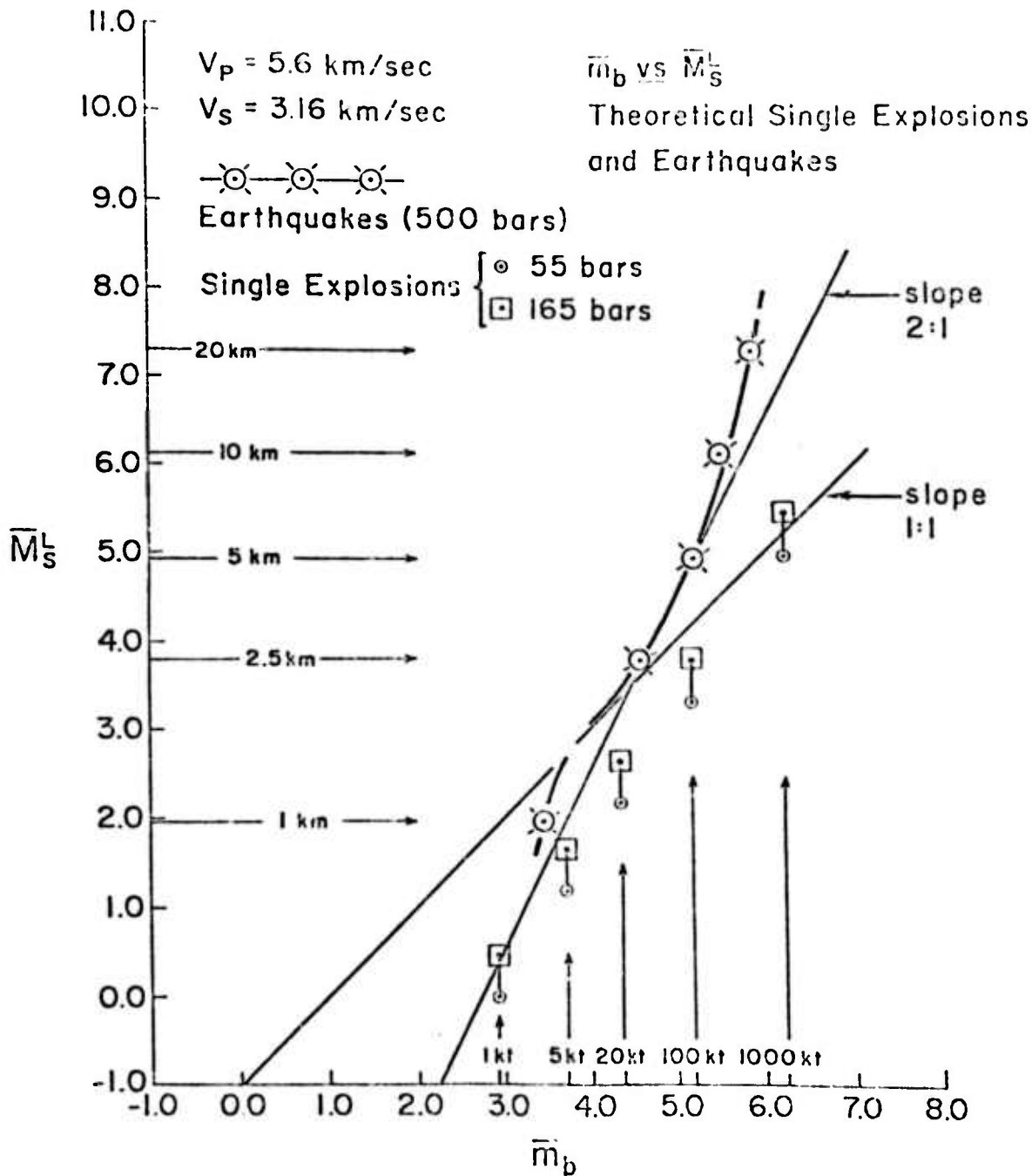


Figure 25. Love type spectral surface wave magnitude as a function of spectral body wave magnitude for single explosions and earthquakes. All event and medium parameters the same as for previous $m_b - M_S$ predictions. Earthquake fault lengths and explosion yields are indicated along the magnitude axes. Only the limiting earthquake loci for the high stress drop events is shown to define the limit of the earthquake population. The explosion \bar{M}_S^L .
(Continued on the following page).

Figure 25 (Continued).

value is totally due to tectonic release, the range from 55 bars (circles) to 165 bars (squares) being the expected extreme range for the effect. Lower prestress values will reduce the \bar{M}_s^L values for explosions drastically. The explosion and earthquake populations are separated by approximately an order of magnitude over the entire range considered.

2. DISCRIMINATION METHODS BASED ON THE $\bar{m}_b(f)$ PARAMETER.

In this part we consider the origins of the convergence of the earthquake and explosion populations in the $\bar{m}_b - \bar{M}_S^R$ plane in detail. This consideration leads to a slight revision of the magnitude based discrimination approach used; to a more general approach wherein we make use of spectral body wave magnitudes computed from narrow band filter output at frequencies other than 1 Hz. The spectral magnitudes so obtained will be denoted as $\bar{m}_b(f)$. In particular, we will generate results for frequencies, f , higher than 1 Hz, and consider then, $\bar{m}_b(f)$ vs. \bar{M}_S^R data as a discriminatory data set. Finally, again on the basis of the spectral differences between earthquakes and explosions of all types, we will consider the use of body wave spectral magnitudes at different frequencies as a basis for discrimination. In this part of the investigation we will use $\bar{m}_b(f_1)$ vs. $\bar{m}_b(f_2)$, with $f_1 < f_2$, as the discriminatory data set. This final investigation leads to event identification procedures that are particularly discriminating and extremely easy to implement, since all that is required are a few arrays of short period seismometers at low noise sites.

(a) Basis for Discrimination.

In considering the spectral basis for discrimination in section (1), it was mentioned that the explosion pP phase could interact with the direct P phase in such a way as to modify the basis

for magnitude discrimination of events. We saw in fact that the earthquake and explosion populations in the $\bar{m}_b - \bar{M}_S^R$ plane do in fact converge at low magnitude. The origin of this convergence is, in fact, primarily due to the pP spectral cancellation that occurs for explosions when a spectral magnitude, \bar{m}_b , is used. This effect does not occur for earthquakes because they are invariably deeper, than 5 km at the hypocenter.

Figure 26 illustrates the spectral relationships between small earthquakes and explosions having nearly the same \bar{M}_S^R , with the explosion being shallow (less than 1 km) and the earthquake near the 5 km "cutoff" depth for earthquake hypocenters. The explosion is assumed to have a moderate tectonic quadrupole component, so that S waves are produced.

For the superposed spectra shown, it is quite clear that the spectral level of the combined P - pP wave for the explosion, which appears as essentially a single pulse form when the event is so shallow, is depressed from the direct P wave spectral level, so that not only will the \bar{M}_S^R values for the explosion and earthquake be nearly the same; but the \bar{m}_b value measured from the 1 Hz level of the P - pP spectrum of the explosion will also be nearly the same as the \bar{m}_b value for the earthquake. On the other hand, while the \bar{m}_b values for the two events are the same, the \bar{M}_S^L values will be about 1 magnitude unit different, since the Love wave

Figure 26 (Continued).

boundary ($\bar{m}_b - \bar{M}_s^R$ "cross-over" effect). The explosion represented is very shallow (depth ~ 200 m.), the earthquake at several kilometers depth. The surface wave magnitude \bar{M}_s^R for the earthquake is determined by the S wave spectral level at .05 cps. and the \bar{M}_s^R for the explosion by the pure P wave spectral levels. In the figure these two levels are essentially equal, as indicated, and the \bar{M}_s^R values will be approximately equal. The \bar{m}_b value is determined by the P plus pP spectral level for the explosion, while the \bar{m}_b value for the earthquake is determined by the pure P wave spectral level. For the event spectra shown, these levels are the same at 1 Hz so that the \bar{m}_b values for the earthquake and explosion will also be the same and the events therefore indistinguishable on the basis of \bar{m}_b vs. \bar{M}_s^R values. However the \bar{M}_s^L value for the explosion is based on the spectral level of the S wave excitation from the tectonic component of the radiation field at .05 Hz which is low relative to the S wave level for the earthquake. Therefore while the \bar{m}_b is the same for the two events, the \bar{M}_s^L values will differ by nearly an order of magnitude and hence the events will be distinguishable on the basis of \bar{m}_b vs. \bar{M}_s^L ($\bar{m}_b - \bar{M}_s^L$ "divergence effect"). For smaller events the normalized amplitude spectra shift to the right relative to the frequency scale shown and the situation illustrated here (\bar{m}_b and \bar{M}_s^R the same for both kinds of events) will remain essentially static, that is the two kinds of events will have nearly the same $\bar{m}_b - \bar{M}_s^R$ values. For larger events, assuming the explosions are at greater depth for larger yields, the spectra shift to the left and while the \bar{M}_s^R values remain roughly the same in this normalized representation, but the \bar{m}_b values for the earthquakes will become much smaller relative to the explosion \bar{m}_b values due to the $1/\omega^3$ fall-off of the earthquake spectra and the increase of the P - pP spectra as the spectral peak approaches the 1 Hz point. Due to the spectral shapes, the $\bar{m}_b - \bar{M}_s^R$ cross-over effect can be shifted to very low magnitudes and the $\bar{m}_b - \bar{M}_s^L$ divergence effect enhanced by measuring the \bar{m}_b at a frequency higher than 1 Hz.

amplitude is proportional to the tectonic S wave component from the explosion and, as shown, the explosion S wave is much lower than the earthquake S wave. Consequently we see that the $\overline{m_b} - \overline{M_S^L}$ data for the two kinds of events will not converge, but will maintain a large separation.

If, however, we were to isolate the P and pP phases in the time domain, as is, in effect, done if $m_b^{(1)}$ is measured, then the measurement of $m_b^{(1)}$ is proportional to the direct P wave spectral level instead of the P - pP level. In this case we see that $m_b^{(1)}$ would be larger than $\overline{m_b}$ for the explosion and the convergence of the populations would not occur. Hence ordinary $m_b - M_S$ criteria would not suffer from this convergence phenomenon, so long as $m_b^{(1)}$ is measured. It is not clear, theoretically at least, whether convergence would occur if $m_b^{(2)}$ or $m_b^{(3)}$ were measured and used for the time domain m_b measurement, since these magnitudes would be partially contaminated by the pP arrival and could very well have values, at 1 Hz, near $\overline{m_b}$. In practice, even when $m_b^{(2)}$ or $m_b^{(3)}$ are used for m_b , this effect is avoided because the measurement is in actuality made at a higher frequency than 1 Hz and the cancellation effect is avoided, in terms of the explanation given here, by moving the measurement of m_b to a higher frequency. That is, from Figure 26 we see that if the body wave magnitude measurement were made at a higher frequency for the explosion, the pP cancellation would not reduce the P wave

spectral level as much, and the body wave magnitude obtained for the explosion would be higher than that for the earthquake. If we also measured the body wave magnitude of the earthquake at this higher frequency, then it would be lower than the value at 1 Hz, due to the high frequency spectral roll-off above the corner frequency, as shown in the figure.

In view of these relationships, it is clear that if the body wave spectral magnitude is always measured at a frequency higher than 1 Hz, then the convergence of the populations will occur at a lower magnitude and for all practical purposes can be effectively "postponed" to magnitudes so low as to be of no interest. Therefore the $\overline{m}_b - \overline{M}_S^R$ criteria can be made to function as a discriminate in almost precisely the same way as the ordinary $m_b - M_S$ criteria, but with the added feature of providing multiple explosion identification. Naturally the explosion and earthquake populations will be even further separated in the $\overline{m}_b - \overline{M}_S^L$ plane if \overline{m}_b is measured at a higher frequency.

Another aspect of the spectral differences between explosions and earthquakes, illustrated in Figure 26 and indirectly by the previous discussion, is the basic differences in the P - pP explosion spectra and the P wave earthquake spectra. In Figure 26 we note that any measurement of \overline{m}_b at "low" frequency, that is below 1 Hz, will give an \overline{m}_b for the earthquake and the explosion of nearly the same value, while any measurement of \overline{m}_b at high frequency above 1 Hz will give an \overline{m}_b for the earthquake that is significantly smaller

than that for the explosion. This will be the case for the events shown in Figure 26 and certainly for all larger events. It will also be the case for smaller events down to some magnitude level where the high frequency \bar{m}_b measurement occupies the same position relative to the spectra shown, as does the 1 Hz measurement indicated in Figure 26. If the high frequency \bar{m}_b measurement is at high enough frequency, then the difference will exist over the entire range of events of interest and significance. This difference can obviously be used for event identification and function as a discrimination method based solely on the compressional waves from earthquakes and explosions. Since P waves are most easily detected, with the simplest instrumentation, this approach is highly desirable.

The entire basis of this P wave magnitude discrimination method is illustrated by the theoretical event spectra in Figure 27. In the figure the entire range of explosion events of interest is shown, along with earthquake spectra corresponding to the most explosion-like earthquakes. The variation of the spectra with event parameter variations is also shown and discussed in the figure caption, so that changes in the spectral relationships can be anticipated. The earthquakes are chosen such that the compressional wave spectral amplitude is about the same as the explosion P + pP spectra at $f = .3$ Hz. Thus, an \bar{m}_b computed at $f = .3$ Hz will be the same for particular earthquake-explosion pairs. However, \bar{m}_b values computed at any frequency

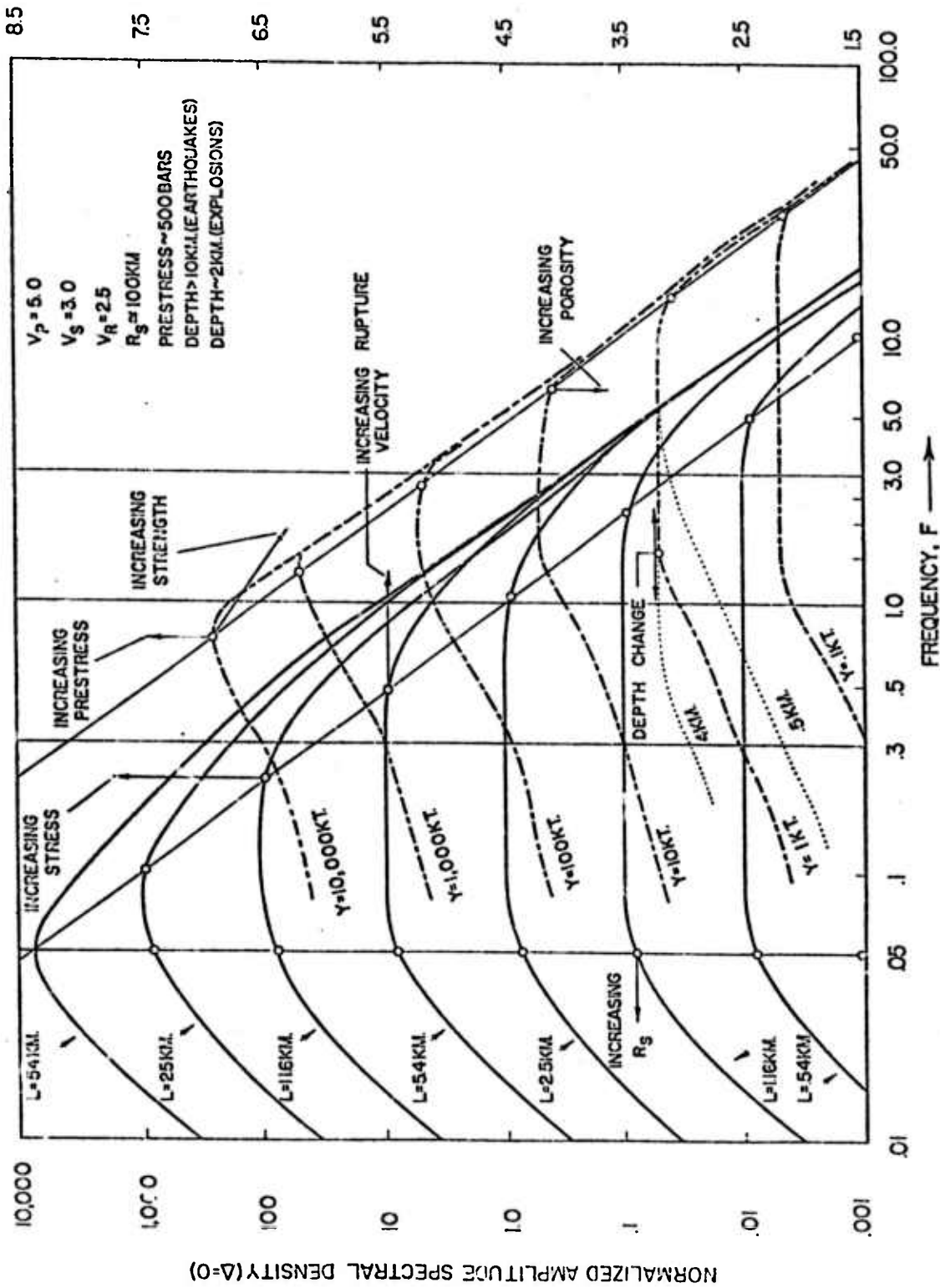


Figure 27. Spectral basis for frequency dependent magnitude discriminants involving high frequency body wave magnitudes. Shown are theoretical earthquake compressional wave spectra parameterized by rupture length and theoretical explosion compressional wave spectra parameterized by yield. All (Continued on the following page)

spectra are normalized to the $L = 2.5$ km. earthquake amplitude spectral density and represent the spectral amplitudes before propagation through the bulk of the earth. The approximate magnitude scale shown and the relative spectral levels between the earthquakes and explosions are for high stress drop, high rupture velocity earthquakes and explosions with no tectonic release; with depth and medium parameters fixed as indicated in the Figure. Different values for these event parameters will change the spectral levels (and spectral shapes to a lesser extent) as indicated in the Figure. For example, increasing the prestress level for the explosion results in a contribution to the direct compression wave train from the directly radiated P wave and from the free surface converted sP phase, both of which will generally be inseparable from the explosion P plus pP waves for shallow explosions (depths less than 5 km.) and result, generally, in an overall increase in the spectral level of the observed compressional wave from the explosion. This is indicated on the curve for the 10,000 kt explosion and applies to all the explosion spectra as well. As with the prestress, increasing (or decreasing) porosity and medium strength for explosions shifts the entire spectrum in the directions indicated (or in the opposite sense for decreases), with relatively small change in the spectral shape. This is also the case for prestress level changes for earthquakes, as indicated. For changes in explosion depths, the P-pP spectrum changes shape in the manner indicated for the 1 kt event, where the low frequencies are affected such that cancellation between the low frequency P and pP begins at a higher frequency for smaller depths. Thus only the frequency point where cancellation begins will change with depth, the remainder of the spectrum being invariant. (Of course the medium strength, porosity and the prestress level may change with depth and so depth changes may result in other changes in the spectrum implicitly, through the other spectral parameters.) Similarly, for changes in R_s the "low frequency" part of the spectrum for an earthquake changes shape such that the characteristic frequency at which the spectrum begins to decrease shifts to higher frequency for lower R_s values. The affect on the earthquake spectrum is very similar to the affect of depth on the explosion P-pP spectrum. Changes in the earthquake rupture velocity on the other hand produce, primarily, changes in the high frequency part of the spectrum and to first order the frequency beyond which the spectrum begins to rapidly decrease shifts to higher frequencies with increasing rupture velocity and oppositely for decreasing rupture velocity. For these changes, however, the spectrum also changes shape somewhat, in particular as the rupture velocity decreases and the "corner frequency" shifts to lower frequencies, the amplitude spectrum decreases less rapidly at frequencies above the corner frequency than is the case for higher rupture velocities. The spectrum for low rupture velocity earthquakes will have a slope of $1/\omega$ and $1/\omega^2$ over an appreciable frequency band before assuming the $1/\omega^3$ slope, which is characteristic of high rupture velocity earthquakes. Further the low frequency spectral level is somewhat higher for the lower rupture velocity events.

For the event spectra shown, the earthquakes are as near to being explosion-like as is likely in terms of the parameter range appropriate for the earth. For these extreme events, comparison

Figure 27 (Continued).

shows that the explosion and earthquake pair having the same spectral amplitude at $f = .3$ Hz (e.g., the $L = 2.5$ km. earthquake and the 100 kt. explosion) will have very different spectral amplitude at higher frequencies, with the earthquake being much lower in amplitude at high frequency. Thus, if the spectral amplitudes at 3 Hz are compared for the pairs having the same level at .3 Hz, the earthquake level is seen to be more than an order of magnitude less than the explosion amplitude level for all events shown. Thus if amplitude spectral values for earthquakes and explosions are plotted, for example, in the parameter space $A_p(3) - A_p(.3)$ (P wave amplitude at 3 Hz versus that at .3 Hz), the earthquake and explosion populations should separate by more than an order of magnitude. Further, due to the nature of the spectral changes with event variable changes (prestress, strength, porosity, etc.) this difference in the populations should always exist to about the same degree in this particular parameter space, except perhaps for deep explosion events with magnitudes less than about $m_b = 3.0$. However, for such explosions in low magnitude ranges, a large separation from earthquakes will still exist if a higher frequency amplitude parameter space is used, for example $A_p(5) - A_p(.3)$.

higher than .3 Hz for the same pair will yield higher values for the explosion than for the earthquake, for all events over the entire range shown. Thus the spectral differences, namely the greater high frequency content of explosions relative to earthquakes with comparable low frequency spectral levels, can be used to establish a body wave magnitude discrimination procedure involving comparisons of $\overline{m}_b(f_1)$ vs. $\overline{m}_b(f_2)$, where $f_1 < f_2$. The larger the difference between the frequencies f_1 and f_2 the greater will be the separation between the explosion and earthquake populations. Further as we have seen this method will also yield multiple explosion identification.

From the preceding discussion it is evident that variable frequency spectral magnitudes are required for implementation of what appears to be a powerful discrimination procedure. Computation of the required $\overline{m}_b(f)$ values is straightforward and in Figure 28 we show the relationship of various computed $\overline{m}_b(f)$ values to the $m_b^{(1)}$ value for theoretical earthquakes. The $\overline{m}_b(1.0)$ values for a range of earthquakes is close to $m_b^{(1)}$ for the same event, as should be the case since $\overline{m}_b(1.0)$ was constructed so as to be close to $m_b^{(1)}$. However, only at $m_b^{(1)} = 5.0$ are they actually equal. The most significant aspect of this figure is the manner in which the m_b values are systematically reduced as f increases. On the other hand, for $f = .3$ Hz the \overline{m}_b curve lies above the unit slope line in the $\overline{m}_b(f) - m_b^{(1)}$ plane, showing that $\overline{m}_b(f)$ values for $f < 1$ Hz are systematically larger than $\overline{m}_b^{(1)}$ (and $m_b(1.0)$) values.

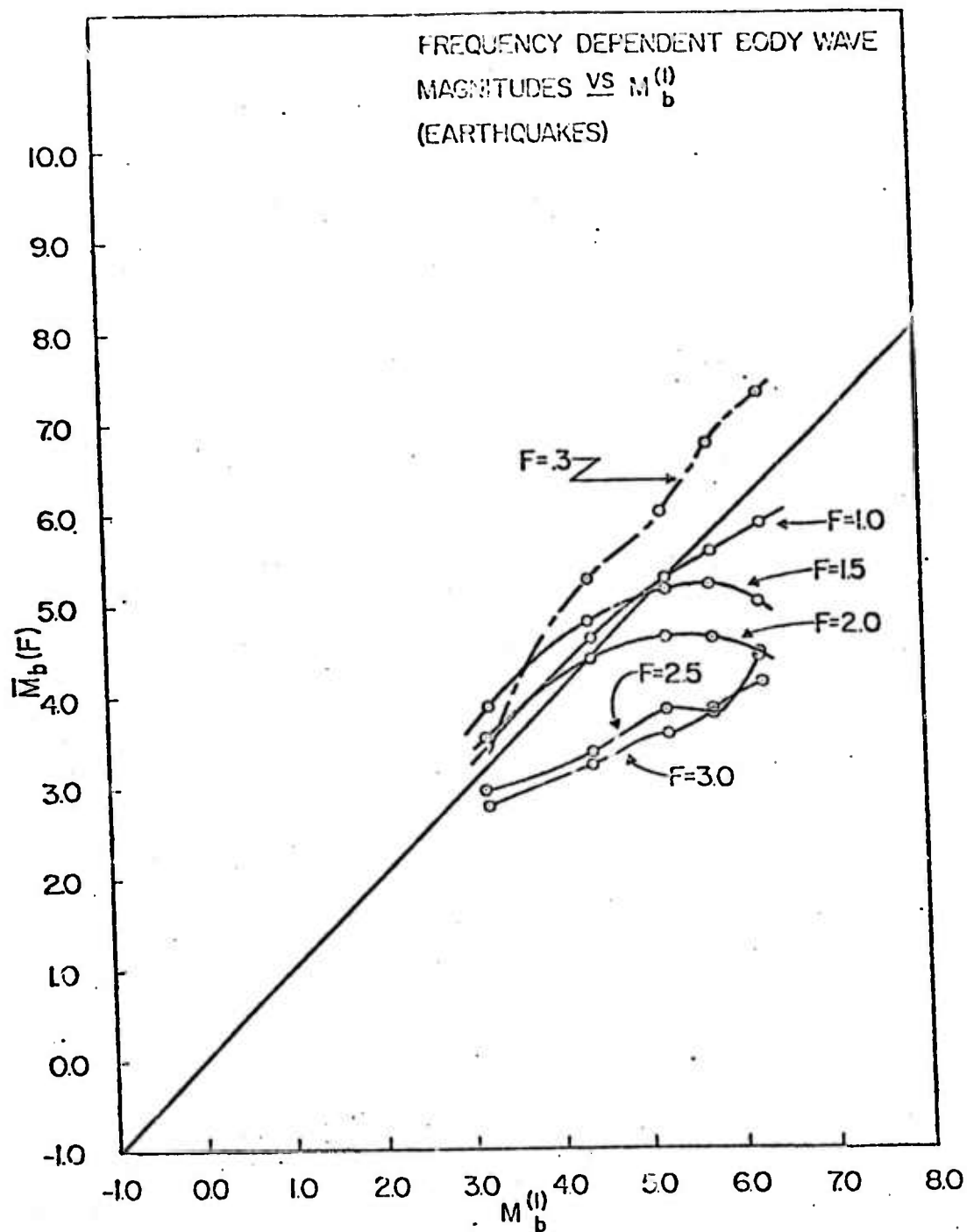


Figure 28.: Frequency dependent spectral magnitudes $\bar{m}_b(f)$ as functions of the conventional body wave magnitude $\bar{m}_b^{(1)}$ for earthquakes.

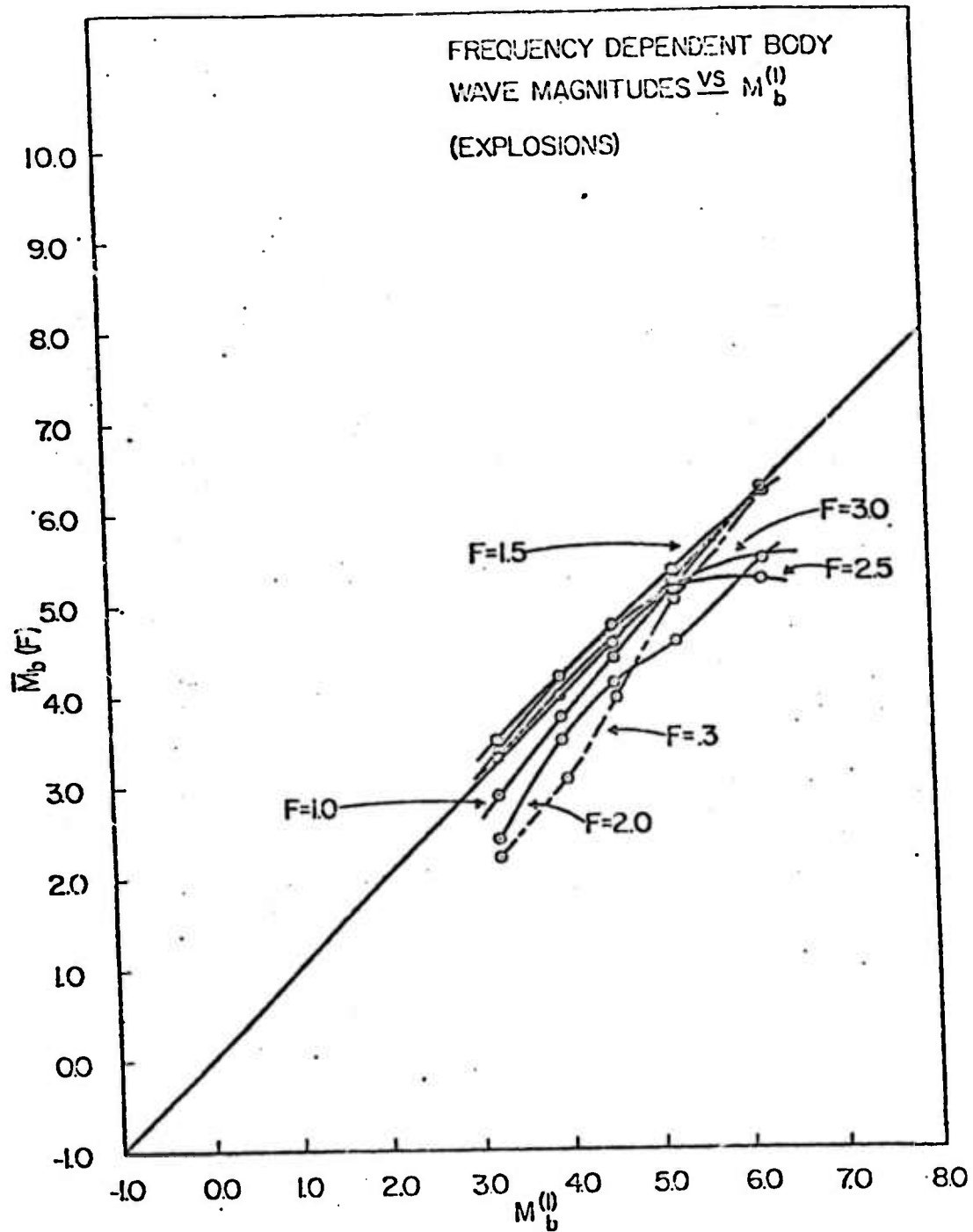


Figure 29 . Frequency dependent spectral magnitudes $\bar{m}_b(f)$ as functions of the conventional body wave magnitude $\bar{m}_b^{(1)}$ for explosions.

In Figure 29 we see that the situation is quite different for explosions. In particular, while the $\overline{m}_b(f)$ values drop below the $m_b^{(1)}$ values for $f > 1$ Hz, as is the case for earthquakes, the decrease is not nearly so large. Further, and most importantly, the $\overline{m}_b(f)$ values for $f < 1$ Hz also are less than the $m_b^{(1)}$ values, whereas they were significantly larger for earthquakes. Indeed, comparing the $\overline{m}_b(.3)$ line for earthquakes with the same line for explosions shows that they are similar in slope, but offset, uniformly, by about one magnitude unit. Clearly the ratio of low frequency bodywave magnitude to the high frequency body wave magnitude at any of the frequencies above $f = 1$ Hz, will be much larger for earthquakes than for explosions.

A compilation of all the magnitude calculations for all the theoretical events used in this study is given in Table 2, along with details concerning the event parameters. This data is used in the next two sections to generate the event discrimination criteria discussed in this section.

TABLE 2- EVENT MAGNITUDES^a

Event	$m_0^{(1)}$	$m_0^{(2)}$	$m_0^{(1,5)}$	$m_0^{(2,5)}$	$m_0^{(3,10)}$	M_R 105 bars no prestress	M_L no prestress	M_R 105 bars, no prestress	M_L no prestress	M_R 105 bars, no prestress	M_L no prestress	Event Description
1-10-Exp.	3.24	3.37	3.35	3.37	3.40	2.2	1.76	2.65	1.92	2.0	1.49	R_0 = slatter zone radius = 152 m., depth = 100 m., pure shear prestress P_0 (relaxation radius) = 100 m., $\nu = 1.5$ km., $\nu_p = 3.1$ km., $\nu_r = 3.1$ km., $\nu_s = 3.1$ km.
3-10-Exp.	3.14	3.14	3.22	3.16	3.16	3.06	2.46	2.79	1.42	2.7	1.44	R_0 = 210 m., depth = 100 m., pure shear prestress P_0 = 10 R_0 = 2.1 km., $\nu = 3.1$ km., $\nu_p = 3.1$ km., $\nu_r = 3.1$ km., $\nu_s = 3.1$ km.
2-10-Exp.	3.35	3.6	3.37	3.43	3.61	3.48	3.00	3.48	2.42	3.3	2.46	R_0 = 400 m., depth = 415 m., pure shear prestress P_0 = 10 R_0 = 4.1 km., $\nu = 3.1$ km., $\nu_p = 3.1$ km., $\nu_r = 3.1$ km., $\nu_s = 3.1$ km.
10-10-Exp.	3.23	3.33	3.27	3.26	3.33	3.01	3.76	4.37	3.04	4.0	3.82	R_0 = 700 m., depth = 7 km., pure shear prestress P_0 = 10 R_0 = 7.1 km., $\nu = 3.1$ km., $\nu_p = 3.1$ km., $\nu_r = 3.1$ km., $\nu_s = 3.1$ km.
10-10-Exp.	3.23	3.26	3.35	3.46	3.46	3.16	4.75	5.81	3.46	5.0	3.46	R_0 = 1500 m., depth = 1525 m., pure shear prestress P_0 = 10 R_0 = 15 km., $\nu = 3.1$ km., $\nu_p = 3.1$ km., $\nu_r = 3.1$ km., $\nu_s = 3.1$ km.
10-10-Exp.	3.24	3.27	3.4	3.43	3.53	3.15	3.30	3.34	2.72	3.34	3.61	Individual event parameters of the multiple series are the same as those listed above. See Table 1 for details of event separation in time and space.
10-10-Exp.	3.18	3.2	3.31	3.21	3.32	3.13	4.13	4.42	3.87	4.42	3.85	Individual event parameters of the multiple series are the same as those listed above. See Table 1 for details of event separation in time and space.
2-20-10-Exp.	3.45	3.5	3.48	3.51	3.71	3.16	5.61	4.83	3.51	4.83	3.46	Individual event parameters of the multiple series are the same as those listed above. See Table 1 for details of event separation in time and space.
10-10-Exp.	3.45	3.48	3.54	3.46	3.65	3.16	4.53	4.82	4.28	4.82	4.27	Individual event parameters of the multiple series are the same as those listed above. See Table 1 for details of event separation in time and space.
2-3-10-Exp.	3.21	3.14	3.40	3.31	3.36	3.36	1.2	1.41	2.15	1.41	1.97	Depth = 10 km., body waves; depth reflector = 1 km., surface waves R_0 (relaxation radius) = 10 km., $\nu = 3.1$ km., $\nu_p = 3.1$ km., $\nu_r = 3.1$ km., $\nu_s = 3.1$ km.
2-3-10-Exp.	3.4	3.33	3.78	3.36	3.22	3.29	3.44	3.62	3.76	3.62	3.76	Depth = 2 km., body waves; depth reflector = 1 km., surface waves R_0 (relaxation radius) = 10 km., $\nu = 3.1$ km., $\nu_p = 3.1$ km., $\nu_r = 3.1$ km., $\nu_s = 3.1$ km.
3-10-Exp.	3.25	3.3	3.27	3.15	3.57	3.0	4.60	4.74	4.97	4.74	4.95	Depth = 10 km., body waves; depth reflector = 1 km., surface waves R_0 (relaxation radius) = 10 km., $\nu = 3.1$ km., $\nu_p = 3.1$ km., $\nu_r = 3.1$ km., $\nu_s = 3.1$ km.
10-10-Exp.	3.22	3.01	3.55	3.23	3.81	3.75	5.68	5.82	6.15	5.82	6.15	Depth = 10 km., body waves; depth reflector = 1 km., surface waves R_0 = 15 km., $\nu = 3.1$ km., $\nu_p = 3.1$ km., $\nu_r = 3.1$ km., $\nu_s = 3.1$ km.
3-10-Exp.	3.24	3.2	3.01	4.45	4.10	7.3	6.55	6.6	7.35	6.6	7.33	Depth = 10 km., body waves; depth reflector = 1 km., surface waves R_0 = 10 km., $\nu = 3.1$ km., $\nu_p = 3.1$ km., $\nu_r = 3.1$ km., $\nu_s = 3.1$ km.

^a Magnitudes compared at 10 km depth, and at an azimuth of 30° using the earth model CIT-100 with the 10 km anelastic model. All magnitudes are 105 bars prestress unless otherwise noted; all earthquakes 500 bars prestress, slip slip velocity. Scaling for other prestress conditions is linear in amplitude.

(b.) Event Discrimination Using High Frequency Body Wave Magnitudes and Surface Wave Magnitudes ($\bar{m}_b(f)$ vs \bar{M}_S)

Figure (20) shows the distribution of multiple and single explosions in the $\bar{m}_b(1.5) - \bar{M}_S^R$ plane, relative to the earthquake population. Comparison with the results using $\bar{m}_b(1.0)$ instead of $\bar{m}_b(1.5)$ (shown in Figures (22) and (26)) clearly indicates that the population separation is now greater. The intersection of the two populations occurs near $\bar{m}_b(1.5) = 4.0$, and all explosions above 5 kT appear to be identifiable as explosions or as possible explosions.

Pursuing the idea that use of even higher frequency body wave magnitudes will give greater event population separation, we show the populations for earthquakes and explosions in the $\bar{m}_b(2.5) - \bar{M}_S^R$ plane in Figure (31). We see, as expected, that the separation of populations has expanded and that positive identification of events can clearly be made down to explosion yields of around 1 kT, using this criteria.

Figure (32) shows the populations in the $\bar{m}_b(1.5) - \bar{M}_S^L$ plane. As was the case before (i.e. when $\bar{m}_b(1.0)$ was used) the populations are well separated, but now the separation is somewhat greater. Obviously multiple explosions look almost exactly like single explosions for all the $\bar{m}_b(f) - \bar{M}_S^R$ and $\bar{m}_b(f) - \bar{M}_S^L$ plots. Even wider separation is achieved in the $\bar{m}_b(2.5) - \bar{M}_S^L$ plane as shown in Figure (33). As has been noted in the figure captions, only the size of R_S , the prestress zone characteristic dimension, alters this picture to any

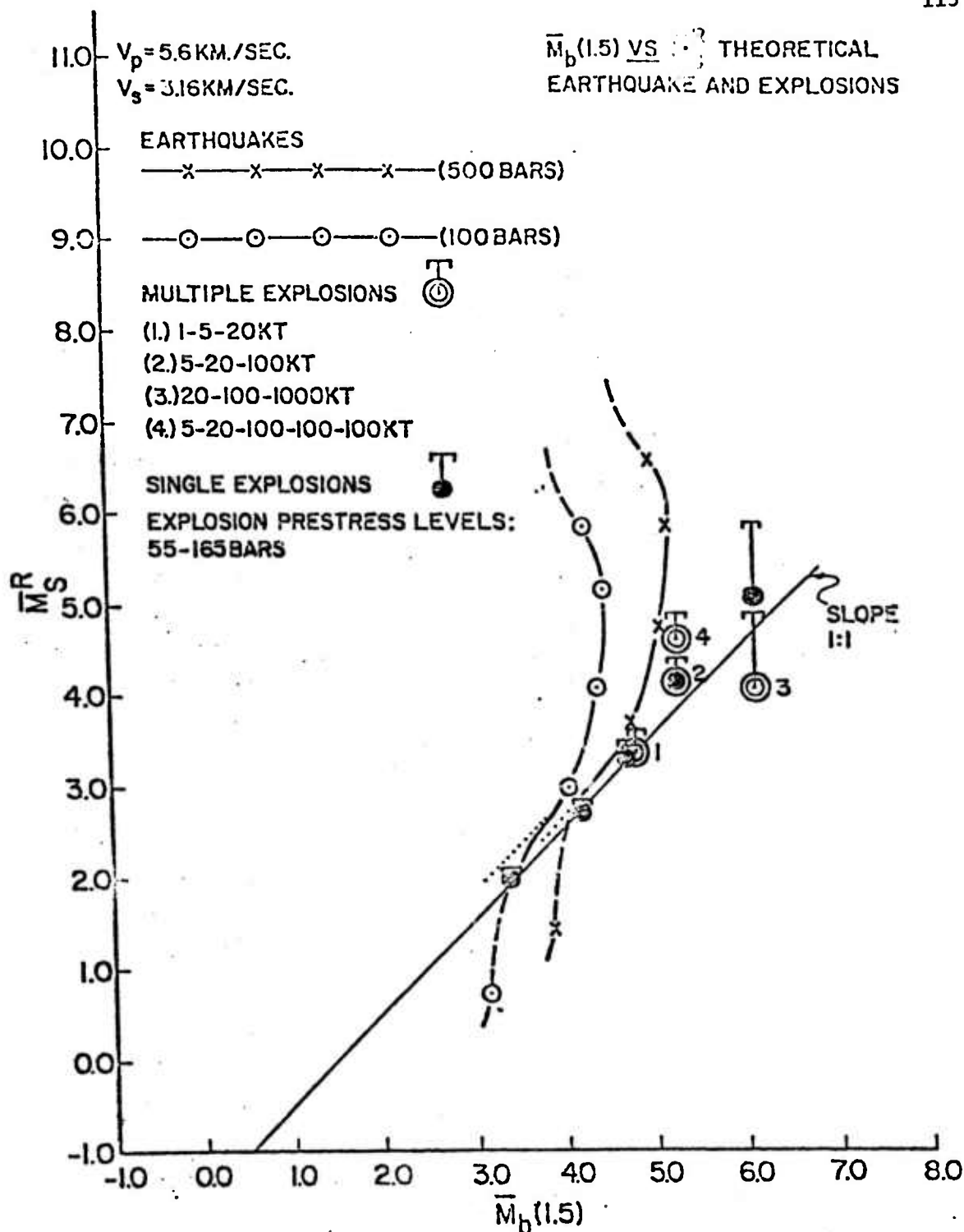


Figure 30. Rayleigh type spectral surface wave magnitude \bar{M}_s^R as a function of $\bar{m}_b(1.5)$, the frequency dependent spectral body wave magnitude at 1.5 Hz; for earthquakes, multiple explosions and single explosions. The effect of using $\bar{m}_b(1.5)$ rather than the spectral body wave magnitude at 1 Hz, which is simply denoted \bar{m}_b , is to shift the earthquake loci to lower body wave magnitude levels for the larger earthquakes and to increase the body wave magnitudes for the explosions slightly. The effect is to separate (Continued on the following page)

Figure 30 (Continued).

the earthquake and explosion populations in the $\overline{m}_b(1.5) - \overline{M}_s^R$ plane to a lower magnitude level than was the case for the $\overline{m}_b - \overline{M}_s^R$ plot. However the explosions are still close to the boundary of the earthquake population and positive identification on the sole basis of an $\overline{m}_b(1.5) - \overline{M}_s^R$ value could not be made at low magnitudes. Again the earthquake loci would be parallel to the unit slope line at low magnitude if R_s were large (dotted line on the plot) but drops below this line for the smallest earthquake because of the (worst case) choice of small R_s for the small event (dashed line on the plot).

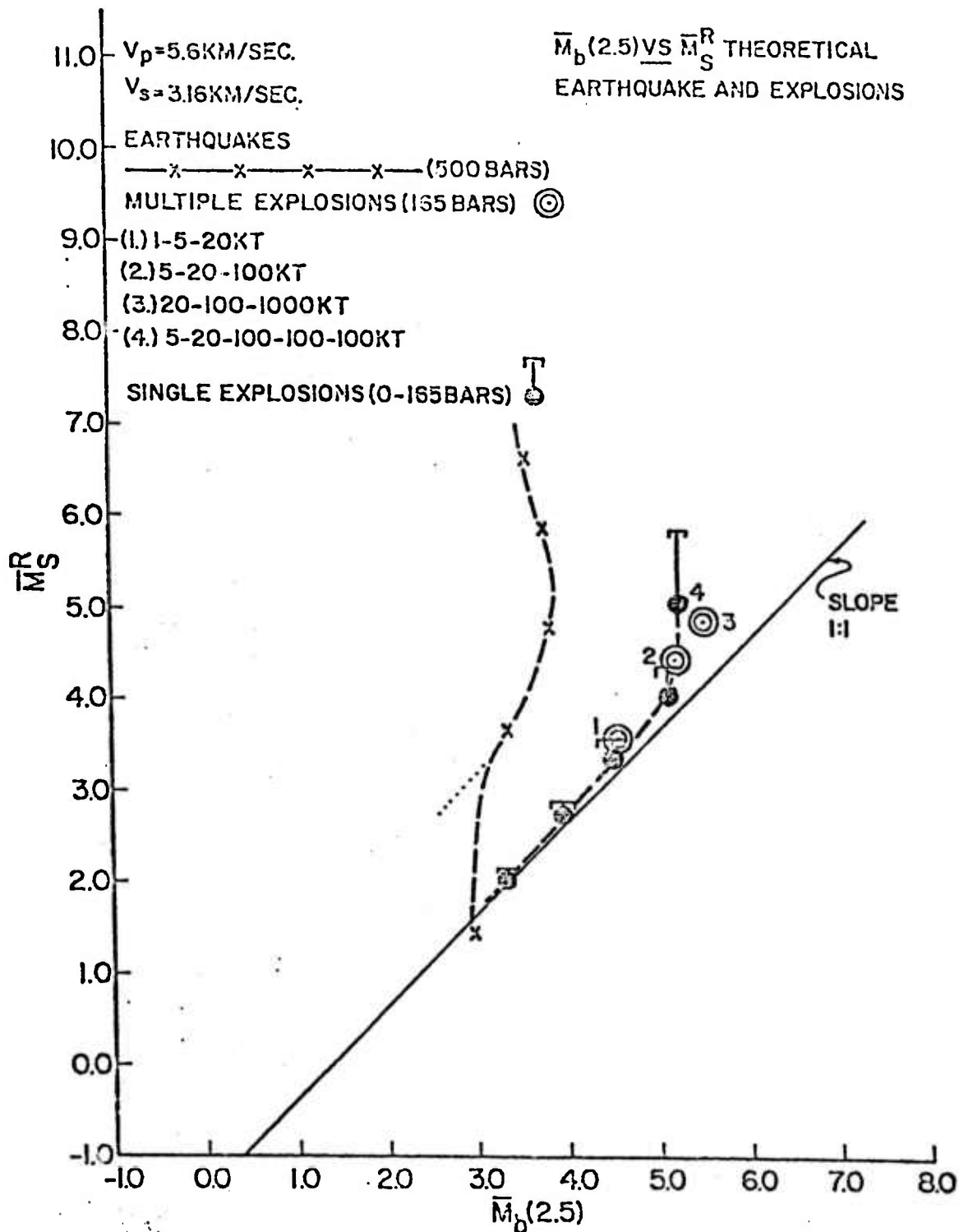


Figure 31. Rayleigh type spectral surface wave magnitude \bar{M}_S^R as a function of $\bar{m}_b(2.5)$, the frequency dependent spectral body wave magnitude at 2.5 Hz; for earthquakes, multiple explosions and single explosions. The possible convergence of the populations at $\bar{m}_b(2.5)$ magnitudes near 3.0 is due to the small R_s value used for the smallest earthquake considered (1 km fault). For a R_s value larger than 60 - 70 km, the $\bar{m}_b(2.5) - \bar{M}_S^R$ (Continued on the following page)

Figure 31 (Continued).

loci for the earthquakes would follow the dotted line shown on the plot and the earthquake and explosion populations would be widely separated at all magnitudes.

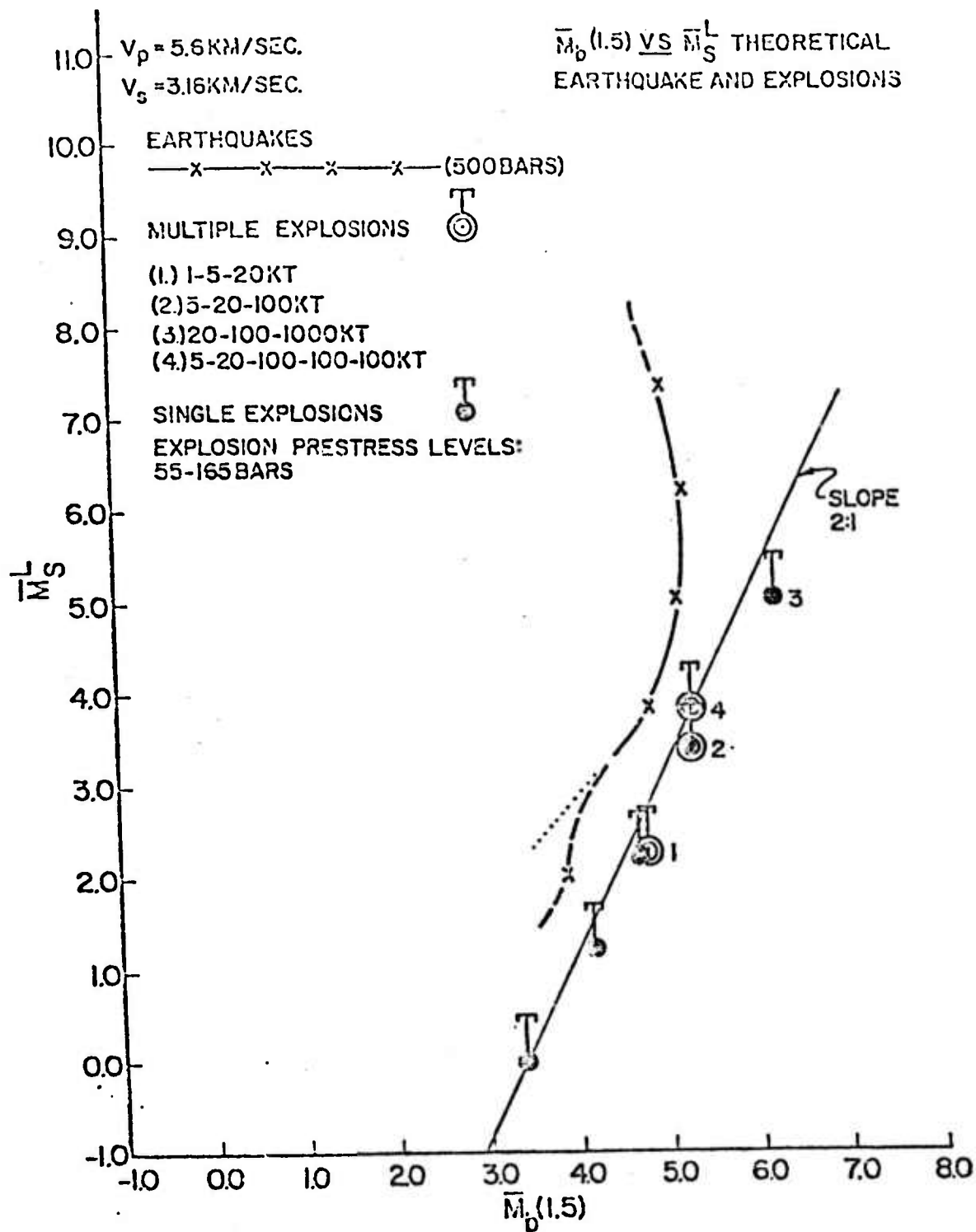


Figure 32. Love type spectral surface wave magnitude \bar{M}_S^L as a function of $\bar{m}_b(1.5)$, the frequency dependent spectral body wave magnitude at 1.5 Hz; for earthquakes, multiple explosions and single explosions. The body wave magnitude at 1.5 Hz for earthquakes is generally less than or about equal to that at 1 Hz, while the $\bar{m}_b(1.5)$ for explosions is greater than the magnitude at 1 Hz giving a wider separation of the (Continued on the following page)

Figure 32 (Continued).

earthquake and explosion populations. Both loci have a slope close to two for all low magnitudes since the Love surface wave magnitude is controlled by tectonic stress relaxation in both cases and in both cases the characteristic dimension of the high stress zone, R_s , is finite. For sufficiently large R_s , for small earthquakes, the earthquake population boundary line would follow the dotted line indicated, which has a slope of unity. In any case the earthquake and explosion populations are well separated and identification of the event types can be accomplished using $\overline{m}_b (1.5) - \overline{M}_s^L$ criteria.

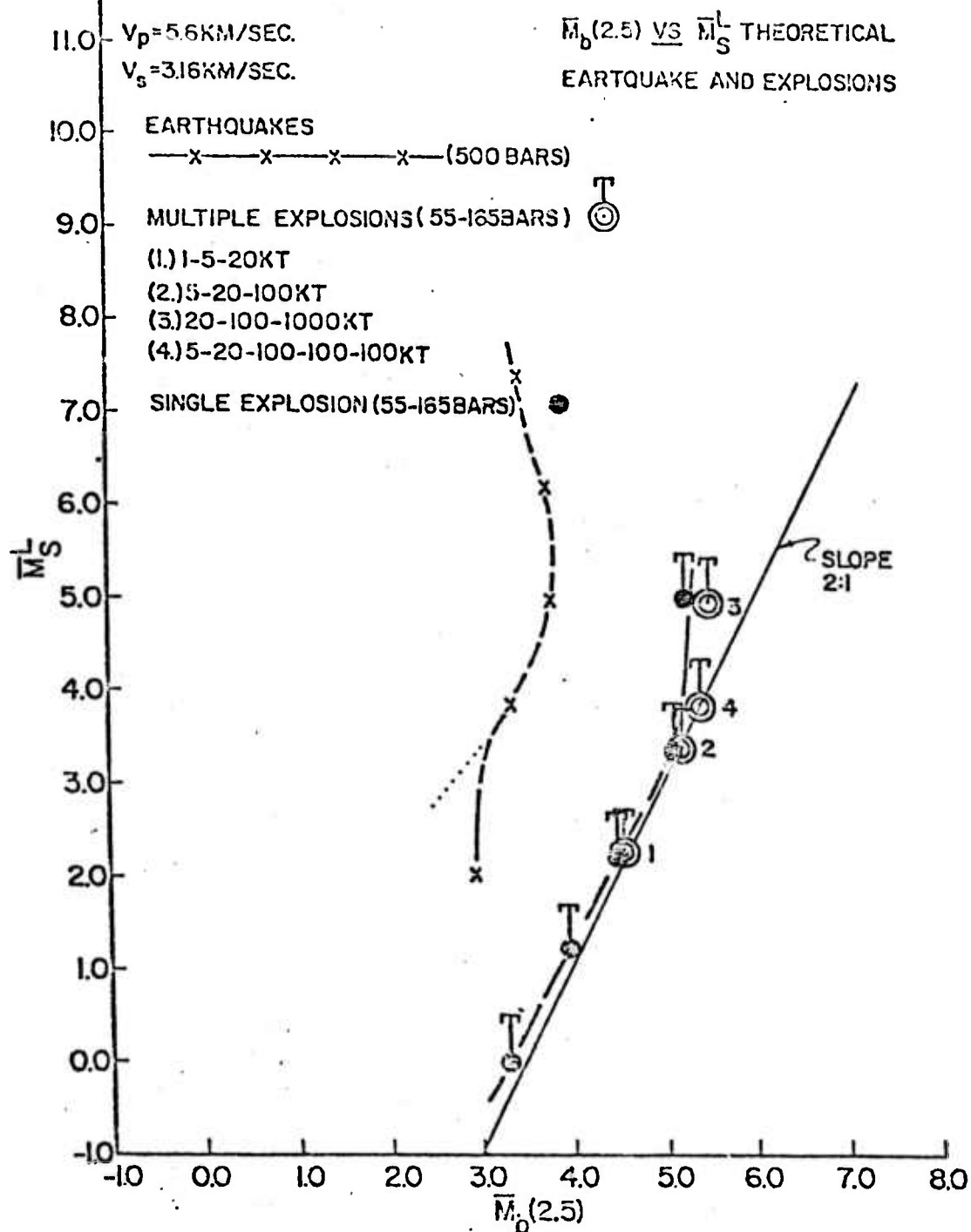


Figure 33. Love type spectral surface wave magnitude \bar{M}_s^L as a function of $\bar{m}_b(2.5)$, the frequency dependent spectral body wave magnitude at 2.5 Hz; for earthquakes, multiple explosions and single explosions. The $\bar{m}_b(2.5)$ magnitude is lower than the \bar{m}_b values at 1.0 and 1.5 Hz for earthquakes and for most explosions, but has decreased much more for earthquakes than for any of the explosions giving a very wide separation (Continued on the following page)

Figure 33 (Continued).
in the populations. The dotted line for the earthquakes indicates the effect of large R_s for small events. The $\bar{m}_b(2.5) - \bar{M}_s^L$ criteria would give positive event identification.

extent. For the $\overline{m}_b(f) - \overline{M}_S^L$ discriminate the effect of small R_S is not particularly critical, but it is somewhat more important for the $\overline{m}_b(f) - \overline{M}_S^R$ data. However, reasonable values of R_S set an upper limit to the reduction of \overline{M}_S^R (and \overline{M}_S^L) for earthquakes, and it would appear that even the smallest R_S values will not cause the populations to overlap at all in the $\overline{m}_b(f) - \overline{M}_S^L$ plane and only cause overlap for explosions at the smallest yields in the $\overline{m}_b(f) - \overline{M}_S^R$ plane.

We conclude from these results that strong positive identification of events can be achieved using either or both of the high frequency body wave magnitude versus surface wave magnitude criteria.

(c.) Short Period Body Wave Discrimination Using $\overline{m}_b(f)$.

For purposes of comparing the event populations in the $\overline{m}_b(f_1) - \overline{m}_b(f_2)$ plane, we take $f_1 = .3$ hz. This is an arbitrary choice, but it appears to be realistic in that it is the lowest frequency in the "short period body wave range" that is likely to be usable, since lower frequencies would be highly contaminated by the microseism noise peak at 6 sec period. However, depending on detector site characteristics, this choice can be modified, and so long as f_1 is fairly near .3 hz, the results of this section should be applicable more or less as they stand. We will, however, consider various values for f_2 in the high frequency range above 1 hz.

Figure (34) shows the event populations in the $\overline{m}_b(.3) - \overline{m}_b(1.5)$ plane. Separation of the event classes is by around one magnitude unit

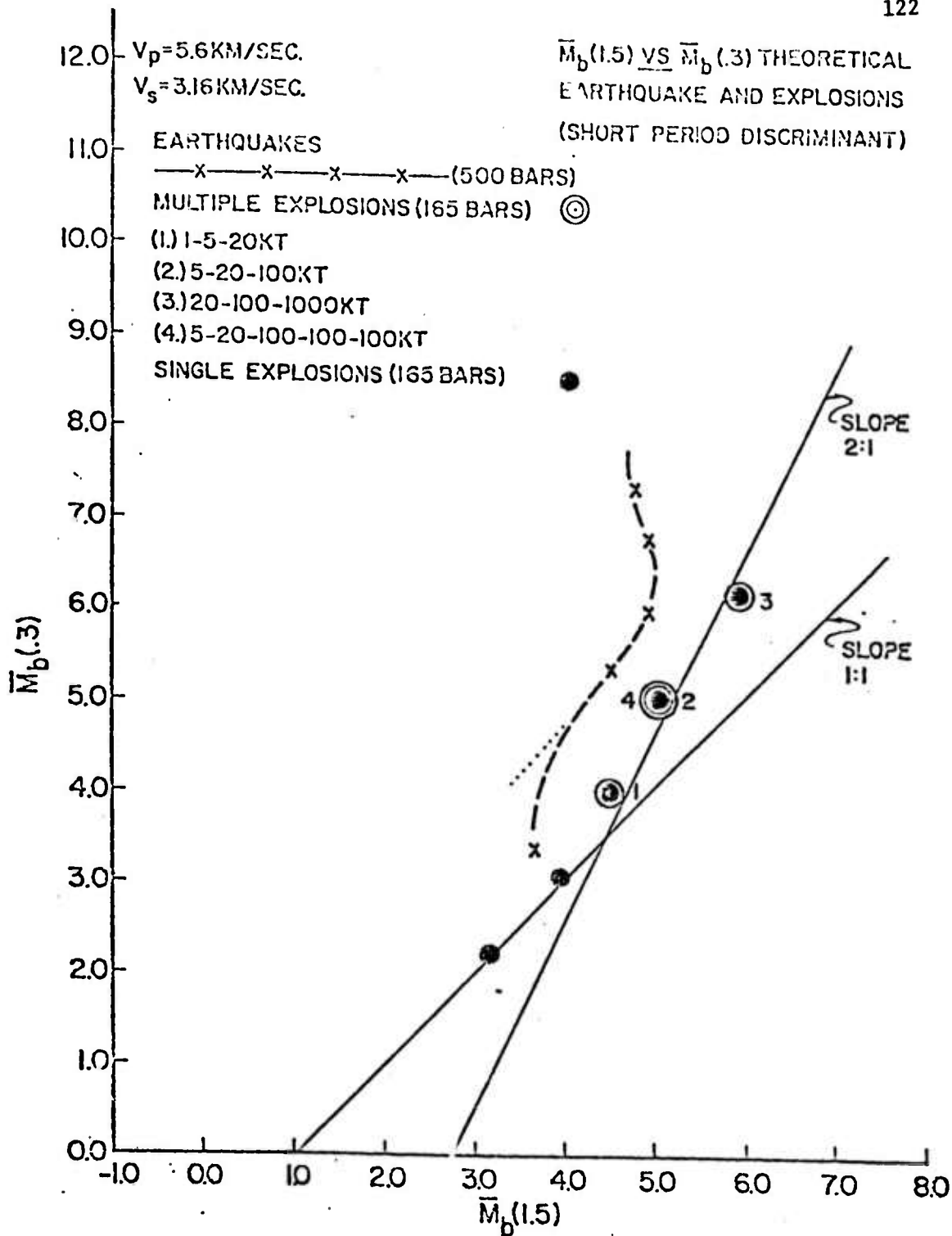


Figure 34. Low frequency spectral body wave magnitude, $\bar{m}_b(.3)$, as a function of the high frequency body wave magnitude, $\bar{m}_b(1.5)$; for earthquakes, multiple explosions and single explosions. This magnitude plot yields a short period event discrimination criteria using compressional body waves alone and hence is an easily applied and very powerful discrimination method. The separation of the populations is greater than (Continued on the following page)

Figure 34 (Continued).

a half a magnitude unit except possibly for the smallest events where the effect of a small R_s for small earthquakes can result in convergence of the populations for \bar{m}_b (1.5) values near 3.5. For sufficiently large R_s , the earthquake population boundary line would lie along the dotted line indicated and no convergence of the populations would occur.

for most of the range of event magnitudes, except for the smallest (~ 1 km) earthquakes. Here we see that a small R_S value will bring the populations closer together, but still with some reasonable separation. Of course if R_S is always large, then the populations are always well separated.

Figure (34) presents an interesting and practically important aspect of the $\bar{m}_b(f_1) - \bar{m}_b(f_2)$ discrimination criteria. That is, for some choices of the frequency $f_2 > 1$ hz, interference of P and pP for the explosion events in particular, can cause quite a large fluctuation in the position of the event population in the magnitude plane. Thus, since the P-pP interference introduces spectral minima and maxima at high frequencies, it can happen that the sampling of the spectrum, which is quite narrow in bandwidth, can occur at one of the spectra minima in the P-pP spectrum. When this occurs the $\bar{m}_b(f_2)$ will of course be depressed, and it is to be expected that this would occur more frequently for explosions than for earthquakes since they are always shallower than earthquakes and so, more subject to strong interference effects in the band $1.0 \leq f \leq 3.0$ hz. However, it is worth pointing out that spectral maxima can occur as well, for both earthquakes and explosions, and hence an "anomalous" increase in $\bar{m}_b(f_2)$ can occur for earthquakes at some particular f_2 , resulting in a shift of the earthquake population (or just one particular earthquake) toward or into the

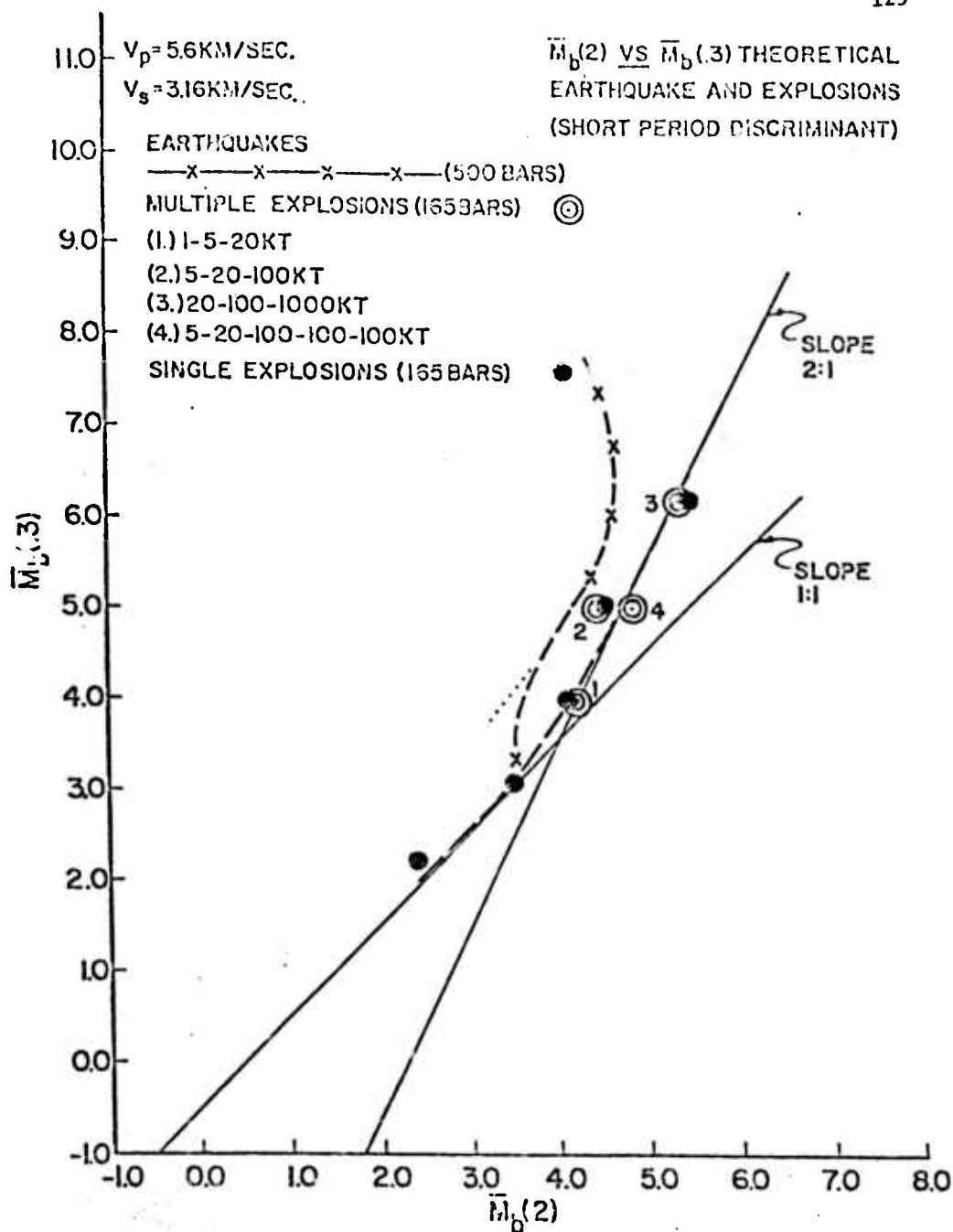


Figure 35. Low frequency spectral body wave magnitude, $\bar{m}_b(3)$, as a function of the high frequency body wave magnitude, $\bar{m}_b(2.0)$; for earthquakes, multiple explosions and single explosions. In this case the populations are not as widely separated as those in Figure 33 because, while the $\bar{m}_b(2.0)$ values decreased for both the earthquakes and the explosions, the explosion values decreased more than did those for the earthquakes and so brought the two populations somewhat closer together. The origin of the anomalous large decrease in $\bar{m}_b(2.0)$ for the explosions is the interference of the direct P wave and the pP reflected phase which, in this case, gives rise to

(Continued on the following page)

Figure 35 (Continued).

a hole or minimum in the P - pP spectrum near 2.0 Hz, so that the spectral body wave magnitude at this frequency is correspondingly depressed. Even so the populations are separated down to a \bar{m}_b (2.) value of 3.5. The convergence at low magnitude is again due to the use of a small R_s value for small earthquakes, the dotted curve shows the limit of the earthquake population for R_s large for these earthquakes.

explosion population. However while these effects (sampling of minima for explosions or maxima for earthquakes) can occur at some particular frequency f_2 , they cannot occur for a range of f_2 frequencies. Thus while the populations might converge somewhat for one choice of f_2 , they will diverge for other choices. Hence it is important to use several f_2 values and to identify events on the basis of their positions in all the $\bar{m}_b(f_1) - \bar{m}_b(f_2)$ plots. If an event is in the earthquake population in most cases, then it is almost certainly an earthquake, and conversely.

Even while the populations are close together in Figure (35), they are still reasonably well separated down to explosion yields of around 5 kT. The convergence there is due to the small R_S value taken for the $L = 1$ km earthquake, and of course this convergence is problematical--we have yet to verify that small R_S values apply for small earthquakes; if not, then the separation of populations is reasonably great at all levels.

Figures (36) and (37) show a very large separation in the earthquake and explosion populations for all events. Thus if signal frequencies as high as 2.5 and 3.0 hz can be reliably measured, without undue noise contamination, then very positive event identification can be achieved by this method. This implies that good event identification can be achieved by proper network design (i.e. sites where the high frequency noise is low and with detection

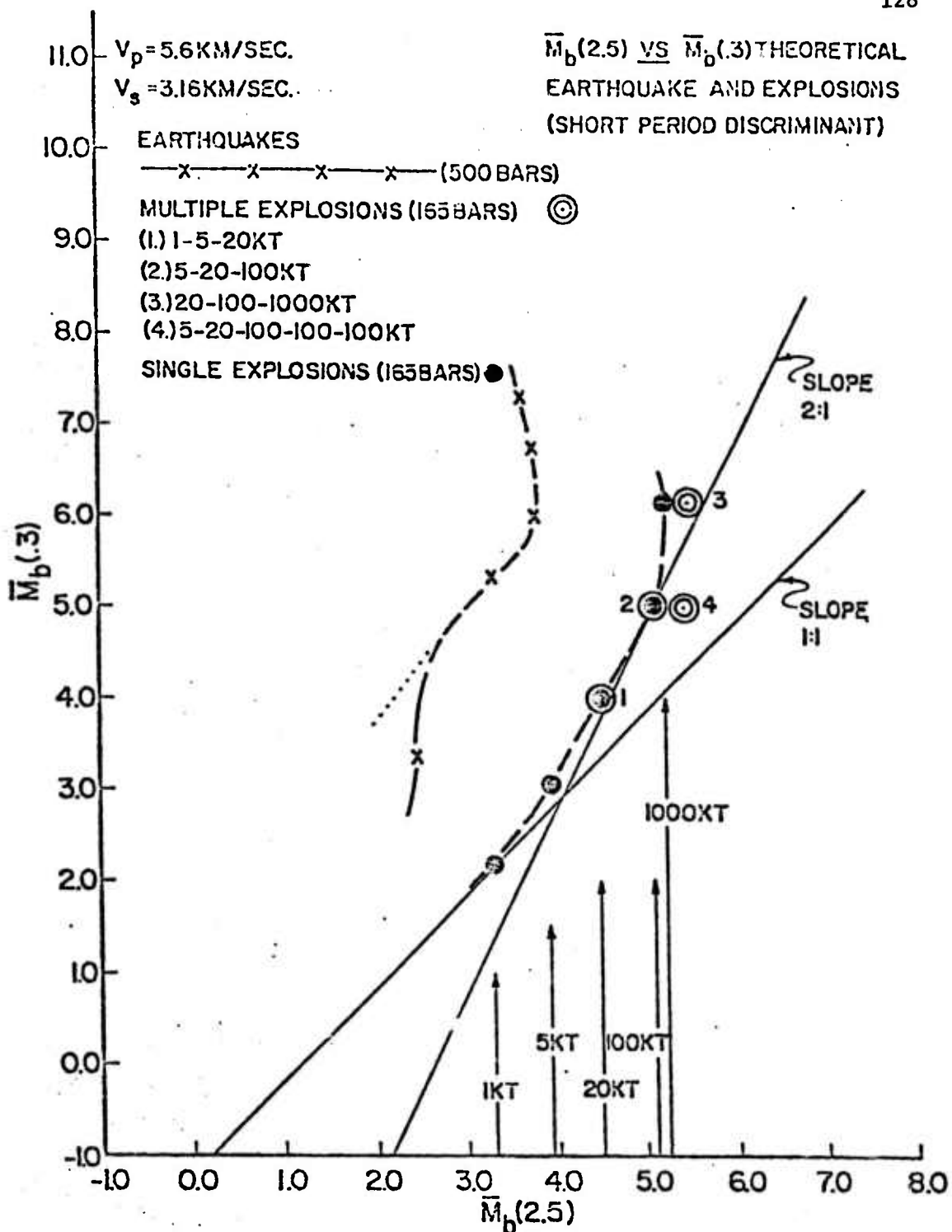


Figure 36. Low frequency spectral body wave magnitude, $\bar{m}_b (.3)$, as a function of the high frequency body wave magnitude, $\bar{m}_b (2.5)$; for earthquakes, multiple explosions and single explosions. The very large separation in populations is due to the difference in peak frequencies for earthquakes and explosions with the same $\bar{m}_b (.3)$ values. In general
(Continued on the following page)

Figure 36 (Continued).

the earthquake spectral peak occurs at a frequency considerably lower than 1.0 Hz while the explosion peak near 1.0 Hz or at higher frequencies. Consequently the $\bar{m}_b(2.5)$ is measured from the high frequency part of the earthquake spectrum where the spectral amplitude has decreased with a slope of 3 from the peak frequency and hence the amplitudes are low, while the $\bar{m}_b(2.5)$ for the explosions are measured near the peak in the spectrum. Therefore the earthquake $\bar{m}_b(2.5)$ values are very low while the explosion values are relatively very high. The separation of populations is everywhere larger than one magnitude unit. Further if the R_s value is large for small earthquakes than the earthquake population boundary is along the dotted line indicated, and an even larger separation of populations would prevail.

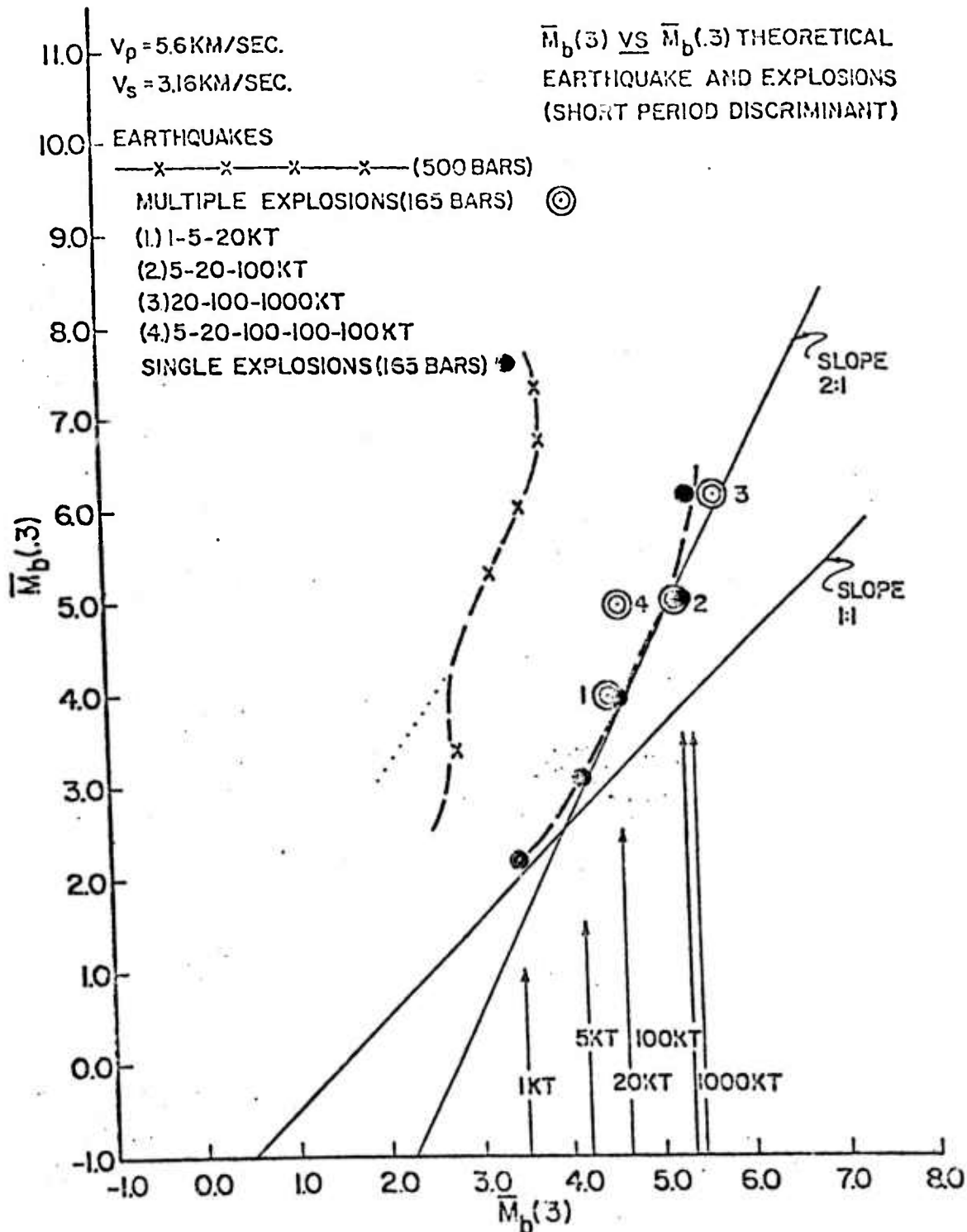


Figure 37. Low frequency spectral body wave magnitude, $\bar{m}_b(3)$, as a function of the high frequency body wave magnitude, $\bar{M}_b(3)$, for earthquakes, multiple explosions and single explosions. The earthquake and explosion populations separate by approximately one and a half magnitude units. The dotted line indicates the earthquake population boundary if R_s is large for small events. The large separation at all magnitudes is due to the spectral differences described in Figure 35.

locations at sites and distances where high frequency signal levels are reasonably high; such as in the interior of continental shield areas).

3. OBSERVATIONAL TESTING AND RESULTS FOR $\bar{m}_b(f)$ SPACE DISCRIMINATION.

The variable frequency magnitude discriminant, originally proposed by Archambeau, et al. (1974), is designed to exploit spectral differences between earthquakes and underground explosions. Essentially, the VFM technique consists of a comparison of a magnitude measurement $m_b(f_1)$ at a relatively low frequency (e.g., $f_1 = 0.45$ Hz) to a magnitude measurement $\bar{m}_b(f_2)$ at a higher frequency (e.g., $f_2 = 2.25$ Hz). The body wave magnitude \bar{m}_b is defined as the log of the amplitude of the output from a narrow-band (high Q) phaseless filter, centered at frequency f_c , plus a distance correction factor \bar{b} . That is

$$\bar{m}_b = \log_{10} \left[\frac{A_M}{T_C} \right] + \bar{b} ,$$

where the center period $T_C = 1/f_c$ and A_M is the maximum amplitude of the envelope of the filter output. The filters employed are digitally constructed in either the time domain (recursive) and/or frequency domain. The recursive filter is made phaseless by filtering an original time series in both the forward and backward time sense and summing the two results.

Examples of narrow-band recursive filter outputs for a presumed Eurasian explosion and a shallow earthquake recorded by the Oyer subarray in Norway are shown in Fig. 38. The top traces on the right- and left-hand sides of this figure correspond to the unfiltered best beam recordings of the P-wave trains, preceded by about 30 seconds of background noise, from the earthquake and presumed explosion, respectively. Note the enhancement of the high frequency ($f_c = 6.0$ Hz) filter output versus the low frequency ($f_c = 0.3$ Hz) filter output for the presumed explosion signal as compared to the filter outputs for the earthquake signal. The $\bar{m}_b(f_c)$ estimates for these events would be based on the maximum amplitudes of the envelopes of the filter outputs at the

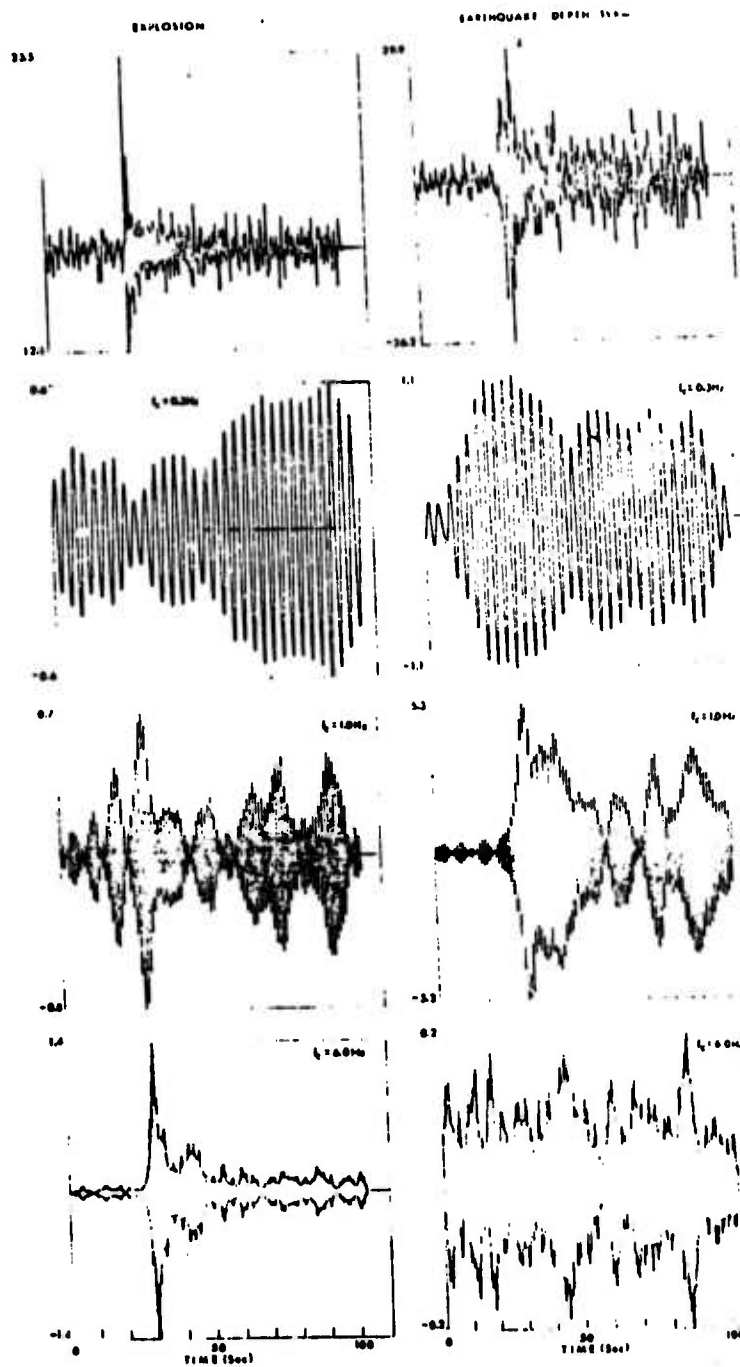


Figure 38. Examples of narrow band filter outputs at three center frequencies (0.3 Hz, 1.0 Hz and 6.0 Hz) for an explosion (left-hand side) and a shallow earthquake (right-hand side).

corresponding f_c 's. As an example, the \bar{m}_b (6.0 Hz) estimate for the presumed explosion would be based on the amplitude of the envelope of the $f_c = 6.0$ Hz filter output at about 30 seconds.

(a) SHALLOW EVENTS RECORDED AT LASA

The data base employed in the first test of the VFM discriminant consists of LASA short-period recordings of P-wave trains from 34 presumed explosions and 156 earthquakes (Lacoss, 1969). Thirty of the presumed explosions originated within the mainland USSR, two in Novaya Zemlya, one (Long-shot) in the Aleutians and one in the Sahara Desert. The earthquakes are distributed along the Alpide seismic belt, the Kuril-Kamchatka arc and the Arctic Ocean. The epicentral distances of these events range from 45° to about 100° with more than half of the events between 65° and 85° from LASA.

Figure 39 is a plot of spectral magnitude estimates, $\bar{m}_b(f_c)$, at a low frequency ($f_c = 0.45$ Hz) versus a high frequency ($f_c = 2.25$ Hz) for all 34 presumed explosions and those earthquakes in the data base that were reported in the Monthly Listings of Events, published by the USGS (formerly NOAA), as having shallow focal depths, $h < 70$ km. This figure clearly demonstrates the enriched high frequency content of the explosion body wave spectra as compared to the earthquake spectra. For instance, for a given value of \bar{m}_b (0.45 Hz) the explosions exhibit \bar{m}_b (2.25 Hz) values that are typically 0.6 to 1.0 unit larger than the \bar{m}_b (2.25 Hz) values for earthquakes.

The high degree of discrimination of earthquakes from explosions evident in Fig. 39 is especially significant in view of the non-regionalization of the event population. The variety of tectonic settings of this event population ranges from relatively stable shield regions to seismically active oceanic arc systems. An indication that discrimination could be further enhanced by regionalizing the event population comes from the fact that for \bar{m}_b (2.25 Hz) > 4.0 the two

presumed explosions (#35 and #138) plotting closest to the earthquake population occurred at Novaya Zemlya. Several of the earthquakes that plot closest to the explosion population occurred along the Kurile-Kamchatka arc or at locations far removed from the explosion epicenters.

The apparent bending of the explosion population into the earthquake population at \bar{m}_b (2.25 Hz) < 3.5 in Fig. 39 is mainly a result of microseismic noise inflating the low frequency ($f_c = 0.45$ Hz) magnitude estimates for the relatively small (signal-to-noise wise) explosions. In order to see the effects of noise contamination more clearly, magnitude estimates based on a series of low-frequency (0.3 to 0.6 Hz) narrow band filters versus the $f_c = 2.25$ Hz high frequency filter for a subset of the event population in Fig. 39 are shown in Fig. 40a-d. Note how the trends of the explosion population (x's) in the case of the low frequency ($f_c = 0.3$ and 0.4 Hz) filters, which are closest to the main concentration of noise power at LASA between about 0.1 to 0.3 Hz (Lacoss and Toksöz, 1967), exhibit rather abrupt bends near \bar{m}_b (2.25 Hz) = 5.0 and flatten out at \bar{m}_b (2.25 Hz) < 5.0. Examination of Fig. 4.3a-d indicates that the prevailing level and spectral distribution of microseismic noise at LASA sets gradually decreasing lower limits on the low-frequency magnitude estimates as the narrow band filter frequency increases from 0.3 Hz to 0.6 Hz, thereby moving away from the main noise band. In the case of Fig. 40d, for \bar{m}_b (0.6 Hz) versus \bar{m}_b (2.25 Hz), the trend of the explosion population is more nearly linear and parallel to the earthquake population over the entire magnitude range of the data. Noise contamination of the earthquake magnitude estimates in Fig. 40 a-d is obviously not as serious a problem since the earthquake signals for a given value of \bar{m}_b (2.25 Hz) are richer in low frequencies and show only a slight tendency to decrease in value as the filter frequency increases from 0.3 Hz to 0.6 Hz.

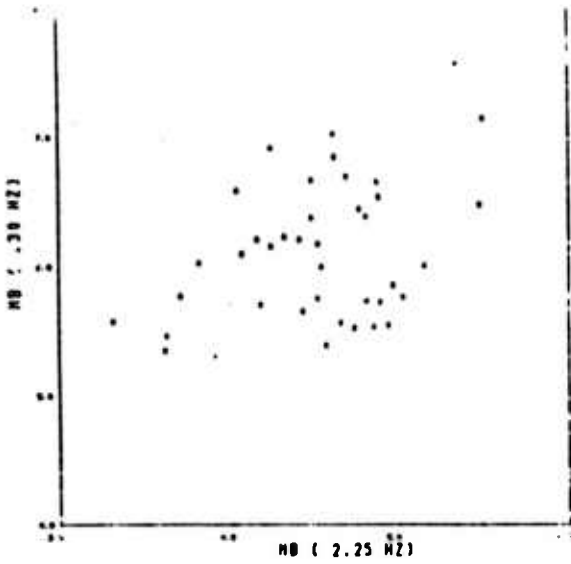


Fig. 40a

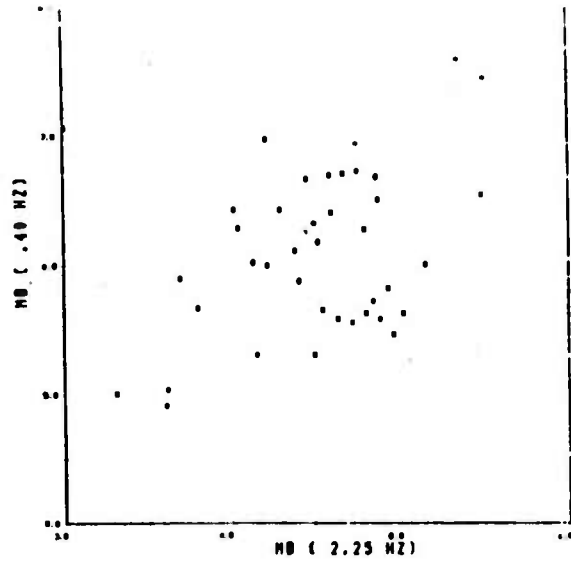


Fig. 40b

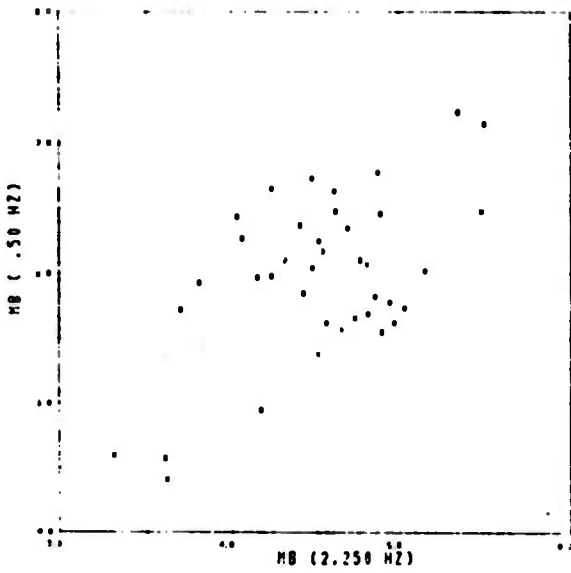


Fig. 40c

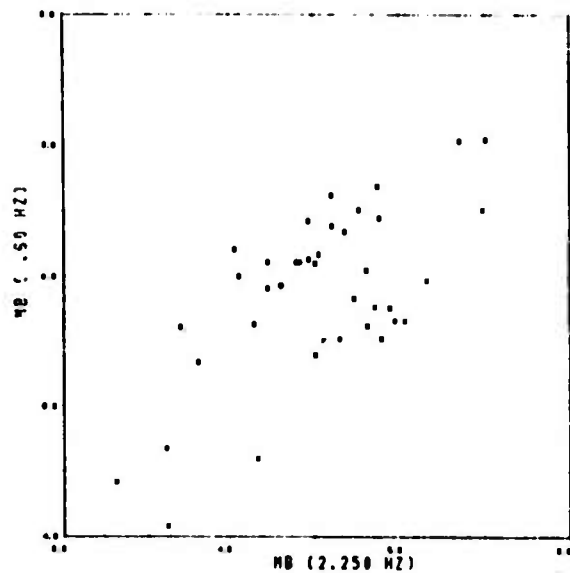


Fig. 40d

Figure 40. Spectral magnitude estimates for a subset of the LASA event population showing the effect of varying the f_c of the low frequency magnitude estimates.

On the high frequency end of the seismic bandpass it is the interplay of mainly three factors that limit the applicability of the VFM discriminant, as well as other short-period discriminants, to small magnitude teleseismic events recorded at LASA. These three factors are source spectrum, anelastic attenuation and high-frequency background noise at LASA. Definitive information on the source parameters of the earthquakes included in this data base are not available. However, the NOAA magnitudes of all the reported events are greater than $m_b = 4.7$. Thus, we will assume that the source spectra corner frequencies are less than 2.0 Hz and further that the source spectra are into the high frequency roll-off (ω^{-2} to ω^{-3}) for the high frequency range of interest here.

As is well known, for a fixed source-receiver distance, anelastic attenuation gives rise to an exponential decay with increasing frequency of the amplitudes of seismic waves. Thus the amplitudes of P-waves of frequency higher than 2.5 to 3 Hz from many of the events in the particular magnitude and distance range of interest here will be suppressed below the high frequency noise level at LASA.

The combined effect of these different factors on the magnitude estimates, \bar{m}_b , can be seen in Fig. 41 a-f. In each of these figures the low frequency magnitude estimates are computed at the same frequency, $f_c = 1.75$ Hz to 3.25 Hz. Starting with the $f_c = 1.75$ Hz estimates in Fig. 41a we see that the explosion and earthquake populations are not separated as much as in Fig. 39. This is undoubtedly due to the relatively close spacing of the high and low center frequencies, 0.5 Hz and 1.75 Hz. As the center frequency of the high frequency magnitude estimates increases (Fig. 41 b-d), the separation of the event population increases. Finally, as the center frequency is further increased (Figs. 41 c and f) the event populations begin to merge. The majority of

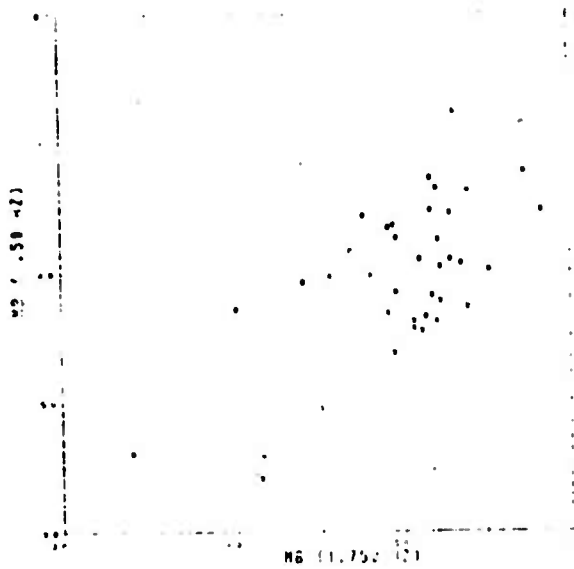


Fig. 41a

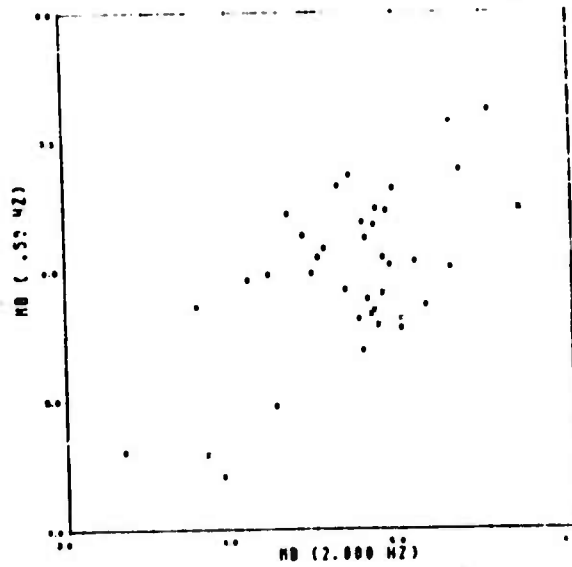


Fig. 41b

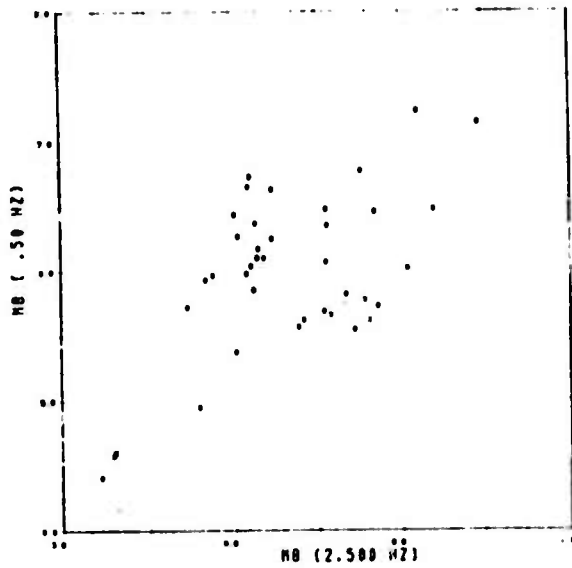


Fig. 41c

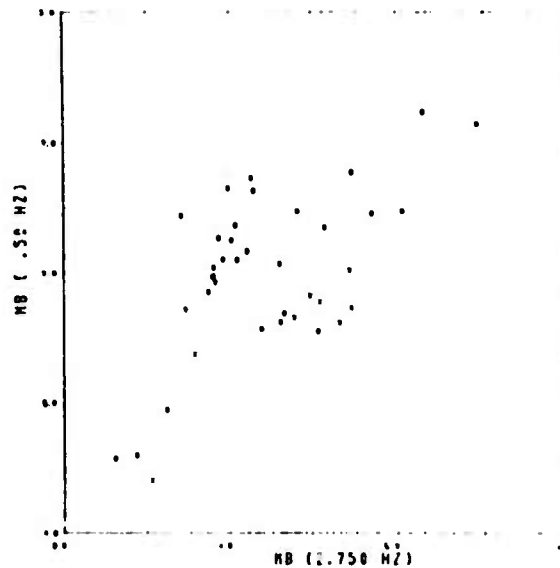


Fig. 41d

Figure 41. Spectral magnitude estimates for a subset of the LASA event population showing the effect of varying the f_c 's of the high frequency magnitude estimates.

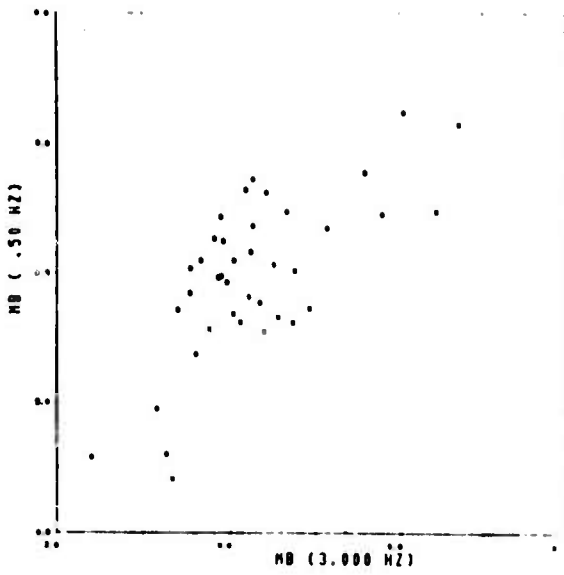


Fig. 41e

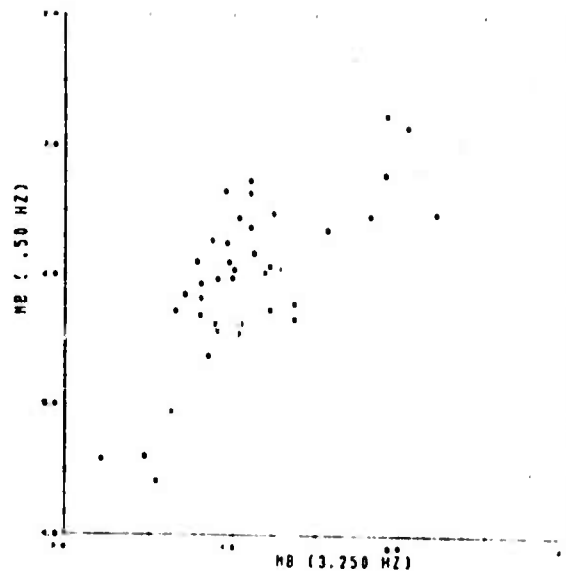


Fig. 41f

Figure 41 (Concluded)

earthquakes reach a high frequency lower noise limit of about $\bar{m}_b(f_c) = 4.0$ at $f_c = 2.5$ Hz while a comparable noise limit for the explosions is not reached until $f_c = 3.0$ Hz. Thus, while optimum discrimination would result for spectral magnitudes computed at frequencies (f_c) separated by a decade or more, noise and anelastic attenuation of the earth combine to constrain the useable bandwidth of frequencies in the case of the LASA data set to approximately one-half a decade.

(b) DEEP EVENTS RECORDED AT LASA

Twenty events in the depth range 80 km to 580 km are included in the LASA data base. Magnitude estimates for these events based on narrow band filter outputs at the same center frequencies as in Fig. 39 are plotted in Fig. 42 and compared with the shallow earthquake and explosion populations which are contoured by the dashed and solid lines, respectively. All of the events with focal depths $h > 300$ km occurred beneath the Japan and/or the Kurile-Kamchatka arcs. The epicentral locations of the intermediate depth events range from the Aegean Sea, Rumania, Hindu Kush regions to the Japan and Kurile-Kamchatka arcs.

Deep earthquakes often fail to separate from explosion populations when examined with any of the discriminants, short-and/or long-period, proposed to date. As can be seen in Fig. 42, such is the case for several of the deep events examined with the VFM technique. Suggestions as to the reason for the lack of discrimination of many deep events range from impulsive source-time functions, small source-dimensions, and high-Q propagation path to the receiver. While the behavior of the deep events in Fig. 42 cannot be explained at this time, it should be noted that the majority of intermediate depth events lie within the bounds of the shallow earthquake population.

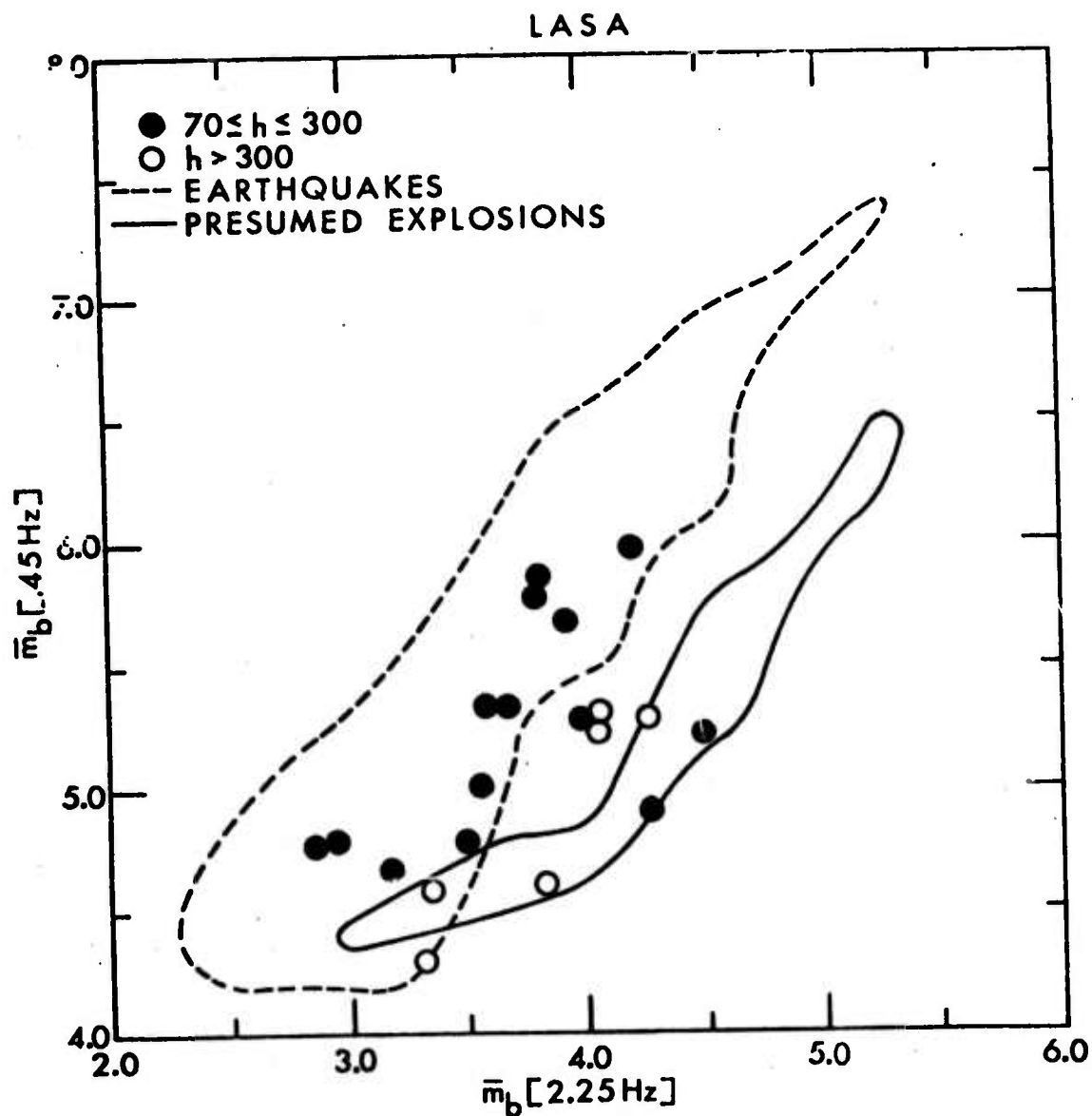


Figure 42. Spectral magnitude estimates of deep earthquakes recorded at LASA. The shallow earthquake and explosion populations plotted in Fig. 39 are contoured in this figure.

(c) SHALLOW EVENTS RECORDED AT NORWAY

A subset of the event population recorded at LASA was also recorded by the limited Oyer array in Norway. The spectral magnitude discriminant was applied to this smaller population of events and the results are presented in Figs. 43 and 44. In Fig. 43 spectral magnitudes, \bar{m}_b , at 0.6 Hz and 5.0 Hz are given for shallow earthquakes (open circles) and presumed explosions (closed circles). Analogous to the results at LASA in Fig. 44, there is discrimination of events over most of the magnitude range of the events except for the smallest magnitude explosion.

The arrows attached to the explosion points indicate that the low frequency magnitude, \bar{m}_b (0.6 Hz), is contaminated by noise. In Fig. 44 the output amplitudes from the narrow-band filters are corrected for noise and replotted. Comparing Figs. 43 and 44 it becomes clear that the cause of the bend in the explosion population toward the earthquake population at small magnitudes is the inflation of the low frequency explosion magnitudes by noise. Correction for this noise results in complete separation of the earthquake and explosion populations.

The effects of noise in different frequency bands can be seen in Fig. 45. In this figure the unfiltered time series corresponding to the smallest explosion recorded at Norway is plotted in the top left frame. The remaining frames show the effect on the time series of the application of five narrow band filters of increasing center frequency (0.3 Hz to 6.0 Hz). The gradual emergence of the signal at $f_c > 1.0$ Hz is quite striking. The persistence of a high signal-to-noise ratio for this very small event probably results from the high-Q nature of the propagation path.

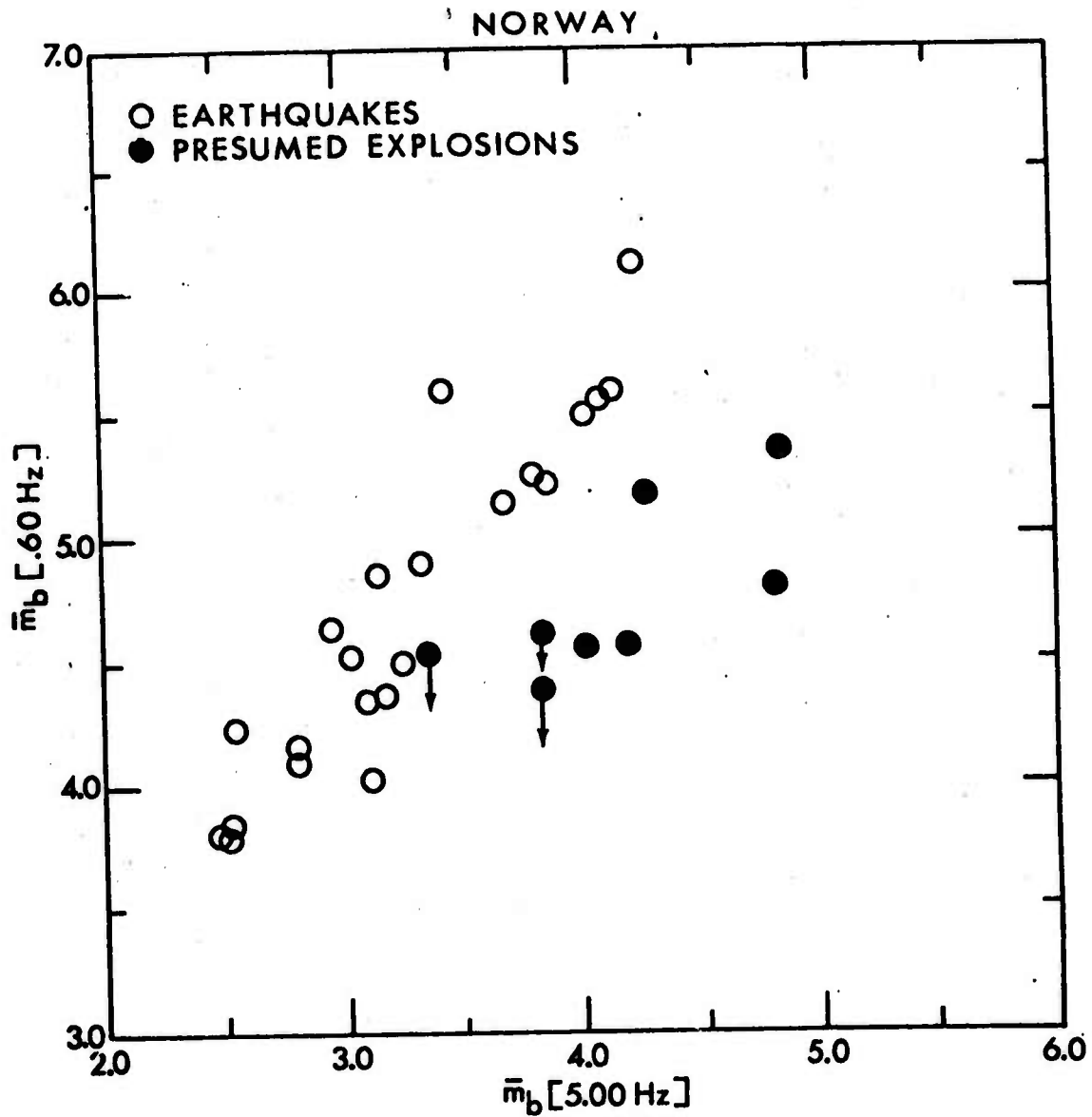


Figure 43. Spectral magnitude estimates at $f_c = 0.6 \text{ Hz}$ and $f_c = 5.0 \text{ Hz}$ for an event population recorded at the Oyer array in Norway.

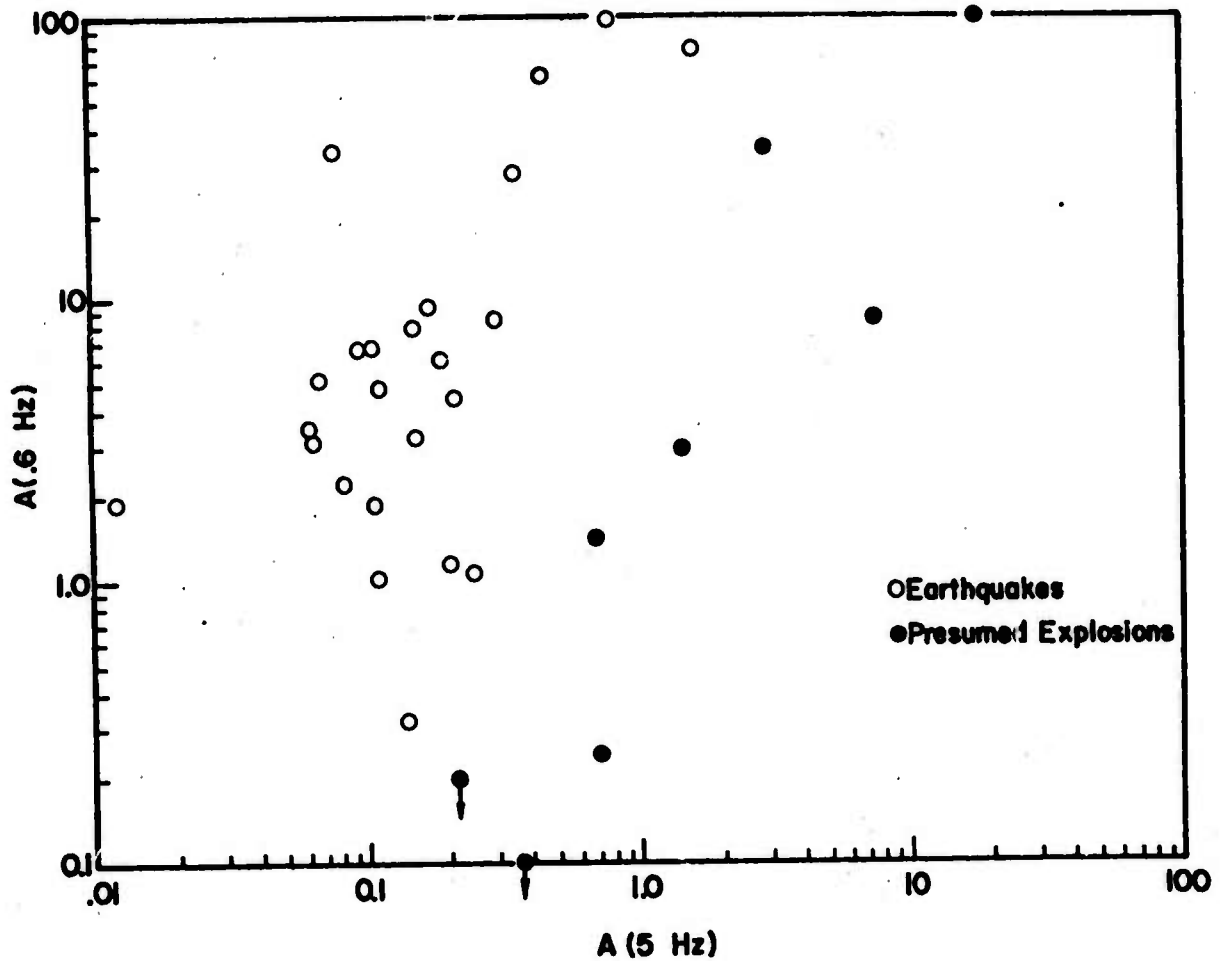


Figure 44 . Filter amplitudes (maximum) with noise corrections for the same event population plotted in Fig. 43. Note the enhanced separation of the earthquake and explosion populations.

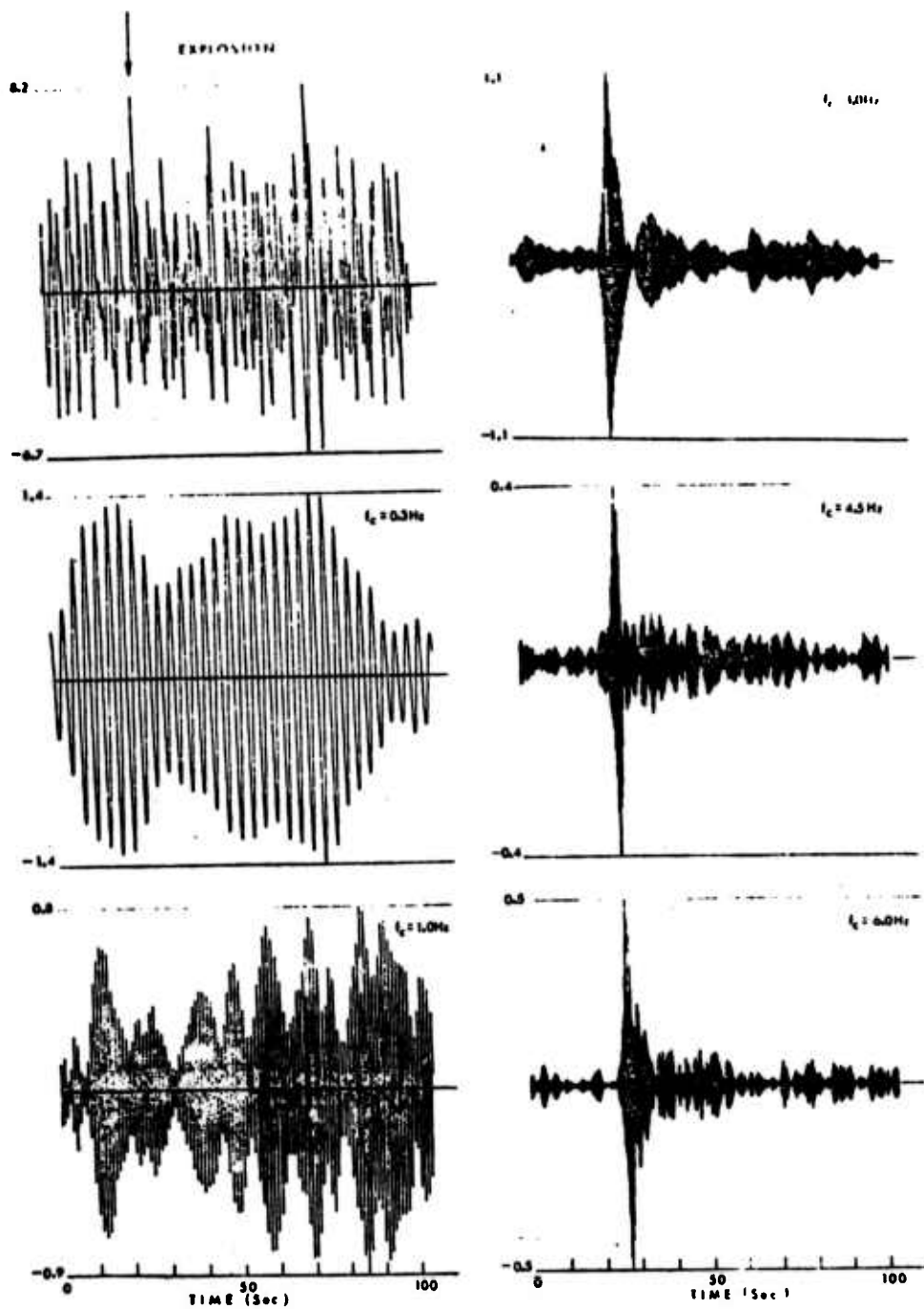


Figure 45 . Examples of increasing signal-to-noise ratio for a presumed explosion (top-left frame) recorded at Norway with successive application of high frequency narrow band filters. Arrow at top denotes approximate arrival of the explosion P-wave on the unfiltered trace.

(d) DEEP EVENTS RECORDED AT NORWAY

Eleven events in the Norway data base were assigned focal depths > 70 km. Amplitudes of narrow-band filter outputs with the same f_c 's used in Figs. 44 and 45 were computed for these eleven events and are plotted in Fig. 46. The frequency dependent amplitudes were corrected for noise based on measurements taken before the onset of each event P-wave signal. The bounds of the shallow earthquake and explosion populations plotted in Figs. 44 and 45 are indicated in Fig. 46 by the broken and dashed curves, respectively.

As was the case with the deep events in the LASA data set shown previously in Fig. 42, the deep events recorded at Norway (Fig. 46) exhibit considerable scatter without any obvious pattern of behavior. While several of these deep earthquakes fail to discriminate in this figure they are really not as troublesome as they might seem since these events can often be identified as naturally occurring earthquakes on the basis of other information (e.g., hypocentral location using P, pP and/or sP travel times).

A rather dramatic example of the short-period spectral similarities between an explosion and a deep earthquake is shown in Fig. 47. Approximately 80 seconds of an unfiltered explosion time series and the output amplitudes of three narrow band filters ($f_c = 0.3$ Hz, 1.0 Hz and 6.0 Hz) applied to the time series are shown on the left-hand side of this figure. A similar sequence of pictures is shown on the right-hand side for a deep ($h = 115$ km) earthquake. Note how the signal-to-noise ratio of the narrow band filter outputs for both events increases as the center frequencies of the filters increase from 0.3 Hz to 6 Hz. Comparison of the spectral behavior of the deep earthquake in this figure with the shallow earthquake ($h = 35$ km) shown in Fig. 38 clearly

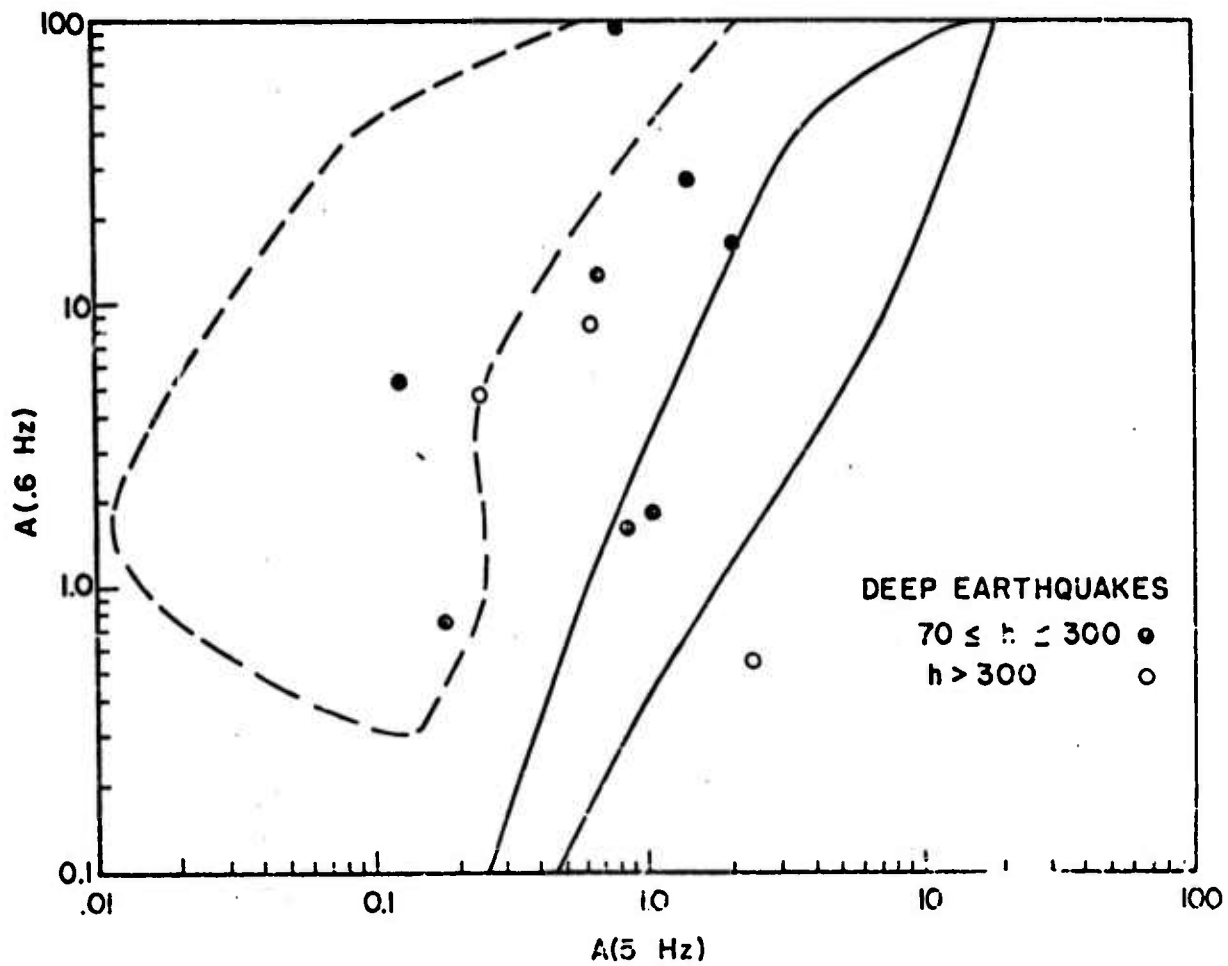


Figure 46. Amplitudes of narrow band filter outputs at two different frequencies for deep earthquakes recorded at Norway.

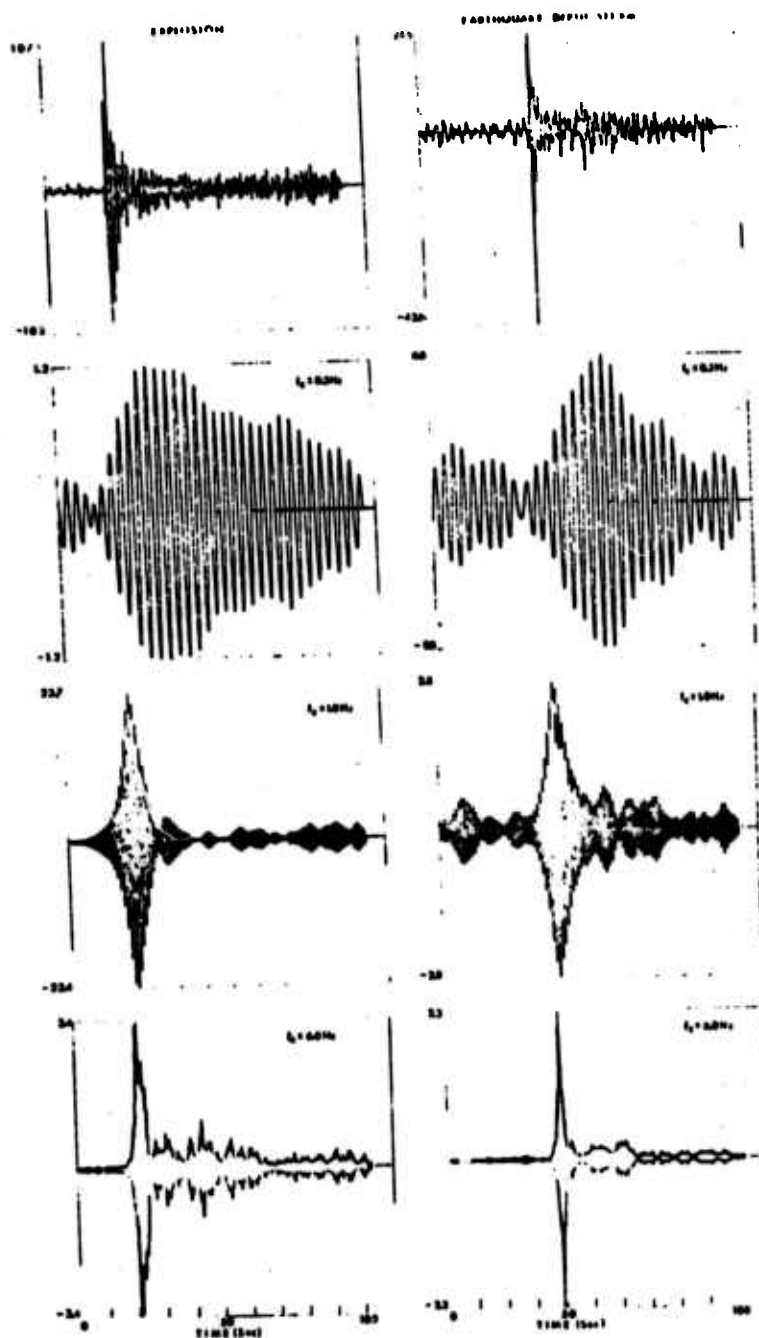


Figure 47. Narrow band filter outputs at three different center frequencies ($f_c = 0.3$ Hz, 1.0 Hz and 6.0 Hz) for an explosion (left-hand side) and a deep earthquake (right-hand side).

points out the far field spectral differences between these two types of events.

(e) MULTIPLE EXPLOSION SCENARIO

The spectral magnitude technique is especially suited for identification and discrimination of multiple explosion sequences that are designed to appear earthquake-like in terms of conventional (M_s - m_b , depth of focus, complexity, first motion) discriminants. A multiple event scenario, somewhat similar to one proposed by Kolar and Pruvost (1975), was devised by superposing eight scaled seismograms of a presumed Kazakh explosion recorded at LASA. This explosion signature is shown on the bottom-center in Fig. 48.

The array of explosions and their relative yields were designed to produce earthquake-like seismograms over a wide range of azimuths. The particular array configuration (spacing and firing order) is indicated in the center of Fig. 48. Each seismogram comprising the multiple event was delayed in time relative to the first, and scaled in amplitude. The largest explosion in the scenario is the sixth event and is scaled to give the same teleseismic ground motion as the primary signal. The amplitude scaling for all eight explosions in the scenario was 1, 3.1, 5, 10, 10, 20, 15 and 12.5.

The composite seismograms resulting from the scenario are shown in Fig. 48 at five different azimuths (1-5) with respect to the shot array. The first point to be noted about these composite seismograms is that with the addition of noise to the beginning of each seismogram the first motions at azimuths 1, 3 and 5 would most probably be picked as rarefactions. Secondly, the complexity of each composite signal has been greatly increased over that of the primary signal.

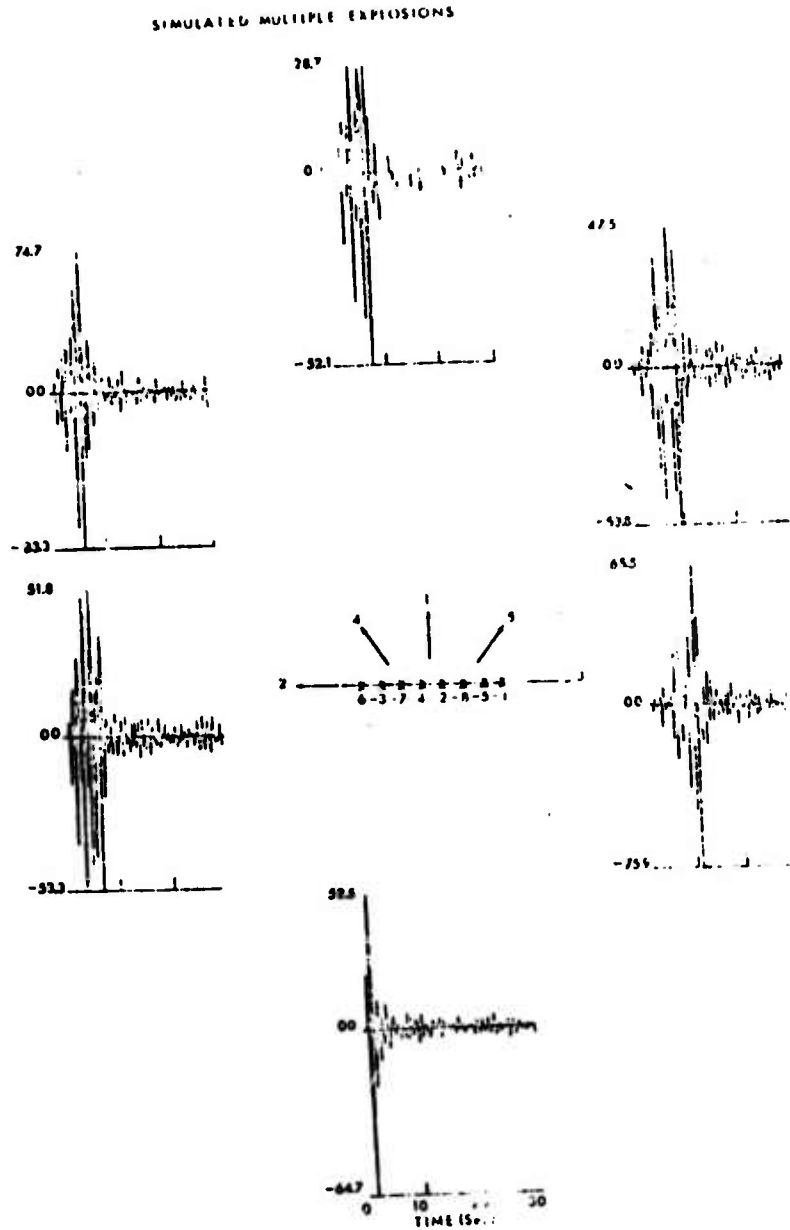


Figure 48. Primary explosion signature (bottom-center) used to make composite seismograms at five different azimuths from the array of eight explosions. The firing order and spacing of the explosions are indicated in the center.

Two factors work together to make the multiple event scenario appear earthquake-like on an M_s - m_b basis. First an analyst making amplitude measurements, to be used for m_b determinations in the conventional manner (maximum amplitude within the first 3 or 4 cycles) would undoubtedly pick amplitudes corresponding to the earlier smaller explosions in the sequence. On the other hand the M_s measurements would be mainly based on the superposed surface waves from the three large yield explosions occurring late in the sequence. The net result would be a reduced m_b and an enhanced M_s resulting in the scenario moving into the earthquake population on an M_s - m_b plot.

Application of the spectral magnitude technique, however, results in complete discrimination of the multiple explosion scenario. In Fig. 49 the spectral magnitude estimates, computed for the five azimuths indicated in Fig. 48 are indicated by the x's. A most significant result in Fig. 49 is that the spectral magnitude estimates of the multiple explosion sequence cluster around the estimates of the primary signal used in the construction of the scenario (the closed circle immediately to the right of x-1). This means that the VFM technique has based the magnitude estimates on the largest amplitude arrival in the wavetrain, corresponding to the largest yield explosion in the sequence. This is a very important result for yield determination of both single and multiple explosions.

(f) SUMMARY

A variable frequency magnitude technique designed to exploit spectral differences between earthquakes and explosions was developed and applied to a large population of Eurasian events recorded at LASA and a limited array (Oyer) in Norway. The magnitude estimates are based on the output amplitudes of variable frequency narrow band phaseless filters

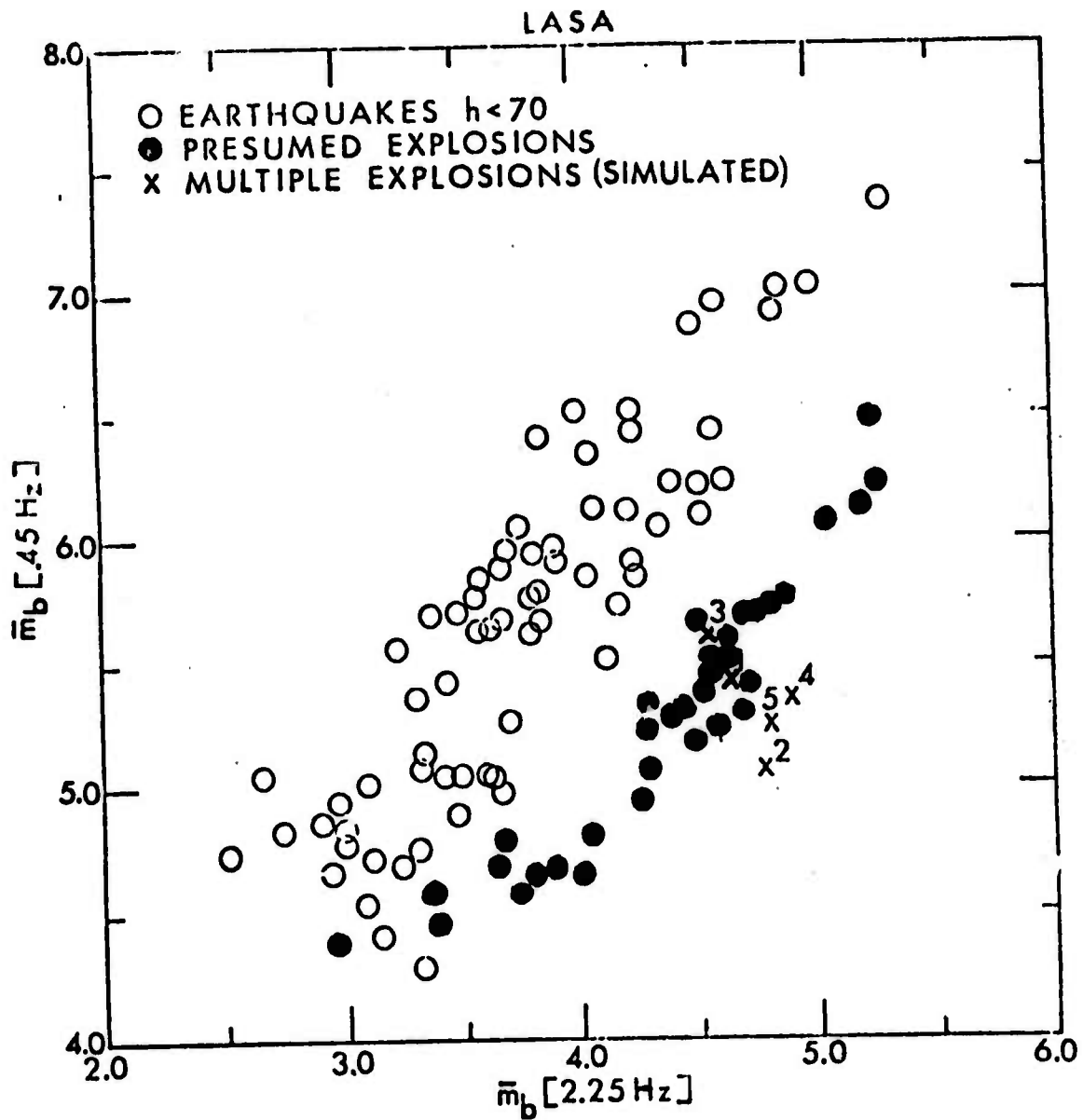


Figure 49. Spectral magnitudes for same event population and filter parameters as in Fig. 39 with estimates for multiple explosions (x's) showing complete discrimination.

applied to short period recordings of body waves. The most significant results pertaining to event identification, discrimination and yield determination obtained with this discriminant are the following:

1. Complete and positive discrimination of earthquakes and explosions down to explosion magnitudes of LASA $m_b = 4.2$.
2. Multi-azimuth discrimination of a multiple explosion scenario with the correct identification of the largest yield explosion in the scenario.
3. Simultaneous discrimination at a single recording site of events, both earthquakes and explosions, distributed over a wide geographical region.

IV. Earthquake Source Properties: Tectonic Stress Estimates

A principal objective of the research effort has been to determine non-hydrostatic stress levels at depths in the earth. As has been previously explained, the approach is to use the large m_b - M_s data base along with theoretical predictions of m_b and M_s for earthquakes, in order to determine the nonhydrostatic stress. Some examples of the results of this study are shown in this part of the report and the discussion will be largely preliminary, since considerable work is still in progress.

Figure 50 shows the m_b - M_s observations for Seismic Region 1, the Aleutian region, along with the theoretical curves obtained for earthquake source models with variable prestress levels. It should be mentioned again that the stress values shown are prestress levels if transient melting is involved for the observed earthquakes, since that condition was assumed in the models, while the stress values correspond to stress drops if this condition is not met. Further the theoretical events used were all dip slip (or thrust) events at 10 km depth. The earth structure model used is appropriate to tectonic regions. The theoretical m_b - M_s curves were then obtained from synthetically produced seismograms.

From the distribution of the m_b - M_s data shown in this figure, it is clear that the average earthquake in this region has a prestress (or stress drop) of about 100 to 150 bars. However, numerous events show prestress (and/or stress drop) levels of about 1.0 kbar, with some events having apparent prestress levels near 1.5 kbar. However of this latter group, it is possible that the observed M_s values are somewhat low because the events were rather deep. In any case however it is clear that earthquakes with associated prestress levels around 1 kbar are not uncommon in this region. Further it is clear that a very wide range of stress drop or prestress level is characteristic. Indeed the stress levels range from below 10 bars to about 1000 bars.

The earthquakes with apparent very low prestress levels are probably strike slip events with artificially low m_b values due to the event radiation pattern with respect to the receiver distribution. The two events near the "NTS Explosion" line with high m_b values relative to their M_s values are actually explosions.

The distribution of m_b - M_s points shown in Figure 50 are rather typical of distributions for some of the other seismic regions. These regions appear to be

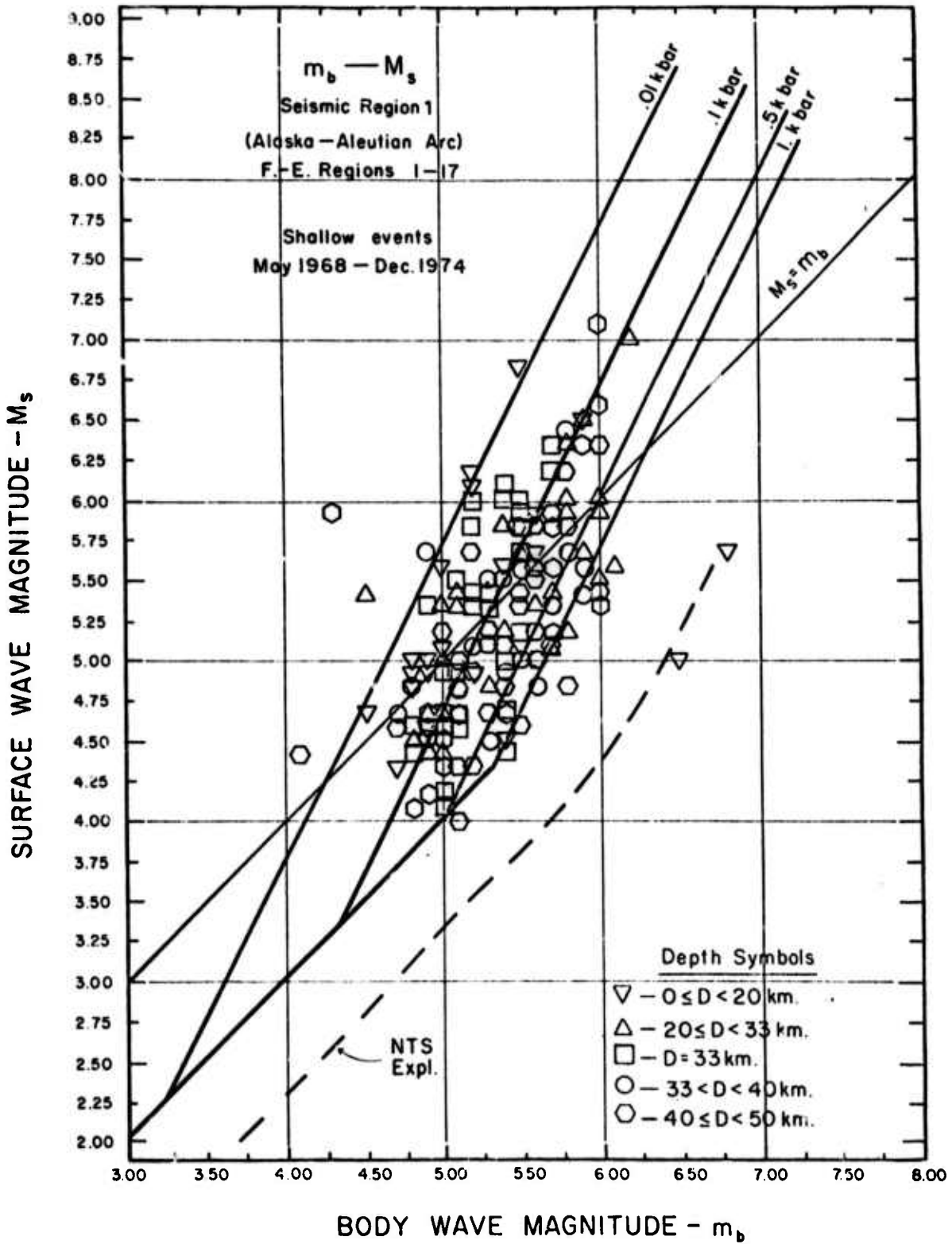


Figure 50. $m_b - M_s$ event data for Seismic Region 1, Alaska-Aleutian Arc.

zones of high tectonic stress as evidenced by the occurrence of numerous high stress drop events.

Figure 51 shows a region with most events having prestress values near 100 bars. However there are still a few events with very high and very low stress values. This seems to be typical of most seismic regions, but in some regions there appear to be more of such "anomalous" events than in others and further the mean value of the event stresses for these regions is also somewhat variable in a compatible sense. That is, regions with very few very high stress events also have a population distribution peaked at a lower stress than does the population with numerous high stress events. Hence there appears to be a clustering effect, with events tending to cluster on one side or the other of the 100 bar stress line for different seismic regions.

Figure 52 illustrates Seismic Region 3, the California-Nevada region. The event points near the "NTS" line are explosions. This figure shows more small events than did the previous figures (due to the receiver distribution). It is important to observe that the line of unit slope along which the "stress drop lines" terminate is determined by the R_s factor used. For the theoretical curves shown in these figures a large R_s factor were used, such that the M_s value was not affected.

If the stress concentration for at least some small earthquakes is small (less than about 60 km), then we should expect to see event points falling below this line in the m_b - M_s plane. From the data shown in Figure 52 it is not clear whether there is any significant drop in event data below this line. However, if an event did drop appreciably below this line, for whatever reason, it would most likely not be included in this data set, since the events represented are only those for which reasonably good measurements of both m_b and M_s could be made. If the long period surface waves were of low amplitude it is likely that the M_s value would be highly uncertain if not unmeasurable. Thus such an event would not normally be included in the data set.

Figures 53 through 57 illustrate the m_b - M_s populations for a number of other seismic regions. It is quite evident that the normal spread in the event stress values is from approximately 10 bars to 1000 bars. Further it appears that there are events with m_b - M_s values below the " R_x line". However, it is quite likely that these events could have been quite deep, since the reported

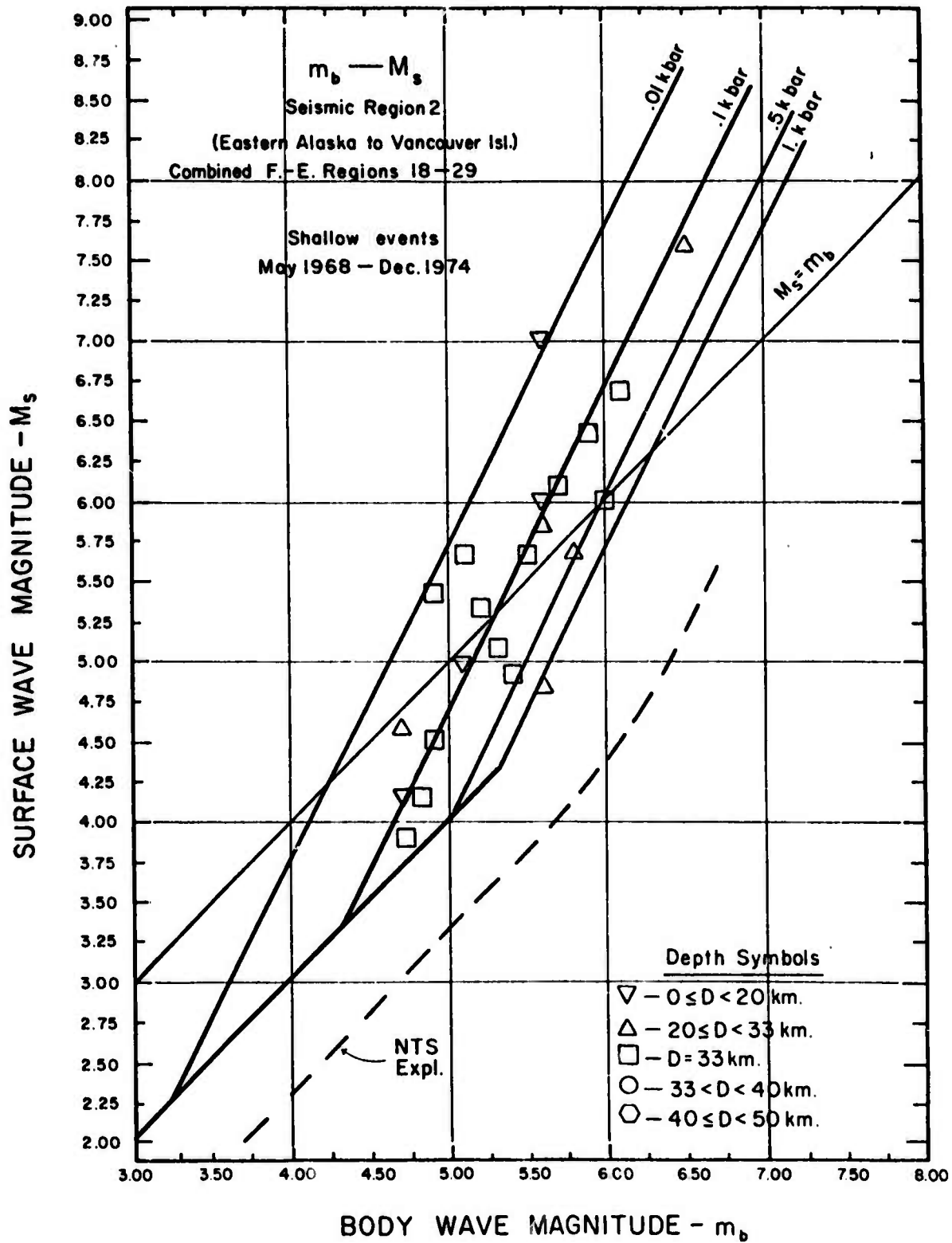


Figure 51. $m_b - M_s$ event data for Seismic Region 2, Eastern Alaska to Vancouver Island

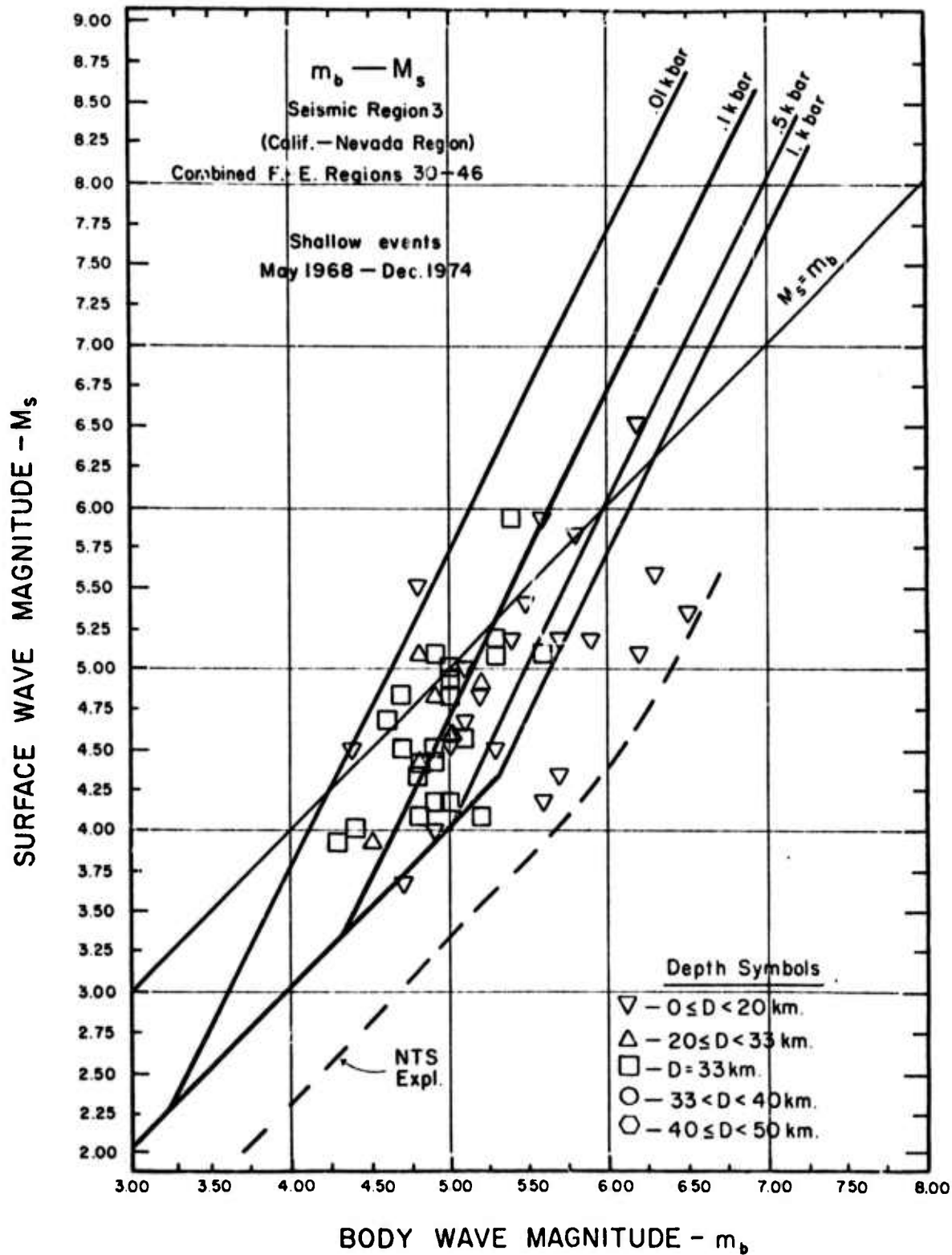


Figure 52. $m_b - M_s$ event data for Seismic Region 3, California-Nevada region.

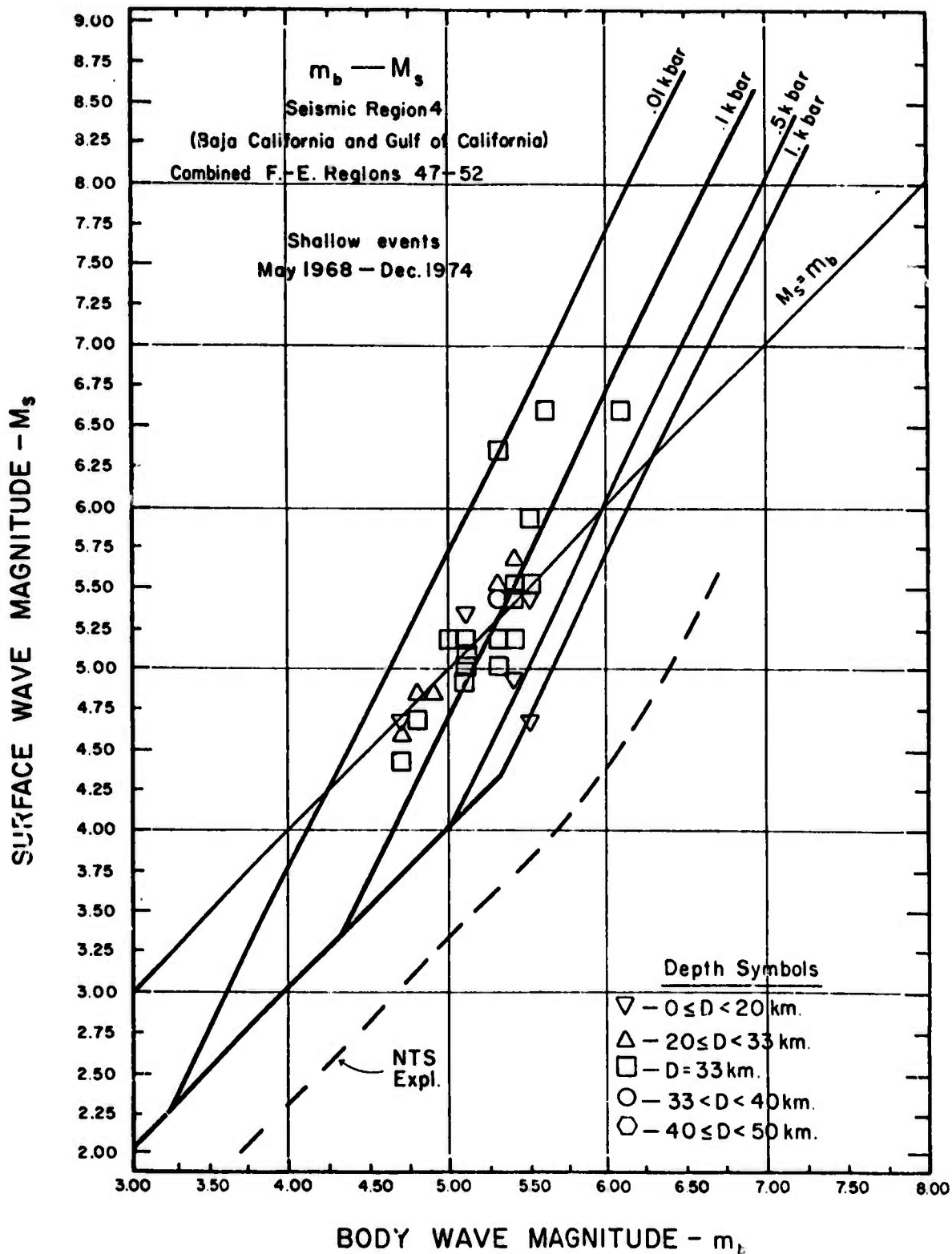


Figure 53. $m_b - M_s$ event data for Seismic Region 4, Baja California and Gulf of Mexico.

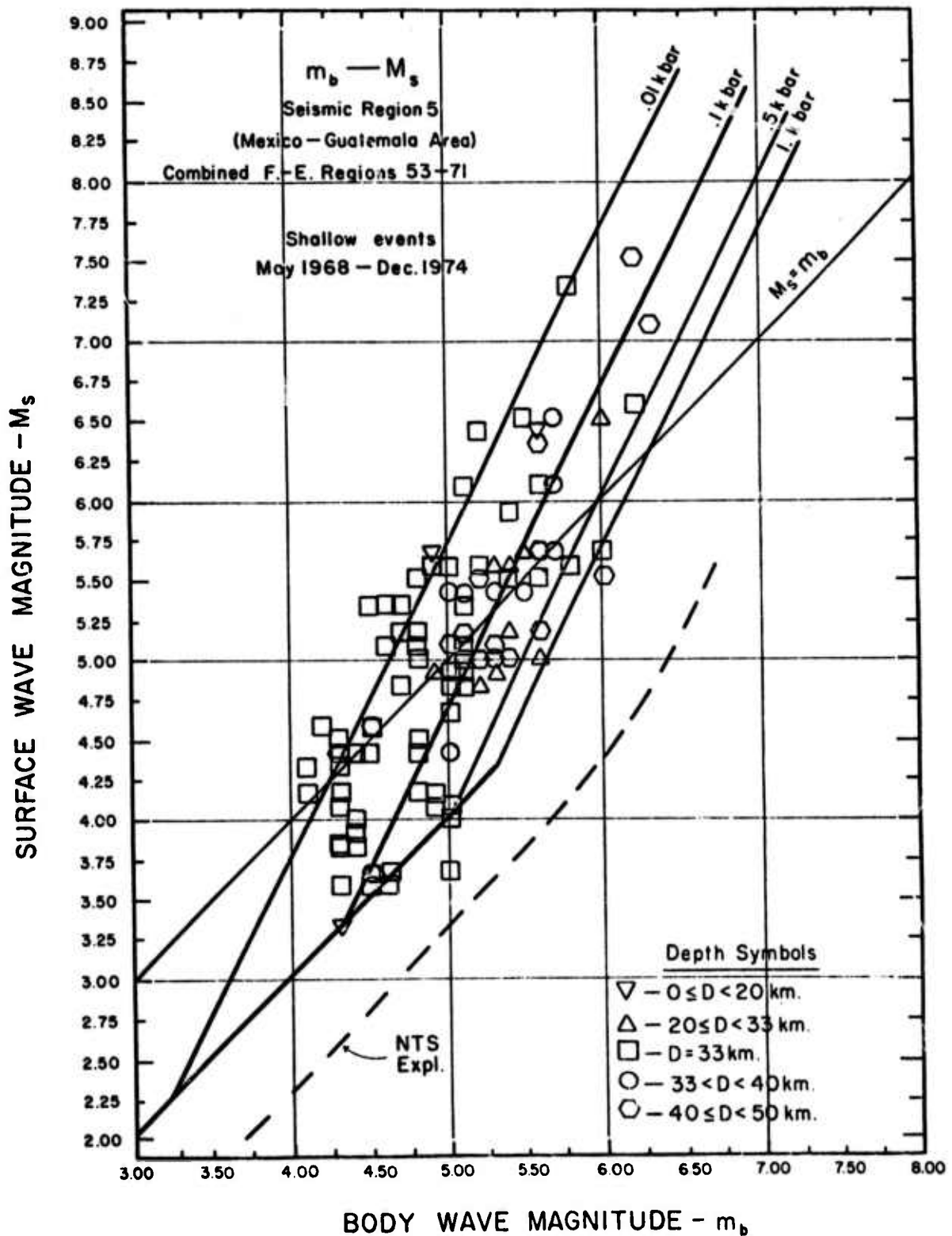


Figure 54. $m_b - M_s$ event data for Seismic Region 5, Mexico-Guatemala area.

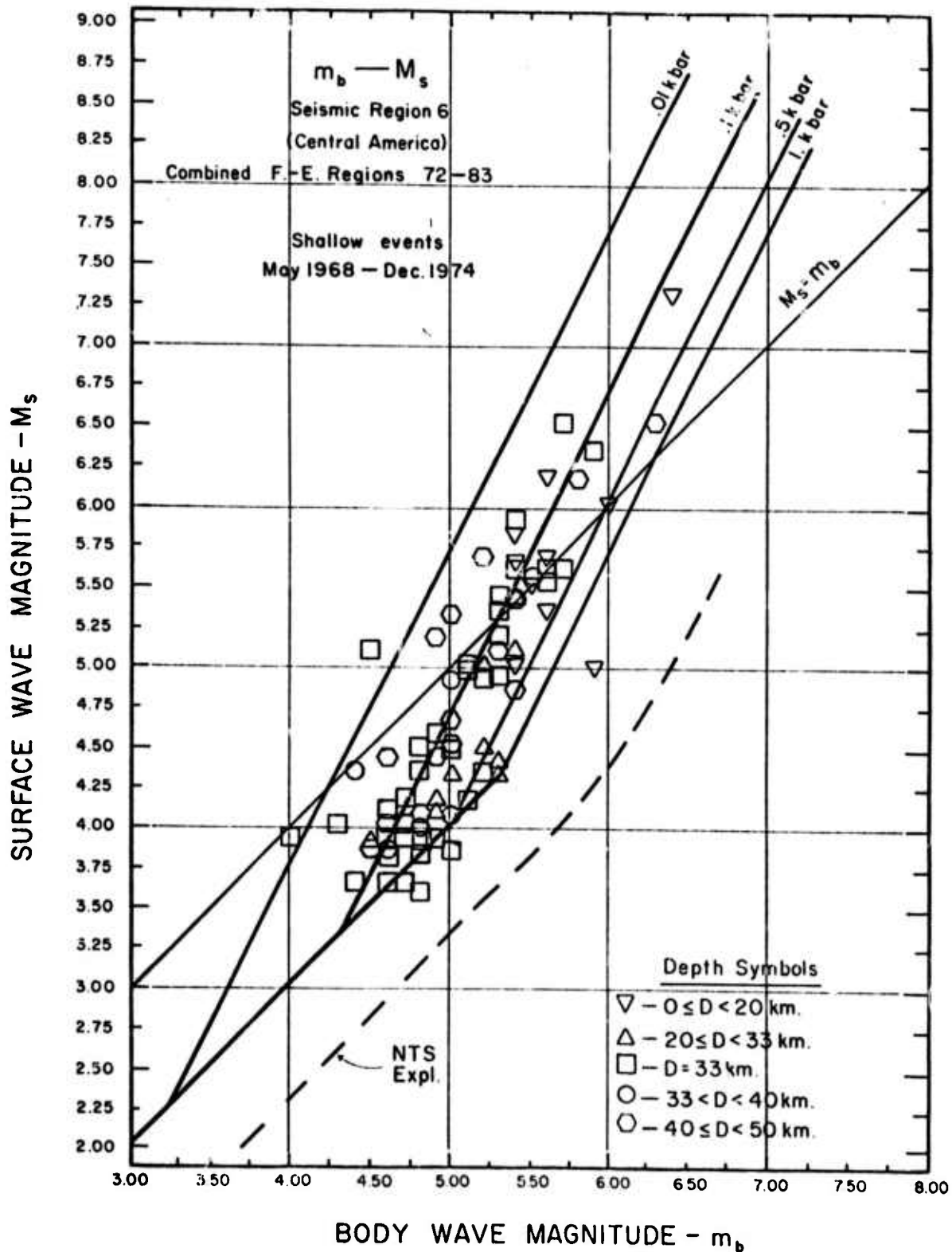


Figure 55. $m_b - M_s$ event data for Seismic Region 6, Central America.

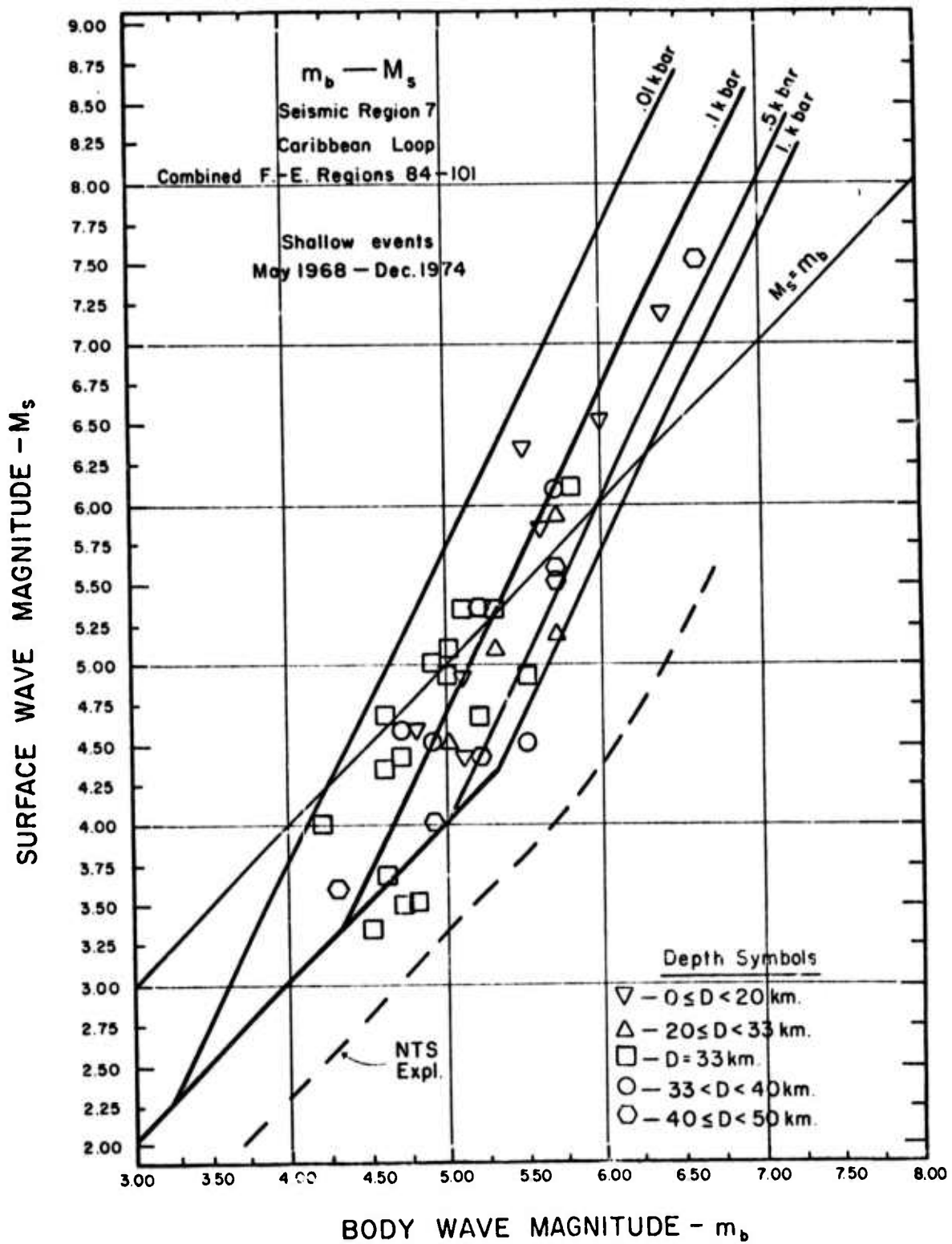


Figure 56. $m_b - M_s$ event data for Seismic Region 7, Caribbean loop.

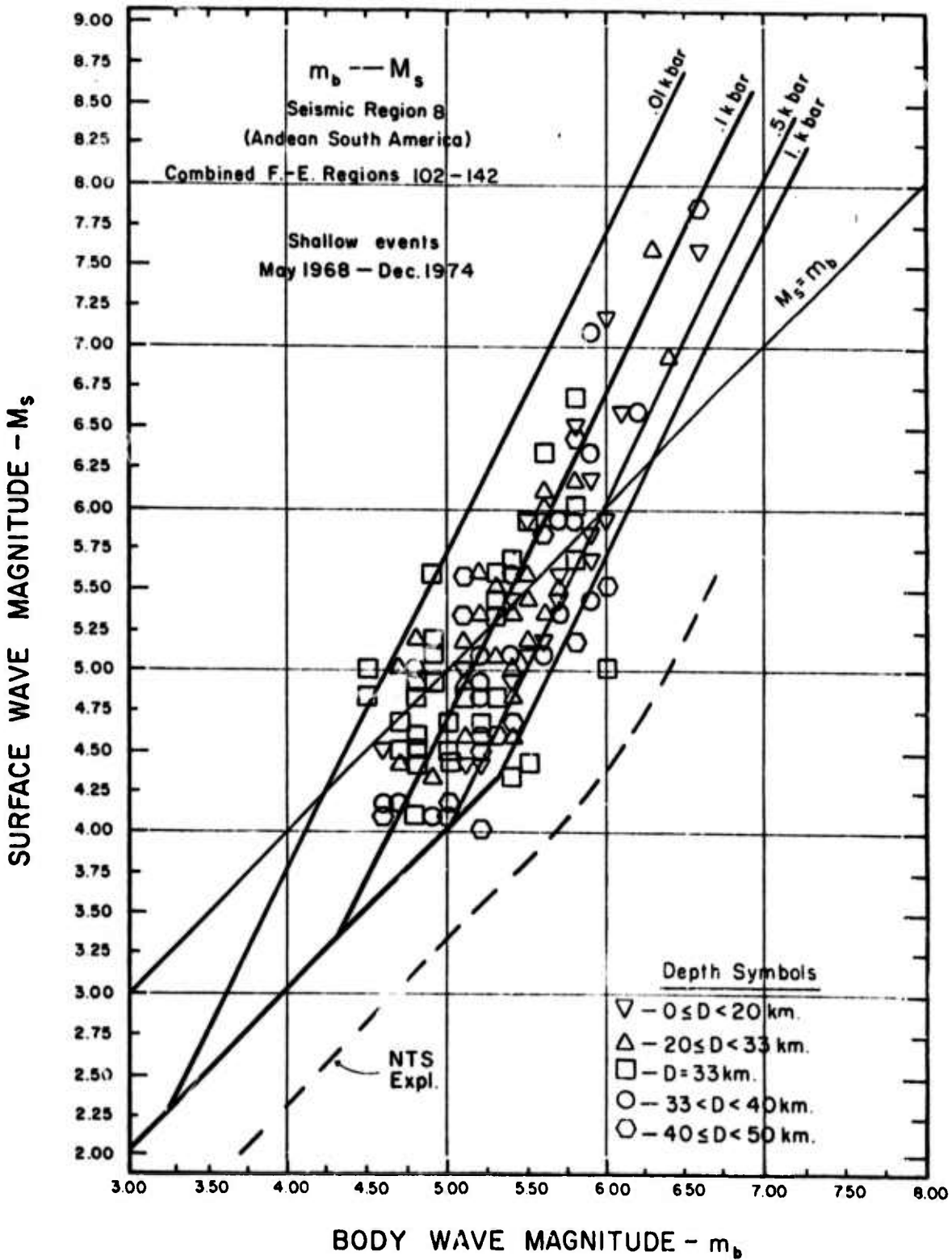


Figure 57. $m_b - M_s$ event data for Seismic Region 8, Andean South America.

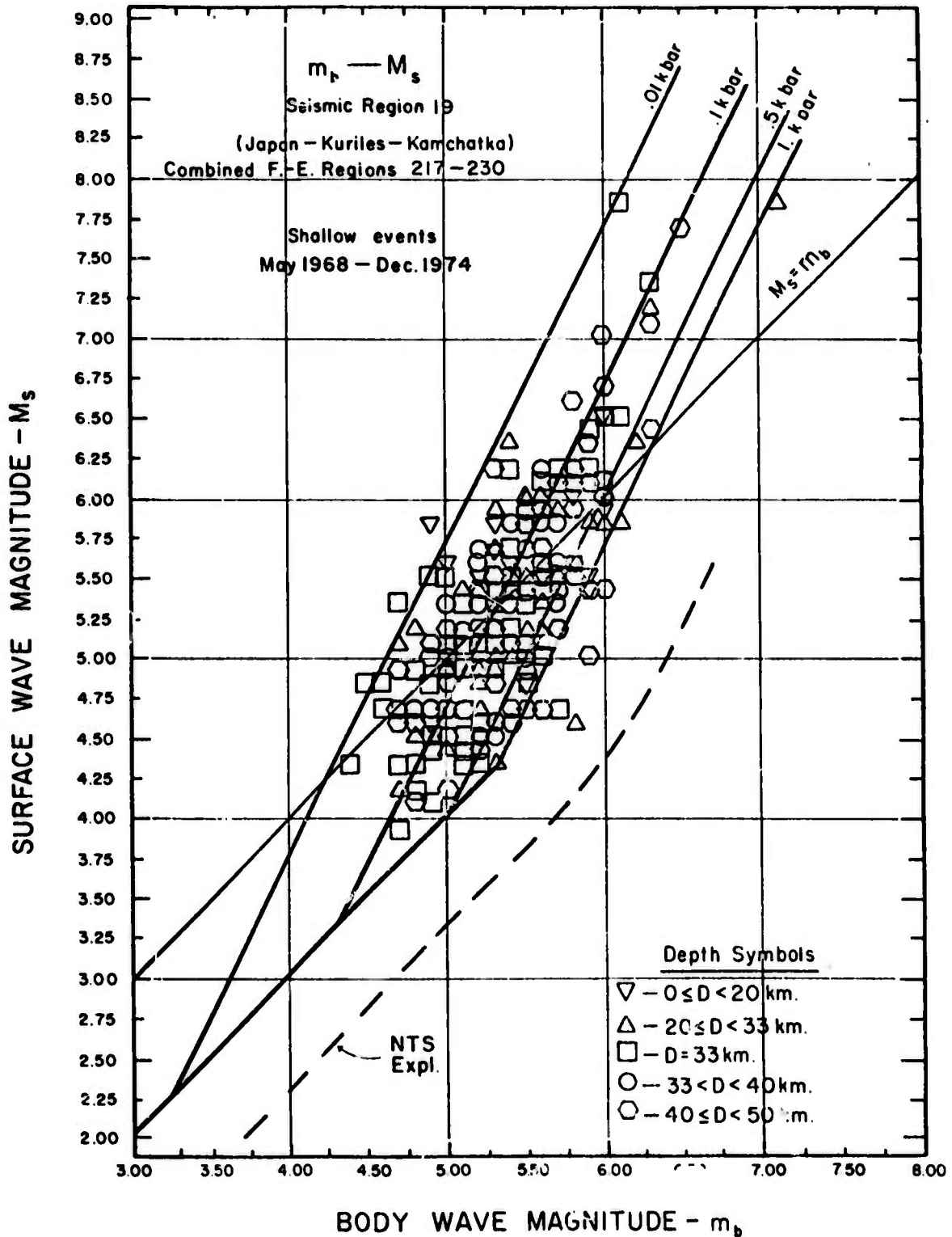


Figure 58. $m_b - M_s$ event data for Seismic Region 19, Japan-Kuriles-Kamchatka.

depths are quite uncertain, so that their M_s values could be depressed due to their being deep. One compensating factor which actually further confuses the interpretation is the fact that for small events, or for any event with small surface wave, it is commonly the airy phase, near 15 to 17 second period, that is measured rather than the 20 second Rayleigh wave amplitude. This can yield a M_s value of more than .5 greater than the M_s measured at 20 seconds. Since the theoretical curves are based on M_s at $T = 20$ sec, then the comparison to these theoretical curves is not appropriate for such events. Indeed such events would appear well above the " R_s line" when in actuality they could have $m_b - M_s$ values well below this line for the appropriately measured M_s .

The events shown here are being tabulated along with the apparent prestress/stress-drop values for each seismic reg.on. The events, in restricted depth ranges such as 0-20 km, are then plotted at their proper locations within the seismic region and contours of the stress levels defined by the events are constructed. From such a spatial projection of the apparent prestress/stress drop it is expected that a systematic pattern should emerge which is related to the structure of the region. In this manner we expect to be able to determine whether the stress levels correspond to the actual prestress or are stress drops. (e.g., If several events at essentially the same position show very different stress levels then the largest of them is probably the prestress level with the other event stress levels defining the stress drop.)

This part of the research program is obviously still in progress, but it is being developed with some considerable vigor since the interest in the results is certainly high.

V. GENERAL CONCLUSIONS AND COMMENTS ON REMAINING PROBLEMS.

Some conclusions that have been drawn that are of importance for the earthquake-explosion discrimination problem and for a general understanding of earthquake elastic wave radiation fields are:

- (i) A relaxation source theory appears to provide predictions of the radiation field from earthquakes that are in good agreement with observations, specifically m_b - M_s and other magnitude data and spectra from near field observations of earthquake radiation.
- (ii) The earthquake theory, combined with explosion source model theory, provides a coherent explanation of the m_b - M_s discriminant. It also provides a predictive basis for ascertaining when and under what circumstances this discriminant can fail. That is, it provides a basis of understanding of anomalous events.
- (iii) Theoretical predictions of spectral magnitude discriminants indicate that a short period body wave magnitude discrimination can be at least as effective as m_b - M_s discrimination and in general provides a wider separation of explosion-earthquake populations to lower magnitudes ($m_b \sim 4.0$) with few if any anomalous shallow earthquakes appearing in the explosion population. Observational tests of the theoretical predictions using roughly 200 Eurasian events have confirmed these predictions. The only earthquakes within the explosion population were some very deep earthquakes. In addition, both single and multiple explosions (the latter designed to appear as earthquakes to all other discriminants, including m_b - M_s) were identified by this discriminant as explosions. This discriminant is easily implemented in the field and as an on-line processor to detect and identify event signals.

Other spectral magnitude measurements employing surface waves were also shown to be discriminatory, but the theoretical predictions have not been observationally verified in detail.

(iv) The stress environment surrounding a failure zone and leading to failure can in many cases be highly inhomogeneous with local nonhydrostatic stress concentrations, of relatively small spatial extent, of the order of 1.0 kb. Most moderate sized earthquakes, however, appear to occur in zones with prestress at the 100 bar level, with the stress quite uniform over regions of the order of 100 km in radius.

(v) Near field spectra observations, moment measurements at widely separated frequencies and $m_b - M_s$ data for small earthquakes ($m_b \leq 5$), suggest strongly peaked far field spectra for at least some earthquakes. A conclusion to this effect is compatible with the deduced strong spatial variations in stress (indeed it would logically follow) provided that the k_s factor approximation used in the relaxation source theory is a reasonably accurate means of representing the radiation from relaxation of spatially variable prestress. A consequence of strongly peaked far field radiation is a reduction in the observed M_s value, with the event appearing explosion-like in the $m_b - M_s$ plane.

Some remaining problems are concerned with the determination of the effects of inhomogeneous prestress. In particular:

(i) By far the most important point that remains to be more fully explored and verified is the shape of the low frequency part of the far field spectrum from earthquakes. The data obtained so far suggests that many of the events had quite strongly peaked spectra. If so, this has important implications for $m_b - M_s$ discrimination, since it implies

anomalously low M_s values for these (small) events and hence possible overlap of the earthquake and explosion populations. Verification can be achieved by detailed fitting of the event seismograms, taking into full account both the source and the medium structure in a systematic way. This should be done for numerous events and in both the near and far field distance ranges, if possible.

(ii) An extension of the present relaxation source theory models to account more accurately and properly for inhomogeneous prestress will remove the uncertainty in the R_s approximation; indeed it should remove the approximation altogether. Further, a more "realistic" geometry for the failure zone would be desirable. Coupled with comparisons with complex numerical modeling of failure in a prestressed medium and current near field observations, this will provide a well verified theoretical framework for understanding failure processes and for the prediction of the radiated stress wave field from earthquakes.

ACKNOWLEDGMENTS

A significant part of this report describes results from work sponsored by ARPA under several contracts. These include, in particular, the AFCRL monitored contract F19628-74-C-0087, the USGS monitored contract 14-08-0001-12716 and the AFOSR monitored contract F44620-74-0063. The latter contract was in support of research at Systems, Science and Software with whom the author carried on cooperative, joint research on near field observations of earthquakes, among other investigations. Further, work carried on jointly by the author with Systems, Science and Software on explosions, under the DNA contract DNA 2231F and contract F44620-74-C-0063 is also included.

Finally, work under ACDA support under contract ACDA/ST-220 also contributed to some of the results described in this report.

A number of individuals contributed to various phases of the work described. These include Drs. J. B. Minster, G. A. Frazier, D. C. Harkrider, D. V. Helmberger, J. T. Cherry, T. C. Bache, J. M. Savino and P. H. Jungels. In addition, members of the ARPA/AFOSR - Near Field Program have made their data available and have provided the author with many stimulating and informative discussions.

REFERENCES

- Anderson, D. L. and C. B. Archambeau, The Anelasticity of the Earth, *J. Geophys. Res.*, 69, 2071-2084, 1964.
- Archambeau, C. B., General Theory of Elastodynamic Source Fields, *Rev. Geophys.*, 16, 241-288, 1968.
- Archambeau, C. B., The Theory of Stress Wave Radiation from Explosions in Prestressed Media, *Geophys. J. Roy. astr. Soc.*, 1974.
- Archambeau, C. B. and E. A. Flinn, Automated Analysis of Seismic Radiation for Source Characteristics, *Proc. IEEE*, 53, 1876-1884, 1965.
- Archambeau, C. B., E. A. Flinn and D. G. Lambert, Fine Structure of the Upper Mantle, *J. Geophys. Res.*, 74, 5825-5865, 1969.
- Archambeau, C. B., D. G. Harkrider and D. V. Helmberger, Studies of Multiple Seismic Events, California Institute of Technology, Final Contract Report (Draft) prepared for U. S. Arms Control and Disarmament Agency, 1974.
- Archambeau, C. B. and J. B. Minster, Elastodynamic Representation Theorems in Prestressed Elastic Media with Moving Phase Boundaries, to be submitted to *Geophys. J. Roy. astr. Soc.*, 1974.
- Archambeau, C. B. and C. Sammis, Seismic Radiation from Explosions in Prestressed Media and the Measurement of Tectonic Stress in the Earth, *Rev. Geophys.*, 8, 473-499, 1970.
- Cherry, J. T., Near Field Small Earthquake-Computer Simulation, Systems, Science and Software Report SSS-R-75-2475, 1974.
- Cherry, J. T., C. B. Archambeau, G. A. Frazier, A. J. Good, K. G. Hamilton and D. G. Harkrider, The Teleseismic Radiation Field from Explosions: Dependence of Seismic Amplitudes Upon Properties of Materials in the

- Source Region, System, Science and Software Report SSS-R-72-1193,
Contract No. DASA 01-71-C-0156, July, 1972.
- Cherry, J. T., T. C. Bache and C. B. Archambeau, A Deterministic Approach to
the Prediction of Teleseismic Ground Motion from Nuclear Explosions,
Systems, Science and Software Final Contract Report, DNA 2231F, 1974.
- Cherry, J. T., T. C. Bache, C. B. Archambeau and D. G. Harkrider, A Deterministic
Approach to the Prediction of Teleseismic Ground Motion from Nuclear
Explosions, Systems, Science and Software Report SSS-R-74-2034,
Contract No. DNA 001-73-C-0167, January, 1974.
- Cherry, J. T., T. C. Bache, J. M. Savino and C. B. Archambeau, A Deterministic
Approach to the Prediction of Teleseismic Ground Motion from Nuclear
Explosions, *Trans. Amer. Geophys. Union, EOS (Abstract)*, 56, 1148,
1975.
- Evernden, J. F., Source Models for Earthquakes and Explosions with Associated
Implications for Verification Network and Procedures, ACDA Internal
Report, 1973.
- Evernden, J. F., W. J. Best, P. N. Pomeroy, T. V. McEvelly, J. M. Savino and
L. R. Sykes, Discrimination Between Small Magnitude Earthquakes and
Explosives, *J. Geophys. Res.*, 76, 1971.
- Evernden, J. F. and J. Filson, Regional Dependence of Surface-Wave Versus Body-
Wave Magnitudes, *J. Geophys. Res.*, 76, 3303-3308, 1971.
- Futterman, W. I., Dispersive Body Waves, *J. Geophys. Res.*, 67, 5279-5291, 1962.
- Harkrider, D. G., Surface Waves in Multilayered Media. I. Rayleigh and Love
Waves from Sources in a Multilayered Half-space, *BSSA*, 54, 627-679,
1964.

- Harkrider, D. G. and C. B. Archambeau, Theoretical Rayleigh and Love Waves from an Explosion in Prestressed Source Regions, to be submitted for publication, 1975.
- Haskell, N. A., Crustal Reflection of Plane P and SV Waves, *J. Geophys. Res.*, 67, 4751-4767, 1962.
- Johnson, L. R. and T. V. McEvelly, Near Field Observations and Source Parameters of Central California Earthquakes, University of California, Dept. of Geology and Geophysics, Contract Report, Contract No. AFOSR-72-2392, 1974.
- Kelly, E. J., A Study of Two Short-Period Discriminants, Lincoln Laboratory Technical Note, ESD-TR-68-16, 56 pages, 1968.
- Kolar, O. C. and N. L. Pruvost, Earthquake Simulation by Nuclear Explosions, *Nature*, 253, 242-245, 1975.
- Lacoss, R. T., A Large Population LASA Discrimination Experiment, Lincoln Laboratory Contract Report 1969-24, 1969.
- Lambert, D. G., E. A. Flinn and C. B. Archambeau, A Comparative Study of the Elastic Wave Radiation from Earthquakes and Underground Explosions, *Geophys. J. Roy. astr. Soc.*, 29, 403-432, 1972.
- Manchee, E. B., Short Period Seismic Discrimination, *Nature*, 238, 152-153, 1972.
- Marshall, P. D., Aspects of the Spectral Differences between Earthquakes and Underground Explosions, *Geophys. J. Roy. astr. Soc.*, 20, 397-416, 1970.
- Minster, J. B., Elastodynamics of Failure in a Continuum, Thesis, California Institute of Technology, December, 1973.
- Minster, J. B. and C. B. Archambeau, Spectral and Temporal Characteristics of Seismic Wave Radiation from Tectonic Sources, to be submitted to *J. Geophys. Res.*, 1974.

- Savino, J. M. and C. B. Archambeau, Discrimination of Earthquakes from Single and Multiple Explosions Using Spectrally Defined Event Magnitudes, *Trans. Amer. Geophys. Union, EOS (Abstract)*, 56, 1148, 1974.
- Strick, E., A Predicted Pedestal Effect for Pulse Propagation in Constant Q Solids, *Geophysics*, 35, 387-403, 1970.
- Tsai, Yi-Ben, Utility of Tsai's Method for Seismic Discrimination, Texas Instruments Incorporated, Semi-Annual Technical Report No. 2, Contract No. F44620-71-C-0112 AFOSR, July, 1972.
- Wiggins, R. A. and D. V. Helmberger, Synthetic Seismogram Computation by Expansion in Generalized Rays, *Geophys. J. Roy. astr. Soc.*, 37, 73-90, 1974.